Adhesive bonding of polymer composites reinforced with carbon unidirectional non-crimp fabrics

by

Tianyi Gao

A thesis
presented to the University of Waterloo
in fulfillment of the
thesis requirement for the degree of
Master of Applied Science
in
Mechanical and Mechatronics Engineering

Waterloo, Ontario, Canada, 2022

Author's Declaration

I hereby declare that I am the sole author of this thesis. This is a true copy of the thesis, including any required final revisions, as accepted by my examiners.

I understand that my thesis may be made electronically available to the public.

Abstract

Lightweight materials have always played a significant role in product design, but global trends toward emissions reduction and resource efficiency have further increased the importance of this topic. In particular, the introduction of CO2 emissions targets and correlated penalties required by the U.S Department of Transportation is increasing the interest in lightweight materials, such as fiber reinforced polymers (FRP), which are set for significant market growth in the automotive industries.

Automotive industries would like to use FRP more broadly; however, the use is still limited because of the high manufacturing costs and long cycle times. But the recent developments in the area of manufacturing technologies are now paving the way to more widespread adoption. Newly developed manufacturing technology, such as high-pressure resin-transfer moulding (HP-RTM) can reduce the manufacturing cost and time. The technology provides a strong potential to incorporate the CFRP composite materials in high-volume production vehicles.

However, the current adoption speed in high-end products and critical load-bearing applications is still limited by the ability to join CFRP efficiently. Structural adhesive bonding represents a feasible joining method for FRPs because it entails several advantages, such as the reduction of stress concentration, and assembly cost and time.

FRP surfaces are primarily composed of a polymer matrix and can be affected by the presence of contaminants such as silicones and fluorocarbon from release compounds that represent leftovers of the fabrication process. It is important to perform a surface preparation step before bonding to remove such contamination and possibly increase the strength of adhesive joints. In the case of FRPs, the outcome of the surface preparation step strictly depends on the actual structure and composition of the composite material, especially in the near-surface region, which is the one that mostly dictates the ability of an adhesive to establish strong adhesion and a durable bond.

Concerning surface preparation and bonding of carbon fiber reinforces polymers (CFRP) manufactured using the HP-RTM technology there is still a relative paucity of contributions, especially on the existing interplay between surface modification, near-surface composite structure and the mechanics of deformation and fracture. The goal of this work was to complement the existing studies in the field and ascertain the mechanical behaviour of adhesive joints comprising composite adherents that feature a non-crimp fabric (NCF) textile whereby carbon fiber tows (or yarns) are stitched together using polyester yarns. The research work includes surface pre-treatment and characterization, mechanical testing and fractographic analysis. Surface preparation is crucial for the mechanical performance of adhesive joints. In this work, both manual sanding and UV laser irradiation (355 nm) is investigated. The morphology and topography of the target surfaces before and after surface preparation are ascertained using optical and confocal microscopy studies. Besides, the wettability is assessed using contact angle measurements. Two load cases are considered for mechanical testing of the composite joints, the Double Cantilever and the End Notch Flexure test configurations. The aim is to determine the Mode I and Mode II fracture toughness of the joints. In-situ CCD imaging during testing, post-failure visual inspection, and optical observations are combined to shed light on the mechanisms of deformation and fracture of the joints.

The obtained results highlight the peculiar interaction between surface preparation and the resulting complex surface structure of the composite. Although the treated surfaces did not show an improved wettability after sanding, the mechanism of failure of the joint was cohesive and the Mode I fracture toughness was in good agreement with that reported in previous related studies and above the values commonly reported for CFRP/epoxy joints in the existing literature. The Mode II fracture tests also displayed cohesive fracture but highlighted a mechanism of deformation whereby the ductility of the adhesive played a much more relevant role and led to the development of a fracture process zone that spanned several millimetres in length. Remarkably, the results of mechanical tests executed on adhesive joints with sanded interfaces were better than those obtained after UV-laser treatment. Although the investigation of the laser process was still preliminary and of exploratory nature, some interesting indications already emerged from this study, including the need for a fine-tuning of the processing variable that can prevent or mitigate surface degradation through photothermal ablation.

Acknowledgements

The work performed in this thesis would not be possible without the support I received from family and friends. I would like to express my special sincere gratitude to my supervisor Dr. Marco Alfano for the continuous support during my MASc studies and my life. His patience and support throughout the project not only improved my academic knowledge and skills, but also taught me complexity and importance in composite characterization and improved my writing skill. Dr. Marco Alfano also provided kindly psychological counseling during the pandemic and made me overcome the difficulties in my life.

I would like to thank the university laboratory staff: Tom Gawel, Eckhard Budziarek, Mike Bustamante, Devon Hartlen, Amir Zhumagulov, Nazmul Huda, Lukas Bauman, Nathan Nelson, Henry Ma for always being available and willing to help. I would also like to thank Dr. John Montesano for providing the composite materials employed throughout the study. Special thanks to Ramin Chitaz Dehaghani, Ningyue Mao, and Henry Ma for their help in the initial fabrication of test specimens, the UV laser treatment, and the CT X-ray analyses.

I would also like to thank the Natural Science and Engineering Research Council of Canada (NSERC) for funding my research through the grant RGPIN-2021-02446.

Finally, I want to thank my parents and my girlfriend for their continuous emotional support and unconditional encouragement over the past two years. Thanks to all my friends who helped me overcome all challenges.

To my parents Yuhong and Lirong

Table of Contents

List of Figures

List of Tables

Chapter 1: Introduction

1.1 Motivation

The increasing demand for vehicles in the world brings about the recent legislation in Canada, the US, Europe, and Asia to economize the cost of vehicle fuel consumption and reduce greenhouse gas emissions, as well as the increasing fuel efficiency of light-duty vehicles (LDVs)[1]–[4]. To improve fuel efficiency, feasible solutions can be included as improving aerodynamic efficiency, developing new efficient powertrains, and optimizing vehicle body-in-white (BIW) structures for weight reduction [5]. Reducing the vehicle weight to improve the fuel efficiency of LDVs plays a crucial role [6]. The study shows that reducing the vehicle weight by 10% can directly improve 6-8% fuel economy for a vehicle with an internal combustion engine [7]. Compared with high-strength steel and aluminum, the use of carbon fiber-reinforces polymers (CFRP) composites within LDVs structures provides higher specific strength, stiffness, and energy absorption capacity [8], [9] - see Fig. 1.1.

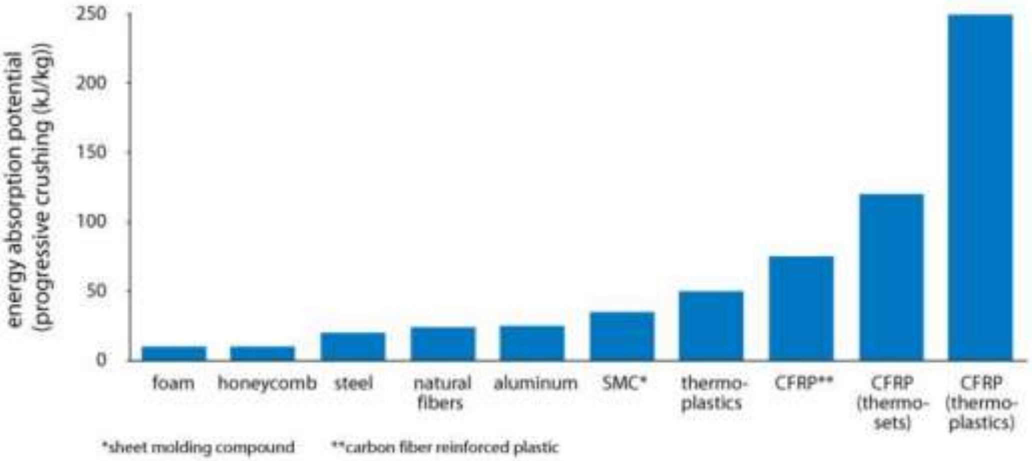

Figure 1.1: Energy absorption budget of structural automotive materials [10].

Automotive industries would like to use composites more broadly; however, the use of CFRP in BIW manufacturing is still limited because of the high manufacturing costs and long cycle times. For this reason, CFRPs are mostly used in high-performance luxury cars, such as the BMW 7 series [11], the Audi R8, [12] and Lamborgini Murciélago 670 [13]. Nevertheless, the recent developments in the area of manufacturing technologies are now paving the way to a more widespread adoption.

Newly developed manufacturing technology, such as high-pressure resin-transfer molding (HP-RTM) [14], can reduce the manufacturing cost and time thanks to the benefits of automation and fast curing resin used for the manufacturing process. A dry fabric is required to generate a preform, which is then transferred to a mold in order to start the HP-RTM process. The pressure varies from 150 bar in the mixing head to 30-120 bar in the mold. The technology provides a strong potential to incorporate the CFRP composite materials in the BIW structures of high-volume production vehicles.

Fastening methods frequently used in current CFRP composite structures are mainly riveting or bolting. However, the limitations are apparent such as the damage to load-carrying fibers by through-holes and the generation of stress concentration spots [15]. Therefore, the current adoption speed in high-end products and critical load-bearing applications is still limited by the ability to join CFRP efficiently [16]. Structural adhesive bonding represents a feasible joining method for composites. Among the various advantages brought forward by adhesives it is worth mentioning the reduction of stress concentration, and assembly cost and time. Besides adhesively bonded joints have better structural damping that can reduce the vehicle structure's noise, vibration, and harshness (NVH)[17]. For this reason, adhesive bonding has been used widely in the joining method for FRP composite materials in recent years and has good development prospects.

CFRP surfaces are primarily composed of a polymer matrix and can be affected by the presence of contaminants such as silicones and fluorocarbon from release compounds [18]–[20]. As a result, it is important to perform a surface preparation step prior to bonding to remove the contamination and possibly increase the CFRP wettability and surface energy. Typical treatments include sanding, peel-plies, corona discharge, flame, plasma, or laser treatments [21]–[27]. Sanding is the most simple method, but while removing the contaminants can also affect the carbon fibers. The use of a peel-ply is also simple, but the surface is often not suitable for adhesive bonding unless combined with another surface treatment [18]. Others surface preparation methods require very specialized equipment, such as for corona or flame treatments. These last can remove a thin surface matrix layer that usually bears the most of contamination, while being able to increase surface wettability [21]. Oxygen plasma treatment will increase carbonyl content and etch the surface, increasing surface roughness, wettability, and joint strength [22]. Other pulsed lasers such as ultraviolet [24], near-infrared [25], and infrared [26], [27] can also remove embedded contaminants through photochemical or photothermal interactions and improve the wetting and surface energy.

1.2 Objectives

Owing to the high demand for CFRPs for usage in body in white (BIW) and the interest in incorporating CFRPs into light-duty vehicles (LDVs), the goal of this thesis was to ascertain the mechanical behavior of adhesive joints comprising composite adherents manufactured with the HP-RTM technology. The composite panels features a non-crimp fabric (NCF) textile whereby carbon fiber tows (or yarns) are stitched together using polyester yarns. Besides, transversely oriented glass fibers are placed between the tows and the stitching to provide support during handling and manufacturing. The main objectives of the present work can be summarized as follows:

- Develop an effective surface preparation methodology that allows to achieve cohesive fracture of adhesive joints. Both mechanical and physical pre-treatments, i.e., manual sanding and pulsed laser irradiation, will be explored.
- Ascertain the effect of the above surface modification methods on surface morphology, and topography, and investigate the wettability and ensuing surface energy.
- Manufacture high-quality NCF-CFRP/epoxy joints and perform fracture tests in Mode I and Mode II using the Double Cantilever Beam (DCB) and the End Notch flexure (ENF), respectively.
- Assess the effect of different structural adhesive on the mechanical performances and evaluate the obtained results thorugh fractographic analyses supported by visual inspection and optical microscopy.

1.3 Thesis overview

Chapter 2 provides a summary overview of the theoretical background regarding the mechanics of composite materials and ensuing failure modes; background knwoledge about fabrication methods is briefly provided, including the HP-RTM technology. Then, joining methods suitable for composites are presented along with a litterature review that focuses on the state-of-the art methods recently developed to enhance the mechanical behavior of composite joints.

Chapter 3 provides details about the materials and the procedures used to manufacture NCF-CFRP/epoxy joints; it also includes description of the surface preparation methods and the mechanical tests employed to assess the Mode I and Mode II fracture toughness.

Chapter 4 reports a detailed description of the obtained results, while Chapter 5 includes a detailed discussion in the context of the most current works on the subject.

The thesis ends with Chapter 6, that provides the main conclusions as well as recommendations for future works.

Chapter 2: Background and literature review

This chapter provides a general overview of fiber-reinforced polymer (FRP) materials. The general characteristics of FRPs will be presented in Section 2.1. Thermoset and thermoplastics composites will be briefly discussed in Section 2.2. Manufacturing methods for thermoset based composite materials (which are the focus of the present effort) will be presented in Section 2.3. Deformation and fracture of composite materials will be the subject of Section 2.4. Then, an overview of the most common joining methods will be provided in Section 2.5, including bolts, rivets, and adhesives. Finally, the influence of surface preparation will be discussed in Section 2.6 by making reference to the most current related research works.

2.1 Overview of lightweight fiber reinforced polymer composites

In 2020, more than 276 million vehicles were on US roads, consuming approximately 54% of US transportation energy sources/fuels [28], [29]. Reducing the consumption of petroleum can make great contributions to economic and energy security as well as providing benefits to the environment. Traditional vehicles use metallic alloys for body-in-white (BIW) framing, which increases vehicles weight and fuel consumption. Therefore, the most important advantage of FRP compared to metals is the significant weight reduction while maintaining a relatively high strength. In particular, the specific modulus (ratio of material stiffness to density) of FRP between three and five times greater than that of metals [30]. In addition, the specific tensile strength (ratio of material stiffness to density) is approximately four to six times greater, and the potential for service induced corrosion is significantly reduced [30]. As a result, FRPs are increasingly being considered as very attractive candidate replacement materials in cars and trucks to increase fuel efficiency and handling [31], [32].

FRPs contain essentially two phases, i.e., high-strength fibers embedded within a binding matrix. It follows that FRPs are heterogeneous materials provided with significant fraction of interfaces separating the matrix from the reinforcement [33]. FRPs can provide a high stiffness along the fiber direction, and the matrix phase holds the fibers in place and transfers the load to the fibers through the interfaces [34]–[36]. Compared with homogenous lightweight materials, FRP materials can be tailored to achieve the desired properties for the intended application, including high inherently damage tolerance, especially in fracture performance and energy absorption [37]. However, the orientation and laminate stacking sequence of the fiber can make a large infect on the strength and stiffness of FRP. In addition, the anisotropic mechanical properties of laminated composite materials can be tailored by altering the fiber orientation and stacking sequence.

There are many ways to introduce the reinforcement fibers within the matrix and the most common way is to use woven fabrics. Woven fabrics are formed by interlacing the fiber yarns along two orthogonal directions (weft and warp directions) leading to a 2D fabric with crimped yarns [38]. The main role of the reinforcement fibers is to support the majority of the applied load. It should be noted that fibers are inherently stronger than the bulk form because of the reduced probability of defects [39].

Unidirectional non-crimp fabrics (UD-NCF) consist of layers of parallel fibers arranged in one direction, stitched with thin textured polyester yarns. Different orientations such as +45º, -45º, +30º, etc. are also possible [40]. Pillar, cord satin, and tricot stitching patterns are commonly used. The tricot stitching pattern can be found on the carbon fiber tows in a zig-zag form along the direction of the fiber direction [41] (see Fig. 2.1). Transversely oriented supporting fibers are typically placed between the tows and the stitching to provide support for handling during processing [41]. Compared with woven fabrics, UN-NCFs provide several advantages, including superior in-plane properties due to ideally non-crimped fiber tows and good drapability, improved reinforcement performance during processing and reduced manufacturing cost owing to the simplicity of the architecture [42]–[44]. Multi-directional layers of UD-NCFs can be combined together to tailor the anisotropic mechanical properties of the laminate by using a thermoset matrix. The UD-NCFs cost has a negative correlation with the increased number of filaments per tow. Some heavy-tow UD-NCFs may contain up to 50,000 filaments per tow, which have been used for automotive applications [41], [45], [42].

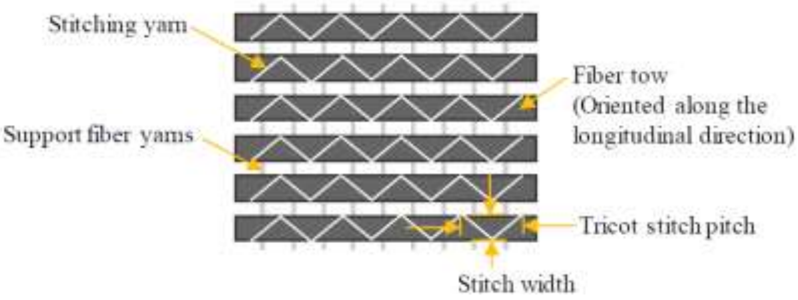

Figure 2.1: Schematic of unidirectional non-crimp fabric [41].

2.2 Thermoplastic versus thermoset polymer matrix composites

Thermoplastics are resins that are solid at room temperature but become soft when heated and eventually become fluid as a result of crystal melting or from crossing the glass transition temperature [46]. Thermoplastic polymers can be shaped through several steps, including heating and cooling. Upon heating, the materials can flow through a mold and achieve the desired shape upon cooling. Due to this special feature, thermoplastic material can be recycled and be considered an environmentally friendly material. In addition, thermoplastics can be produced through different techniques, such as extrusion or molding. Major types of thermoplastics include styrene, propylene, and ethylene, which account for 80% to 90% of the overall thermoplastic monomers produced [47].

Thermosets polymers, also called thermosetting resin or thermosetting plastic, are specific class of polymers that form well-defined, irreversible chemical networks through curing. This last can either occur due to heating or through the addition of a curing agent [48], therefore causing a crosslinking formation between its chemical components, and giving the thermoset a strong and rigid structure that can be added to other materials to increase strength. The application of thermoset polymers includes coatings and epoxy adhesives employed in construction and building industry, as well as in transportation and electrical equipment [47]. Thermoset polymers are also used widely in advanced applications, such as composite materials used in aerospace, automotive, and military industries.

The main differences between thermoset and thermoplastic are shown in Tab. 2.1 [49], [50]. Thermosets are provided with higher hardness compared to thermoplastics because of the three-dimensional network of bonds, or crosslinks, that are created during curing. Because of the ensuing strong covalent bonds between polymer chains, thermosets are more suited to high temperature applications too. The higher the crosslink density, the better the heat degradation and chemical attack resistance. Higher crosslink density also improves the mechanical strength and hardness of these materials, although this can lead to brittleness [46]. As a matter of fact, thermoset polymers are considered to be more suitable than thermoplastic polymers for FRP manufacturing because thermoplastics require a high temperature to melt and have high viscosity, which makes the manufacturing process more complex. On the contrary, thermoset polymers can cure at room temperature with lower viscosity and have a higher curing speed.

Table 2.1: The two main classes of polymers [49], [50].

Materials	Main characteristics	Examples
Thermoset	• Highly cross-linked upon curing (irreversible bonds) • Not recyclable • Cannot be reshaped. • Dimensional stable. • Cost effective	• Polyisoprene • Polyurethane • Benzoxazines • Polyester resin
Thermoplastics	• Highly recyclable • Reshaping ability. • Chemical resistance. • More expensive.	• High-density polyethylene Polyethermide • Polyphenylene oxide • Polyether ketones

2.3 Manufacturing methods of FRP

Manufacturing methods for FRPs can be classified into open mold, closed mold, and other processes. Open mold processes include wet lay-up, hand/automatic laying of prepreg, and vacuum bagging with an autoclave. Closed mold processes include resin transfer molding, resin infusion molding, wet compression molding, hot pressing prepregs and thermoforming. Other processes can include filament winding, pultrusion, and 3D printing [41].

FRP composite manufacturing processes that use liquid resin to impregnate a fabric preform stack in a closed mold are called Liquid Composite Molding (LCM) processes [51]. LCM manufacturing processes are used in aerospace and automotive industries because they can provide high quality parts with complex shapes. Common LCM processes include resin transfer molding (RTM), that is a mature manufacturing process after two decades of development [45], [52]. In a typical RTM manufacturing process, the fabric preform is placed in the cavity of a closed mold. Then, the premixed resin will be injected into the closed mold allowing wetting of the fabric layer prior to curing and hardening of the near net shape composite part (see Fig. 2.2). High pressure mixed resin replaces air under low pressure, the displaced air will escape the mold through vents to avoid dry spots and minimize void formation [53]. RTM cycle times depend on part thickness, resin type and processing temperature, and it may take from few minutes to hours [54]. The benefits of the RTM process include the ability to produce high quality geometrically complex parts with tight tolerances and high repeatability despite the long cycling time. Thus, RTM is regarded as a cost-effective process and has attracted the interest of the automotive industry [55]. Although the manufacturing process is relatively simple and the fabrication cost is acceptable, the process is still affected negatively by the high initial setup cost and the small to medium sizes of the obtainable parts [56].

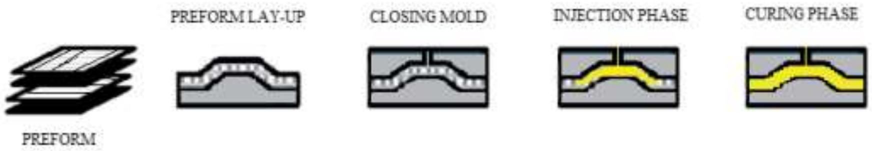

Figure 2.2: Sequence of the main steps of RTM process [57].

To solve the limitations of RTM, a new process known as high-pressure resin transfer molding (HP-RTM) was recently developed. The manufacturing steps can be seen in Fig. 2.3. Compared with the traditional RTM process, HP-RTM process employs highly reactive resin and hardener components that are rapidly mixed and injected into the closed mold at high pressure and flow rate using a costly metering unit with a mix head. The high mold cavity pressure requires a large press to maintain the tool shut and sealed in position during resin injection. This implies a pre-vacuum step for the model before the mixed resin is injected. Thanks to the automation of the manufacturing process and the use of fast curing resin and high-pressure injection, HP-RTM cycle times are reduced to minutes [58], [59]. In addition, the high injection pressure leads to improved part surface finish and higher attainable fiber volume fractions.

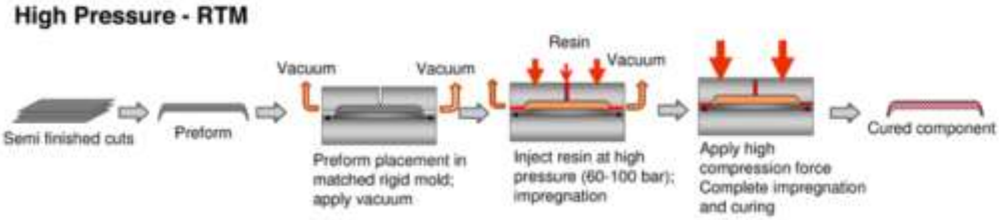

Figure 2.3: Flow diagram of the HP-RTM [60].

2.4 Deformation and fracture of composites: basic concepts

2.4.1 Mechanics of laminated composites

Continuous FRP materials are comprised of several layers stacked together and oriented along different directions to achieve the required mechanical properties that, in general, are regarded as anisotropic. A lamina (or layer) can exhibit either a linear elastic response until failure or an elastic-inelastic response prior to failure, which may vary along different material directions [61]. Since the strength of an anisotropic lamina is along the fiber direction, there will be a relationship between failure direction and applied stress relative to the direction of the fibers. The linear elastic anisotropic response of lamina is governed by three-dimensional generalized Hooke's law, as per the following set of equations represented using index notation:

$$\sigma_{ij} = C_{ijkl}\varepsilon_{kl} \qquad \text{Eq. 2.1}$$

Here, σ_{ij} represents the components of the second order Cauchy stress tensor, C_{ijkl} represents the fourth order homogenized elastic tensor components, and ε_{kl} represents components of the second order infinitesimal strain tensor, where indices $i, j, k, l = 1,2,3,4$. There are 81 components for the elastic tensor for a fully anisotropic material. The symmetry of the stress tensor can be deduced by applying the principle of equilibrium. The number of the independent constants of the elastic tensor is reduced to 21 by consideration of the symmetry of the strain tensor. For unidirectional composites, such as UD-NCF lamina, the existence of three mutually orthogonal planes of material symmetry leads to an orthotropic material response, which further reduces the independent components of the elastic tensor to 9. For a UD lamina the local material coordinate system can be defined based on the 1, 2, 3 indices, with 1 representing the fiber direction, 2 the in-plane transverse fiber direction and 3 the out-of-plane direction (Fig. 2.4).

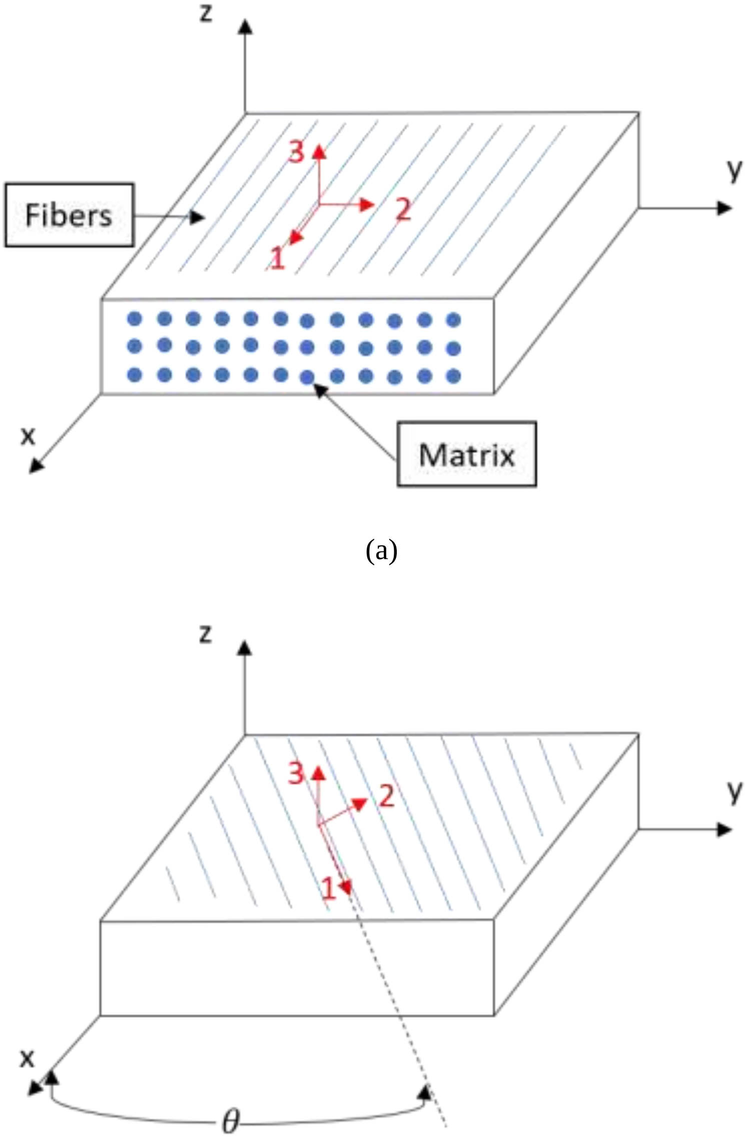

(a)

(b)

Figure 2.4: (a) Local material coordinate system for a UD composite, and (b) orientation of UD lamina with respect to the laminate coordinate system (θ is the angle between the x- and 1- axes).

Stress and strain tensors can be replaced in vector form allowing for reduced (Voigt) notation by assuming the following definitions for the indices of the stress, strain and elastic tensors: 11 = 1, 22 =

2, 33= 3, 23 = 4, 13 = 5 and 12 = 6. The stress-strain relations for a three-dimensional orthotropic lamina in reduced notation are defined as [39]:

$$\begin{bmatrix} \sigma_1 \\ \sigma_2 \\ \sigma_3 \\ \sigma_4 \\ \sigma_5 \\ \sigma_6 \end{bmatrix} = \begin{bmatrix} C_{11} & C_{12} & C_{13} & 0 & 0 & 0 \\ C_{21} & C_{22} & C_{23} & 0 & 0 & 0 \\ C_{31} & C_{32} & C_{33} & 0 & 0 & 0 \\ 0 & 0 & 0 & C_{44} & 0 & 0 \\ 0 & 0 & 0 & 0 & C_{55} & 0 \\ 0 & 0 & 0 & 0 & 0 & C_{66} \end{bmatrix} \begin{bmatrix} \varepsilon_1 \\ \varepsilon_2 \\ \varepsilon_3 \\ \varepsilon_4 \\ \varepsilon_5 \\ \varepsilon_6 \end{bmatrix} \qquad \text{Eq. 2.2}$$

$$C_{ij} = S_{ij}^{-1} \qquad \text{Eq. 2.3}$$

Where, C_{ij} represents the components of the elastic tensor, and S_{ij} is the compliance tensor components. The compliance matrix components, S_{ij}, can be written in terms of the orthotropic elastic constants as follows [36]:

$$S_{11} = \frac{1}{E_{11}}, S_{22} = \frac{1}{E_{22}}, S_{33} = \frac{1}{E_{33}} \qquad \text{Eq. 2.4}$$

$$G_{23} = \frac{1}{S_{44}}, G_{13} = \frac{1}{S_{55}}, G_{12} = \frac{1}{S_{66}} \qquad \text{Eq. 2.5}$$

$$v_{23} = -\frac{S_{23}}{S_{44}}, v_{13} = -\frac{S_{13}}{S_{11}}, v_{12} = -\frac{S_{12}}{S_{11}} \qquad \text{Eq. 2.6}$$

Here, E_i, G_{ij} and v_{ij} respectively represent the Young's moduli, shear moduli and Poisson's ratios of the effectively homogeneous lamina with respect to the local material coordinate system. It should be clarified that E_i, G_{ij} and v_{ij} are dependent on the properties of the constituent materials (i.e., the reinforcement fiber and polymer matrix) and the fiber volume fraction (V_f)

If the out-of-plan stresses approach to zero by considering the plane stress condition for the case when the laminate is thin. As a result, Eq. 2.2 is reduced from three dimensions to two dimensions:

$$\begin{bmatrix} \sigma_1 \\ \sigma_2 \\ \sigma_{12} \end{bmatrix} = \begin{bmatrix} Q_{11}\ Q_{12}\ 0 \\ Q_{21}\ Q_{22}\ 0 \\ 0\ 0\ Q_{66} \end{bmatrix} \begin{bmatrix} \varepsilon_1 \\ \varepsilon_2 \\ \gamma_{12} \end{bmatrix} \qquad \text{Eq. 2.7}$$

The reduced stiffness matrix Q and components are written in terms of the in-plane lamina elastic constants [35]:

$$Q_{ij} = \begin{bmatrix} \frac{E_1}{1 - v_{12}v_{21}} & \frac{v_{12}E_2}{1 - v_{12}v_{21}} & 0 \\ \frac{v_{12}E_2}{1 - v_{12}v_{21}} & \frac{E_2}{1 - v_{12}v_{21}} & 0 \\ 0 & 0 & G_{12} \end{bmatrix} \qquad \text{Eq. 2.8}$$

For a laminate comprised of many laminas oriented along different directions, it becomes necessary to describe the orientation of each lamina with respect to the laminate coordinate system (see x, y, z in Fig. 2.4b). The orientation of a lamina can be represented as a rotation about the z-axis by angle θ (see Fig. 2.4b). The transformation with respect to the laminate coordinate system leads to the following stress- strain relations [34]:

$$\begin{Bmatrix} \sigma_x \\ \sigma_y \\ \sigma_{xy} \end{Bmatrix} = [T_1]^{-1}[Q][T_2] \begin{Bmatrix} \varepsilon_x \\ \varepsilon_y \\ \gamma_{xy} \end{Bmatrix} = [\overline{Q}] \begin{Bmatrix} \varepsilon_x \\ \varepsilon_y \\ \gamma_{xy} \end{Bmatrix} \qquad \text{Eq. 2.9}$$

Where, $[T_1]$ is the stress transformation matrix and $[T_2]$ is the strain transformation matrix (Eq. 2.10, and 2.11), $[\overline{Q}]$ represents the lamina transformed reduced stiffness matrix, σ_x, σ_y, σ_{xy} denote the stress in the laminate coordinate system and ε_x, ε_y, γ_{xy}denote the strains in the laminate coordinate system.

$$[T_1] = \begin{bmatrix} m^2 & n^2 & 2mn \\ n^2 & m^2 & -2mn \\ -mn & mn & m^2 - n^2 \end{bmatrix} \qquad \text{Eq. 2.10}$$

$$[T_2] = \begin{bmatrix} m^2 & n^2 & mn \\ n^2 & m^2 & -mn \\ -2mn & 2mn & m^2 - n^2 \end{bmatrix} \qquad \text{Eq. 2.11}$$

In Eq. 2.10 and 2.11, m and n denote the transformation coefficients where $\mathrm{m} = \cos\theta$ and $\mathrm{n} = \sin\theta$.

The elastic response of multi-directional laminates can be defined through classical laminate theory (CLT) [34]. Where bending and stretching deformations of assumed thin plates are defined based on Kirchhoff’s plate theory. CLPT assumes that the plies are perfectly bonded and under plane stress states, plies undergo linear elastic deformation with small strains and rotations, and that there are no out-of-plane strains [36] (Fig. 2.5). Therefore, the deformation of the laminate can be reduced to a two-dimensional problem by considering the bending and stretching deformation of the laminate geometric mid-plane (Fig. 2.5).

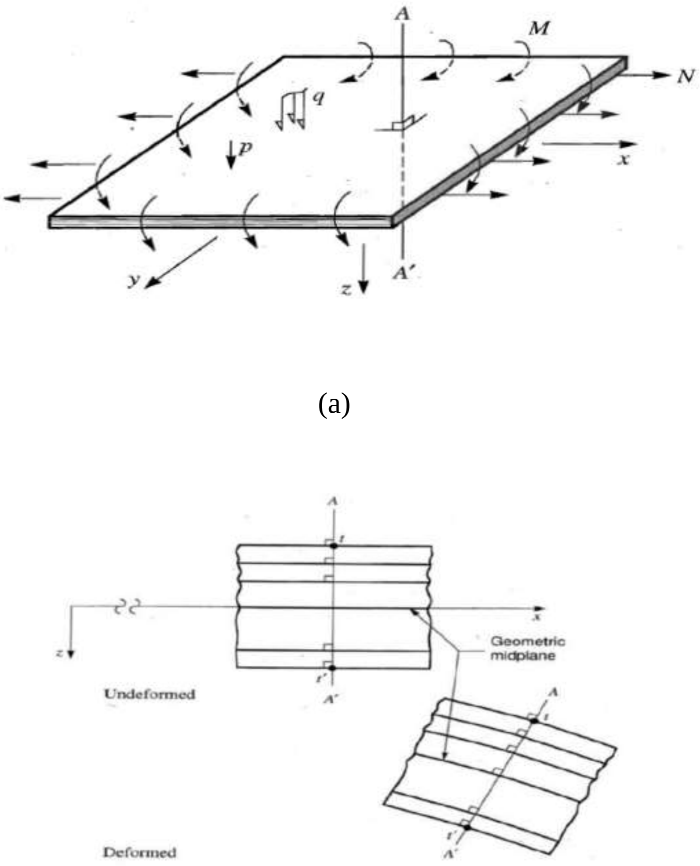

(a)

(b)

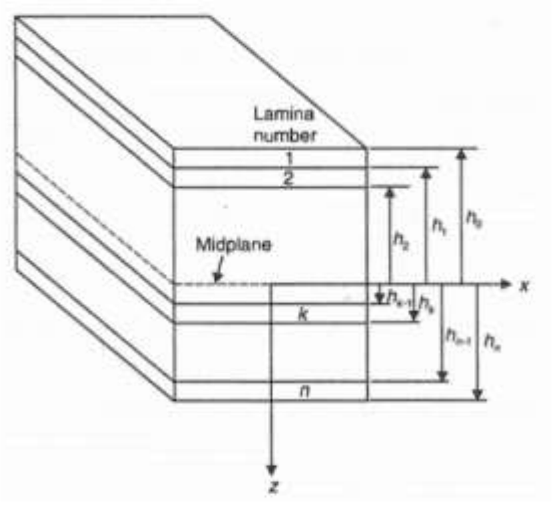

(c)

Figure 2.5: Schematic representation of a thin laminate plate: (a) external loading and resultant forces and moments, and (b) deformed and undeformed state (c) multilayered laminate geometry [36].

The strain distribution through the thickness of the laminate can be obtained from the laminate geometric mid-plane strains $\{\varepsilon^0\}$ and curvatures $\{\kappa^0\}$ and is dependent on the position z with respect to the mid-plane (Fig. 2.5c). The strain distribution in terms of the laminate coordinate system is defined per the following:

$$\begin{Bmatrix} \varepsilon_x \\ \varepsilon_y \\ \gamma_{xy} \end{Bmatrix} = \begin{Bmatrix} \varepsilon_x^0 \\ \varepsilon_y^0 \\ \gamma_{xy}^0 \end{Bmatrix} + z \begin{Bmatrix} \kappa_x^0 \\ \kappa_y^0 \\ \kappa_{xy}^0 \end{Bmatrix} \qquad \text{Eq. 2.12}$$

The stress distribution for ply k with respect to the laminate coordinate system are calculated based in the strain distribution as follows:

$$\begin{Bmatrix} \sigma_x \\ \sigma_y \\ \sigma_{xy} \end{Bmatrix}_k = \begin{bmatrix} \overline{Q_{11}} & \overline{Q_{12}} & \overline{Q_{16}} \\ \overline{Q_{22}} & \overline{Q_{22}} & \overline{Q_{26}} \\ \overline{Q_{61}} & \overline{Q_{62}} & \overline{Q_{66}} \end{bmatrix} + \begin{Bmatrix} \varepsilon_x^0 + z\kappa_x^0 \\ \varepsilon_y^0 + z\kappa_y^0 \\ \gamma_{xy}^0 + z\kappa_{xy}^0 \end{Bmatrix} \qquad \text{Eq. 2.13}$$

Where $[\overline{Q}]_k$ is the transformed reduced stiffness matrix for ply k.

The mid-plane strains and curvatures can be evaluated by considering the resultant forces {N} and moments {M} acting on the laminate (Fig. 2.5a). The laminate governing equations are defined as [35]:

$$\begin{Bmatrix} N \\ \dots \\ M \end{Bmatrix} = \begin{bmatrix} A & B \\ \dots & \dots \\ B & D \end{bmatrix} \begin{Bmatrix} \varepsilon^0 \\ \dots \\ \kappa^0 \end{Bmatrix} \qquad \text{Eq. 2.14}$$

The expanded form is shown in Eq. 2.15.

$$\begin{Bmatrix} N_x \\ N_y \\ N_{xy} \\ M_x \\ M_y \\ M_{xy} \end{Bmatrix} = \begin{bmatrix} A_{11} & A_{12} & A_{16} & B_{11} & B_{12} & B_{16} \\ A_{21} & A_{22} & A_{26} & B_{21} & B_{22} & B_{26} \\ A_{61} & A_{62} & A_{66} & B_{61} & B_{62} & B_{66} \\ B_{11} & B_{12} & B_{16} & D_{11} & D_{12} & D_{16} \\ B_{21} & B_{22} & B_{26} & D_{21} & D_{22} & D_{26} \\ B_{61} & B_{62} & B_{66} & D_{61} & D_{62} & D_{66} \end{bmatrix} \begin{Bmatrix} \varepsilon_x^0 \\ \varepsilon_y^0 \\ \gamma_{xy}^0 \\ \kappa_x^0 \\ \kappa_y^0 \\ \kappa_{xy}^0 \end{Bmatrix} \qquad \text{Eq. 2.15}$$

Where, [A], [B] and [D] are the extensional stiffness, coupling stiffness and bending stiffness matrices of the laminate, respectively. The components of the [A], [B] and [D] matrices are given by following expression [35]:

$$A_{ij} = \sum_{k=1}^{n} \left(\overline{Q_{ij}}\right)_k (z_k - z_{k-1}) \qquad \text{Eq. 2.16}$$

$$B_{ij} = \frac{1}{2} \sum_{k=1}^{n} \left(\overline{Q_{ij}}\right)_k (z_k^2 - z_{k-1}^2) \qquad \text{Eq. 2.17}$$

$$D_{ij} = \frac{1}{3} \sum_{k=1}^{n} \left(\overline{Q_{ij}}\right)_k (z_k^3 - z_{k-1}^3) \qquad \text{Eq. 2.18}$$

Where Z_k is the distance from the laminate min-plane to the bottom of ply k (See Fig. 2.5c).

The ply level stress and strain distributions can be computed along the local material directions by transforming the stresses and strains in the laminate coordinate system:

$$\begin{Bmatrix} \varepsilon_1 \\ \varepsilon_2 \\ \gamma_{12} \end{Bmatrix}_k = [T_2]_k + \begin{Bmatrix} \varepsilon_x \\ \varepsilon_y \\ \gamma_{xy} \end{Bmatrix} \qquad \text{Eq. 2.19}$$

$$\begin{Bmatrix} \sigma_1 \\ \sigma_2 \\ \sigma_{12} \end{Bmatrix}_k = [T_1]_k + \begin{Bmatrix} \sigma_x \\ \sigma_y \\ \sigma_{xy} \end{Bmatrix} \qquad \text{Eq. 2.20}$$

2.4.2 Failure modes of composites

When a UD lamina undergoes transverse compressive stress, the resulting damage is a ply crack that has an angle biased to the transverse direction (Fig. 2.6a) and is referred to as compressive matrix failure mode. This failure mode is primarily driven by shearing along the fracture plane. However, when the UD lamina exhibits transverse tensile stress, the resulting ply crack forms perpendicular to the transverse direction (Fig. 2.6b) [36]. When a UD lamina is subjected to combined in-plane shear and transverse stresses, the corresponding fracture plane orientation angle may vary.

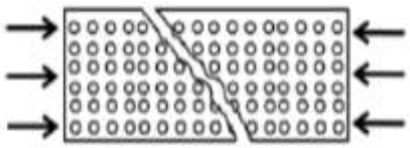

(a)

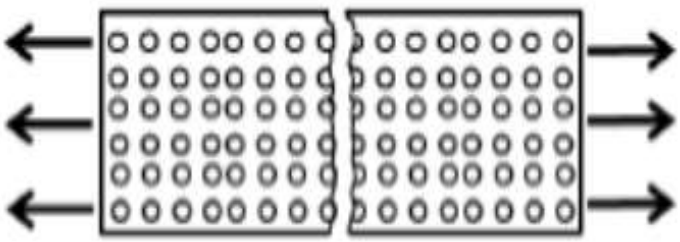

(b)

Figure 2.6: Matrix failure mode for UD lamina: (a) transverse compression and (b) transverse tension [62].

2.4.3 Failure of fiber mode

Once apply compressive stress along the UD lamina fiber direction, failure can occur as a result of in-phase fiber micro buckling caused by local matrix degradation, where a kink-band forms at an angle biased to the fiber direction (See Fig. 2.7a). The misalignment causes reduced lateral support to the fibers and the formation of kink bands at a lower stress lever [63]. Instead, the fibers fail in a brittle manner with the fracture plane perpendicular to the loading direction when the UD lamina is subjected to longitudinal tensile stress (see Fig. 2.7b).

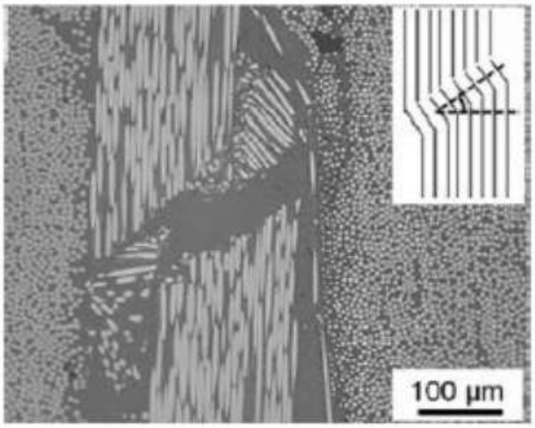

(a)

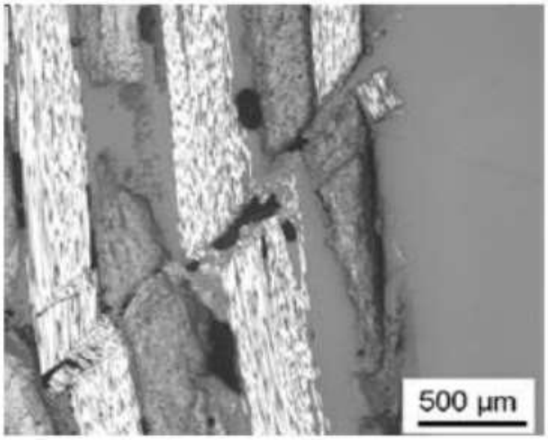

(b)

Figure 2.7: (a) Kink band formation in single UD ply of a laminate, (b) kink band and matrix crack formation in several plies of a laminate [64].

2.5 Joining of FRPs using structural adhesives

2.5.1 Available joining methods and need for adhesive bonding

Joining of composites is a challenging task because of the complex structure of composite materials [65]. Viable options include bolting, riveting and adhesive bonding. A bolted joint consists of a male threaded fastener that capture and joins other parts, secured with a matching female screw thread. Bolting can offer high strength [66] and provide a dismountable connection, however, the composite parts need to be drilled which implies damage to the reinforcing fibers and local weakening of the composite, which often require shimming. Riveted joints are permanent and can support tensile loads but also shear loads. The limitations of rivet joining are common to bolting, but also include higher manufacturing skills. Besides, a riveted joint does not make a tight or leak-proof joint unless using hot rivets or a sealant along the rivet [67]. It follows that both bolted and riveted joints introduce significant stress concentration because of the through holes needed to perform the joint. Adhesive bonding is a joining technique used in manufacture and repair of a wide range of products and is provided with significant advantages with respect to standard riveting and bolting [68]:

- ✓ good fatigue resistance;
- ✓ ability to join dissimilar materials;
- ✓ good sealing properties;

- ✓ smooth exterior appearance;
- ✓ reduced stress concentration.

These advantages are making adhesive bonding a choice that is difficult to resist in many fields and, in turn, automotive and aerospace industries would like to use adhesives more broadly; however, the presence of bondline defects generated in service or during fabrication is hampering usage of adhesives in load-bearing applications. A surface pre-treatment step is always necessary to guarantee a reliable bond and prevent the formation of bondline defects, especially with respect to environmental attack. This is very important in bonding of composites, since the mating surfaces are usually in contact with a mold and are subjected to contamination from mold release compounds thereby making the surfaces difficult to bond. As a result, for safety reasons, adhesives are mostly used in conjunction with other joining methods, such as riveting. This approach does not allow a full realization of the lightweight and cost-effective potential of this joining method. Because of the significant advantages with respect to bolting and riveting, and the increasing use of composites, in fact, joining of composites with structural adhesives is currently the subject of a worldwide research effort. The most current works related to this subject are discussed in the next section.

2.5.2 Literature review

Cleaning the mating surfaces of a joint from contaminants, increasing surface roughness, or inducing functionalizing are all tasks that can be accomplished through careful surface preparation [69]. Many surface preparation methods can be used, such as chemical treatment, peel ply, laser treatment, and abrasive sanding. The main point of the surface pre-treatment is the removal of contaminants, which are mostly represented by mold release agents applied to the tool's surface to enable demolding of cured composite, such that used in the fabrication of fiber reinforced composites using the HP-RTM. The presence of mold release agents plays a critical role because they are designed to prevent chemical bonding and, as such, they must be removed before any subsequent bonding procedure [70]. Contaminations do not only arise because of the presence of mold release compounds. In composite manufacturing, a layer of woven fabric, the so-called peel ply are often used during the fabrication of prepreg-based FRPs parts to control surface roughness and morphology (Fig. 2.8) [71].

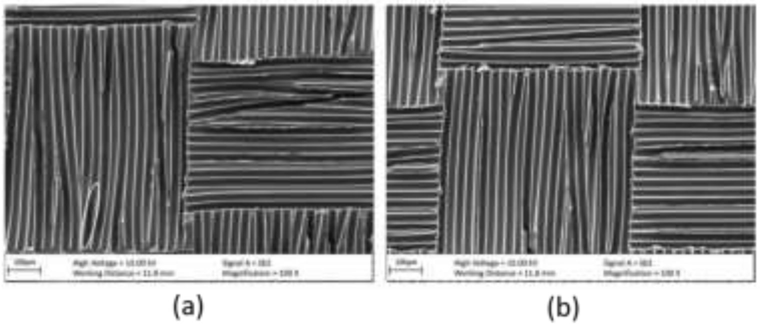

Figure 2.8: Surface morphology of a composite adherend after removal of a peel ply with (a) Hexflow RTM6 epoxy resin NCF and (b) toughened epoxy matrix NCF [71].

Peel plies are laid down on the composites and then are stripped off from the surface of the cured materials and immediately before adhesive bonding. Such process is supposed to enable the formation of a fresh matrix surface but, ironically, this is not always the case. As shown in the research by Kanerva and Saarela, the use of peel plies altered not only the roughness but, more importantly, the elemental composition of a CFRP surface [72]. Indeed, to enable removal without significant modification of the induced texture, the peel plies are often coated with Teflon or silicone. Residuals of these compounds remain on the surface of the composite and weaken the joint strength if not properly cleaned prior to bonding [73].

Among the most common surface preparation methods suitable to remove surface contamination, the following ones are recalled: mechanical abrasion (e.g., sanding, grit-blasting), chemical treatment, physical (energetic) treatments. Sandblasting, aka abrasive blasting, is the operation of forcibly propelling a stream of abrasive material against a surface under high pressure to smooth a rough surface or rough a smooth surface. The process can efficiently remove surface contamination and increase surface energy and surface roughness of FRP substrate. However, large grit size in abrasion surface treatment can not only over remove the epoxy resin on the surface, but also the fibers in the substrate. This will lead the fiber damage and decrease bond performance for FRP. Zaldivar et al. [74] performed experiments involving different blasting procedures and assessed the outcome using SEM imaging (see Fig. 2.9). The results revealed the interplay between abrasion affected zone on the FRP surface and the abrasive grit size, i.e., an increase in abrasive grit size induces larger abrasion damage zone.

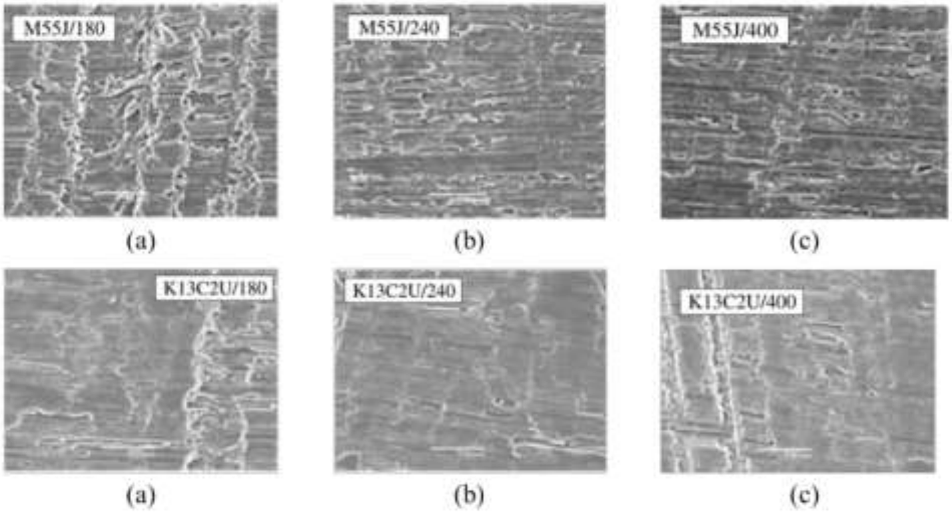

Figure 2.9: SEM images of M55J and K13C2U composite surfaces treated with sandpaper with different abrasive grit sizes including: (a) 180 grit, (b) 240 grit and (c) 400 grit adopted from [74].

Yang et al. [75] performed an investigation around the influence of sandpaper grit size on the performance of adhesively bonded CFRP joints over the range of 60-800 grit. The result demonstrated that surface abraded with 220 grit sandpaper had the best performance for their composite. Besides, abrasion along the fiber direction or perpendicular can result in the removal of the epoxy resin on the matrix at the surface and expose the fiber. However, when setting the abrasion direction was random, the surface was completely polished and loose fibers on the surface were removed, which resulted in the highest joint strength. Park et al. [76] studied the effectiveness of abrasion with sandpaper, grit blasting, and the use of a peel ply as surface treatments on the lap shear strength of CFRP secondary bonded joints. The result shows sandpaper treatment has the lowest static joint strength for SLJ because of the potentially low polar component of surface energy. However, samples with sandpaper treatment have the highest static strength retention in the cyclic fatigue testing (Fig. 2.10). The characteristic of fracture surface after the test shows the failure mode was dominated by cohesive failure during static loading.

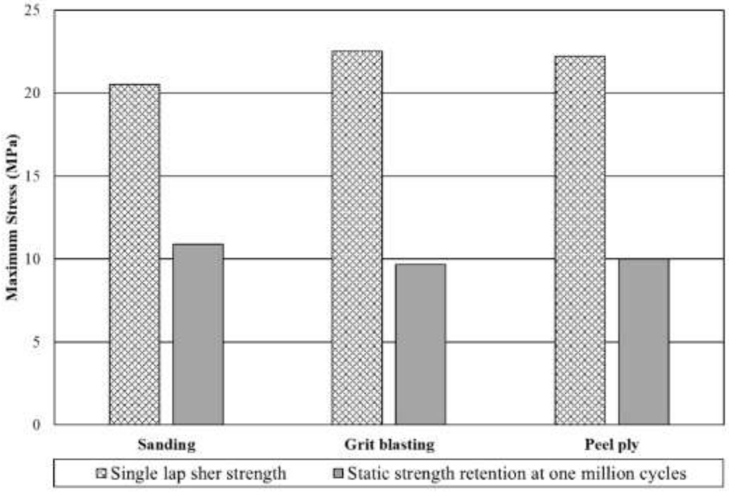

Figure 2.10: Single lap joint strength under static and fatigue loading with different surface treatments [76].

Surface cleaning using chemical products is another commonly used method to remove and clean the surface of the adherents from contaminants [77]. Effective cleaning solvents include methyl ethyl ketone, acetone, and methanol, the choice of which is based on the type of the adherents [65], [77], [78]. Chemical treatments are typically used for plastic materials to alter the physical and chemical properties of the surface [77]. The surface of an FRP composite part is generally washed with soap followed by immersion in a chemical treatment bath (e.g., acid, base, oxidizing agent, chlorinating agent, or other active chemicals [79]). The chemical agent etches the target surface leading to increased and consistent surface roughness [80]. A previous study indicated that the fracture toughness largely depends on surface preparation and it was observed that an acid etching could provide the best results (see Fig. 2.11) [81]. Besides, the authors observed that the surface morphology obtained with a chemical treatment was similar to that stemming from solvent cleaning, i.e., surface morphology does not necessarily play a relevant role for the outcome of mechanical tests.

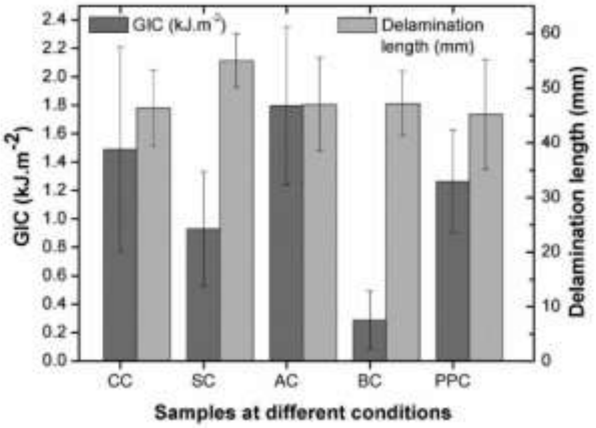

Figure 2.11: Fracture toughness and delamination length for specimens treated with different surface treatments including solvent cleaning (CC), sanding (SC), acid etching (AC), base etching (BC) and peel ply (PPC) [81].

Although a chemical treatment allows to attain good adhesion at the composite/adhesive interface, the use of chemical compounds such as acid, alkali, and oxidants, increase the manufacturing complexity since they introduce safety issues (can be harmful to operators) and requires costly disposing procedures. Moreover, a chemical treatment requires a robust understanding since prolonged interaction of the chemical solution with the composite can induce damage.

Laser surface treatment is an environmentally friendly energetic method used to prepare composite adherents. The common laser technologies used include carbon dioxide (CO_2) laser, diode-pumped solid-state (DPSS) lasers operating near the infrared wavelength spectrum, and frequency multiplied DPSS lasers with output in the ultraviolet wavelength spectrum, and excimer lasers [82]. The laser wavelength plays a significant role on the mechanism of material removal; photochemical abrasion (i.e., breaking molecular bonds by single photons) is usually enabled by UV laser radiation (<255 nm) while photothermal ablation is induced with near-infrared (n-IR) and infrared (IR) lasers. Photochemical ablation is preferred because it results in higher reactivity of the treated CFRP surface [83].

Fischer et al. indicated that laser irradiation could effectively remove contaminants from the surface without affecting the fibers. SEM imaging of treated CFRP surfaces revealed that laser intensity accurately controls the final status of the surface. At low intensity contaminants were removed and the bulk material remained unchanged (Fig. 2.12a); at higher intensity, the epoxy material was removed and the fibers were partially exposed (Fig. 2.12c).

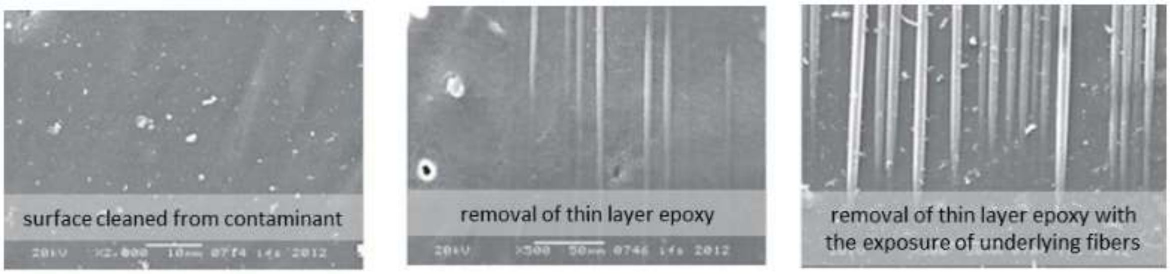

(a) (b) (c)

Figure 2.12. SEM images taken from CFRP surfaces treated with different laser intensity: (a) low (no exposed fibers), (b) increased laser intensity (fiber exposure), and (c) high laser intensity (significant fiber exposure, but no damage) [82].

Tao et al. [26] studied the effects of IR-laser irradiation on the Mode I fracture toughness of CFRP/epoxy joint. A comparison was made with peel ply and sandblasting pre-treatments. In particular, XPS analyses were carried out to track the elemental composition following the various surface preparation methods. In particular, silicon concentration (%) and total polar groups (%) as a function of surface treatment are reported in Fig. 2.13. The laser treatments could remove silicon compound and by tailoring the pulse fluence it was possible to either clean the surface (L1) without exposing carbon fibers, or completely remove the matrix (L2). In the latter case, however, the photo thermal ablation induced damage at the matrix/fiber interface. Thus, bonding directly on the exposed (loose) carbon fibers led to weak adhesion and low fracture toughness as determined in Double Cantilever Beam (DCB) tests.

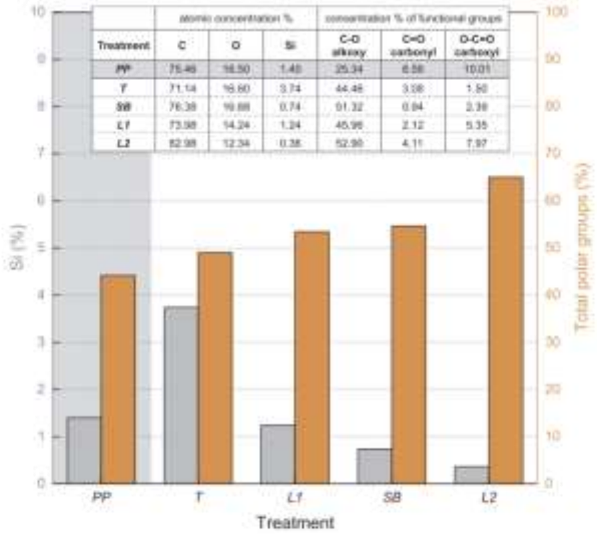

	atomic concentration %			concentration % of functional groups		
Treatment	C	O	Si	C-O alkoxy	C=O carbonyl	O-C=O carboxyl
PP	75.46	16.50	1.40	25.34	6.58	10.01
T	71.14	16.60	3.74	44.46	3.08	1.50
SB	76.38	16.88	0.74	51.32	0.94	2.38
L1	73.98	14.24	1.24	45.96	2.12	5.35
L2	82.98	12.34	0.38	52.90	4.11	7.97

Figure 2.13: Atomic concentration of elements and concentration of polar groups as obtained from XPS analyses. PP: peel-ply; T: Teflon; SB: sandblasting; L1: laser irradiation at p 1.2 J/cm^2; and L2: laser irradiation at F= 3.6 J/cm^2. [72].

The study from Sorrentino et al. [84] focused on the effectiveness of carbon dioxide laser treatment on an adhesive bonding of CFRPs. The end notched flexure (ENF) test showed an improvement in Mode II fracture toughness of up to 80% for specimens treated using the carbon dioxide laser compared to untreated specimens. The result of the fracture surfaces indicated that carbon dioxide laser treatment altered the failure mode from adhesive at the interface of adhesively bonded jointed for untreated samples to stock-break failure.

Rauh et al. employed a UV-laser treatment on CFRP adherents and manufactured single lap joints to assess the mechanical behavior. The observation of the fracture surface shows that the failure mode changed from adhesive failure to failure at the fiber-resin interface in the top surface of adherends. The joint strength of UV laser-treated SLJ specimens was 100% higher when compared to that of the mechanically abraded SLJ specimens (see Fig. 2.14) [24].

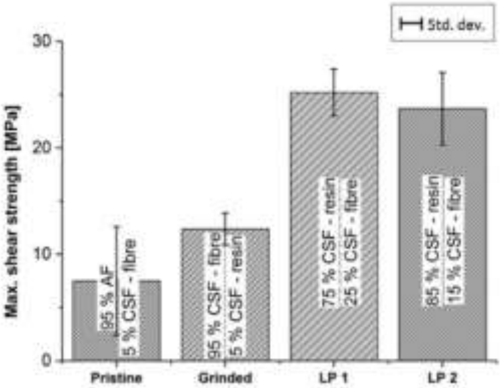

Figure 2.14: Single lap shear strengths for different surface treatments [85].

Besides classical surface preparation methods, some interesting developments are worth discussing. First, it should be recognized that improving interfacial adhesion in composite materials may not necessarily lead to a cohesive fracture. For instance, some structural epoxy have a cohesive strength that surpasses the interfacial strength of the composite joint. In such circumstances, Tao et al. [26] proposed to combine two laser processes that provide an adhesion landscape consisting of weak and strong regions parallel to the direction of crack propagation. Such patterned interface induced the formation (from the weakly bonded regions) of longitudinal adhesive ligaments, whose deformation and fracture had a leveraging effect on the fracture toughness - which was larger than the that obtained using uniform surface treatment (i.e., either L1 or L2 discussed earlier in this section). Indeed, nonlinear deformation mechanisms occurred because of ligaments bridging across the crack faces. That caused an inherently brittle interface to deform inelastically, redistributing the stresses around defects and dissipating more energy.

Chapter 3: Materials and methods

In this chapter, CFRP and adhesive materials used throughout this study, as well as the methods employed for bonding and characterization are discussed. In particular, Section 3.1 reports about the materials deployed for fabrication of adhesive joints, including composite substrates and the structural adhesives. Section 3.2 provides a detailed description concerning the surface preparation processes employed herein before bonding. Section 3.3 is focused on surface characterization including profilometry, wettability and contact angle measurement followed by determination of surface energy. Section 3.4 provides a description of the fabrication used for the Double Cantilever Beam and End Notched Flexure specimens. Besides, Section 3.5 will include the experimental procedures and data reduction schemes employed for the determination of fracture toughness. Finally, Section 3.6 reports about the methods employed for the assessment of damage mechanisms.

3.1 Materials

3.1.1 NCF-CFRP panels

The material used as substrates for the adhesive joints is a carbon fiber/epoxy composite material comprising a non-crimp fabric that was obtained through HP-RTM. The composite features a unidirectional non-crimp fabric (UN-NCF) Zoltek^{TM} PX35-UD300, which has 5 mm wide carbon fiber tows (i.e., each tow contains 50,000 PX35 carbon fibers) [41]. The carbon fiber tows (or yarns) are stitched together using polyester yarns. Transversely oriented glass fibers are also placed between the tows and the stitching to provide support during handling/manufacturing. The total density of the fabric is 333 g/m^2 with the carbon fiber tow accounting for 92.8% of the total weight.

The summary of fabric characteristics is shown in Tab. 3.1. The matrix consists of a three-part fast-cure epoxy system containing EPIKTE^{TM} Resin TRAC 06150, EPIKURE™ Curing Agent TRAC 06150, and an internal mold release agent HELOXY™ Additive TRAC 06805 (Hexion Inc.)[86], [87]. This low viscosity resin system was designed for the RTM process owing to the excellent wetting and adhesion characteristics on glass fibers, carbon fibers, or aramid fibers. Additional benefits are the low viscosity during infusion and the short curing cycle which reduces manufacturing time. Applications includes, but are not limited to, structural automotive parts such as the frame, floor panels, and bulkheads monocoque structures [88].

Flat carbon fiber/epoxy panels (900 $\times$ 550 mm^2) were fabricated using $[0]_7$ stacking sequence. The volume fraction of the consolidated panel is 53% and the average thickness was 2.27±0.03 mm [89].

Table 3.1: Zoltek^{TM} PX35-UD300 unidirectional non-crimp fabric characteristics [90].

Parameter	Value
Total fabric areal density	333 g/m2
Carbon fiber tow weight fraction	92.8%
Glass fiber yarn weight fraction	3.0%
Glass fiber yarn linear density	34 dtex
Polyester stitch weight fraction	1.8%
Polyester stitch linear density	76 dtex
Binder resin powder weight fraction	2.4%
Nominal Carbon fiber diameter	7.2 µm
Carbon fiber tow width (measured)	5 mm
Dry fabric thickness (measured)	0.49 ± 0.02 mm

The corresponding mechanical properties were determined in [61] and the results are summarized in Tab. 3.2. Notice that the longitudinal and transverse directions correspond to the directions along and transverse to the carbon fiber tows, respectively.

Table 3.2: Mechanical properties of UNC-CFRP ply with 53% fiber volume fraction[61].

E_1	Longitudinal Young’s modulus	123.4 GPa
E_2	Transverse Young’s modulus	8.4 GPa
v_{12}	Major in-plane Poisson's ratio	0.37
G_{12}	In-plane shear modulus	3.4 GPa
X_t	Longitudinal tensile strength	1765 MPa
Y_t	Transverse tensile strength	60.3 MPa
X_c	Longitudinal compressive strength	1000.7 MPa
Y_c	Transverse compressive strength	144.9 MPa
S_{12}	In-plane shear strength	42.6 MPa

3.1.2 Structural adhesives

The following structural adhesives were considered in this work, i.e., a two-part structural epoxy named Impact Resistant Structural Adhesive 07333 (3M, Canada Company) and 3M DP 190-Gray Epoxy Adhesive Translucent (3M Scoth-Weld^{TM}). The basic properties are reported in Tab. 3.3.

Table 3.3: Mechanical properties of adhesive used in the project [91], [92].

Property	**3M 07333**	**3M DP 190 Gray**
Young's modulus	2.1 GPa (ASTM D638)	N/A
Poisson's ratio	0.43	N/A
Elongation at failure	2-3% (ASTM D638)	30% (ASTM D882)
Ultimate tensile strength	35 MPa (ASTM D638)	3500 psi (ASTM D882)
Mixed viscosity [cP]	150,000 to 200,000 cPs (mixed adhesive)	75,000-150,000 cPs (base) 40,000-80,000 cPs (accelerator)

The technical data regarding the 3M 07333 adhesive were extracted from a previous study at the University of Waterloo [91] and from the manufacturer's website. The 3M 07333 is a two-part epoxy adhesive that allows for extended work time and cures rapidly with heat. The uncured adhesive has a silver color that turns to purple upon complete curing - provided proper mixing has been accomplished. The adhesive is particularly suitable for weld-bonded and rivet-bonded joints but also for repairs. Areas of application in the automotive field include the front upper and lower rail structure, and the body side structure, the rear unibody structure, the pillar and inside structure [93]. The chemical composition, including the concentration of various components is withheld as a trade secret. However, the main components are disclosed in the technical data sheet are as follows:

- Epoxy Copolymer
- Bis(3-Aminopropyl) Ether of Diethylene Glycol

- Acrylic Copolymer
- Aluminum
- Methylenedi (Cyclohexylamine)
- Synthetic Rubber
- Treated Filler
- Surface Treated Inorganic Filler
- Mineral Filler
- Tris(2,4,6-Dimethylaminomonomethyl)phenol
- m-Xylene-.alpha.alpha'.Diamine
- Polyamide Resin
- Inorganic Filler

Notice the presence of synthetic rubber that acts a toughness enhancer. The curing cycle was carried out at 80 ºC for 90 minutes following the recommendations provided by the manufacturer to reduce variability and maximum adhesive strength [93].

The main components of the 3M DP 190-Gray Epoxy are disclosed in the manufacturer data sheet as follows:

- Fatty acids, C18-unsaturated, dimers, polymers with 3,3'-oxybis(ethyleneoxy) bis (propylamine)
- Kaolin
- 3,3'- Oxybis (ethyleneoxy) bis (propylamine)
- Carbon black
- Titanium dioxide

The addition of kaolin should serve to improve mechanical properties, reduce flammability as well as improving thermal stability; besides, it has been reported to decrease the viscosity of the mixed adhesive [94]. Titanium dioxide should serve as a means to prevent brittleness induced by exposure to sunlight, while carbon black is often employed to enhance the cohesive strength of rubber-based adhesives. Curing was accomplished at room temperature (25 ºC) for 7 days.

3.2 Surface preparation methods

This work considered two surface preparation methods: a traditional light sanding treatment and a laser treatment. High-energy radiation treatments, such as pulsed laser surface preparation, is a fast and controllable technique, which can simultaneously modify surface chemistry and morphology, and is suitable for large-scale applications [26]. It was elected to perform both treatments to compare their effect on adhesion and fracture toughness of the joints.

3.2.1 Sanding

Sanding was performed using 400-grit aluminum oxide sandpaper (Norton Saint-globain), see Fig. 3.1. Two conditions were considered based on the sanding time. In the first case, the sanding process lasted 1 minute, i.e., 30 seconds clockwise and 30 seconds counterclockwise (S1). In the second condition, the treatment lasted 1 minute clockwise and 1 minute counterclockwise (S2). In addition, a degreasing step with acetone was performed before and after sanding to impart an initial cleaning of the received substrates and to remove potential debris from the sanding process afterwards. Besides, the simple degreasing step of the as received material was also used to establish a baseline surface to be used for subsequent comparisons following surface preparation.

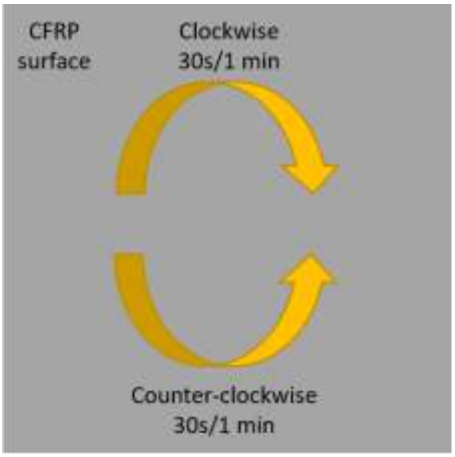

Figure 3.1: Schematic depiction of the manual sanding process.

3.2.2 Pulsed laser irradiation

Pulsed laser treatments can reduce or eliminate contamination from CFRP surfaces while keeping low the process variations [26], [27]. Currently, various choices are possible to perform laser ablation, since various laser systems operating at different wavelengths, from UV to IR, are available in the market. The interaction between the laser and the target can give rise to a variety of surface modifications, ranging from a simple surface “cleaning” with little or no modification of surface layers, to full removal of the matrix with consequent exposure of carbon fibers. The extent of surface modification depends on the wavelength of the laser source.

In this work, UV laser at 355 nm wavelength was used to perform surface preparation. The advantage of UV radiation is that it should be mostly absorbed by the epoxy matrix. As such, it does not penetrate a thicker layer of the CFRP, which may potentially damage the underlying carbon fibers (or the fiber/matrix interface). However, the energy supplied by UV laser radiation at and above 300 nm could couple with carbon fibers and lead to thermal damage [24]. The schematics shown in Fig. 3.2 illustrates some basic features of a pulsed laser source. First, notice in Fig. 3.2(a) that the laser beam is driven over the target at a given speed that is selected by the user. As shown in Fig. 3.2(b), the beam consists of regularly repeating optical pulses with repetition rate (or pulse frequency) given as:

$$f = \frac{1}{\lambda} \qquad \text{Eq. 3.1}$$

The peak power is denoted as P_{peak}, and energy supplied per single pulse as E_p. The duration of each pulse is Δt. As a result, the peak power can be related to the pulse energy and duration through the following equation:

$$P_{peak} = \frac{E_p}{\Delta t} \qquad \text{Eq. 3.2}$$

While the average power is given as:

$$P_{avg} = \frac{E_p}{\lambda}. \qquad \text{Eq. 3.3}$$

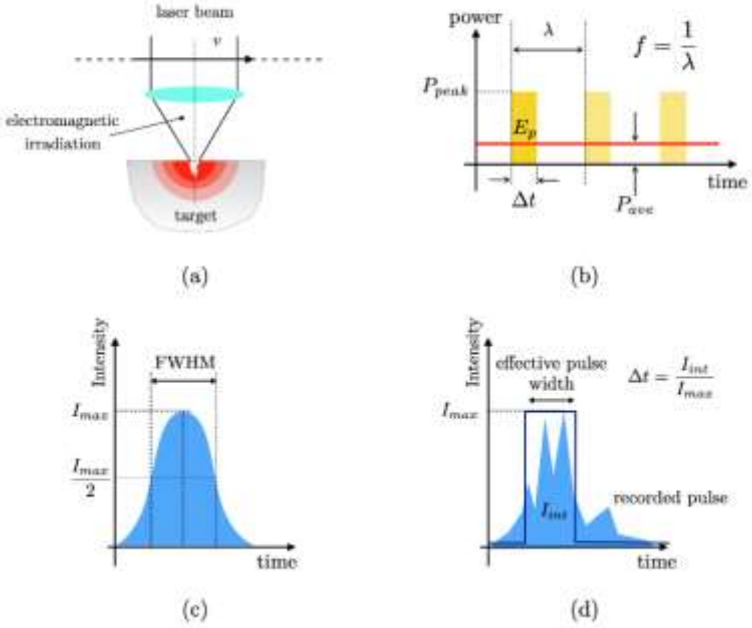

Figure 3.2: Fundamentals of pulsed laser ablation [95].

It is also important to introduce the pulse fluence, which is given as the ratio between the pulse energy and the effective focal spot area (A_s) of the laser:

$$F_p = \frac{P_{peak}\Delta t}{A_s}. \qquad \text{Eq. 3.4}$$

The intensity of the laser is given as the optical power per unit area, such that the peak intensity is given as:

$$I_p = \frac{P_{peak}}{A_s} = I_{max} \qquad \text{Eq. 3.5}$$

The pulse width is usually provided as that corresponding to full-width-half-maximum (FWHM) intensity; however, if the pulses feature non-rectangular or non-gaussian profiles, the effective pulse width is used instead. Both quantities are illustrated in Figs. 3.2(b) and (c).

UV laser irradiation was carried out using a Desktop Samurai marking system (DPSS laser Inc.) available at the Center for Advanced Materials Joining at University of Waterloo. The processing variables provided in Tab. 3.4 were set constants through the experiments.

Table 3.4: UV laser surface processing variables.

Average Power	800 mW
Laser head spot size	~10 µm
Filling spacing	0.01 mm
Laser path	Linear
Treatment times	1 time

However, the pulse frequency and scanning speed were modified as schematically shown in Fig. 3.3. In particular, the repetition rate was set equal to three distinct values, i.e., 30 kHz, 40 kHz, and 50 kHz. Likewise, the laser head moving speed was given the following values: 125 mm/s, 250 mm/s, and 500 mm/s. The corresponding pulse fluencies are also provided in the schematic below. After laser treatment, a degreasing step was carried out to remove the evaporated epoxy and contaminants.

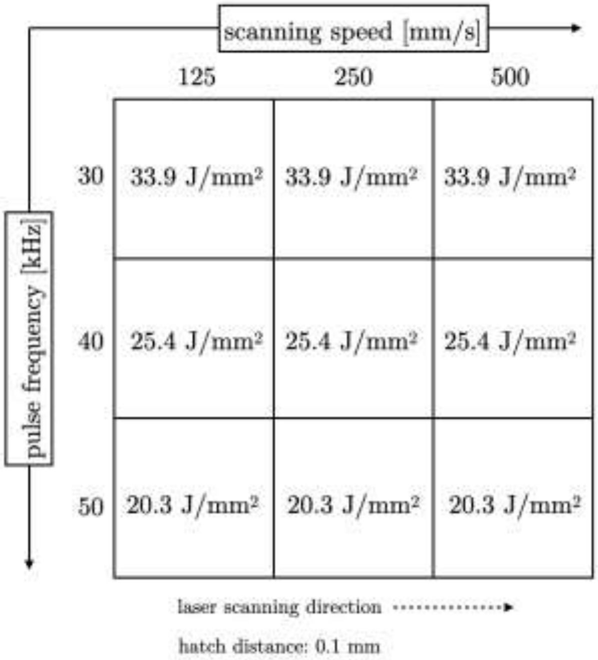

	125	250	500
30	33.9 J/mm²	33.9 J/mm²	33.9 J/mm²
40	25.4 J/mm²	25.4 J/mm²	25.4 J/mm²
50	20.3 J/mm²	20.3 J/mm²	20.3 J/mm²

Figure 3.3: Array of experimental processing condition employed to pre-treat the CFRP surface using the UV-laser.

3.3 Surface characterization

3.3.1 Profilometry

In order to investigate surface roughness of the CFRP before and after surface preparation, profilometry measurements were carried out using Laser Scanning Confocal Microscopy (KEYENCE VK-X250, Canada). The system uses a UV laser and a 16-bit photomultiplier to accurately obtain measurement data from the target surface. The system has a magnification range of 50 x to 24,000 x enabling the collection of features at nano-level. The system is depicted in Fig. 3.4 and was accessed at the MSAM Laboratory at University of Waterloo. Measurements were carried out at various location across the target surface to highlight the essential features of the CFRP surface before and after treatment.

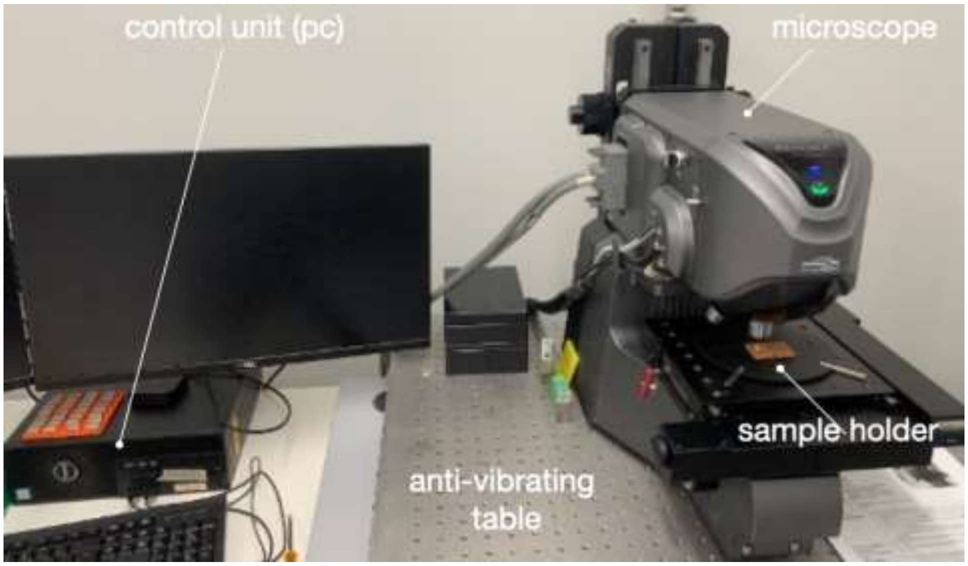

Figure 3.4: Laser Scanning Confocal Microscope available at MSAM Laboratory at University of Waterloo (E7)

3.3.2 Wettability and determination of contact angle

Wetting means the spreading of liquid on a solid surface. Wetting plays a fundamental role in many industries, as it has a role in painting, printing, and adhesive bonding, to list a few. Surface wettability is one of the key measurements that enable the analysis of the surface energy of a material, and it is determined with the aid of the contact angle (C.A.). In particular, a small liquid drop (range in the tens of microliters) is gently laid down with a calibrated syringe upon a solid, such that it flows and equilibrate with the target surface. As shown in Fig. 3.5, the equilibrium C.A. is measured as the angle where the liquid (*l*)–vapor (*v*) interface meets the solid (*s*) surface (i.e., three-phases contact point).

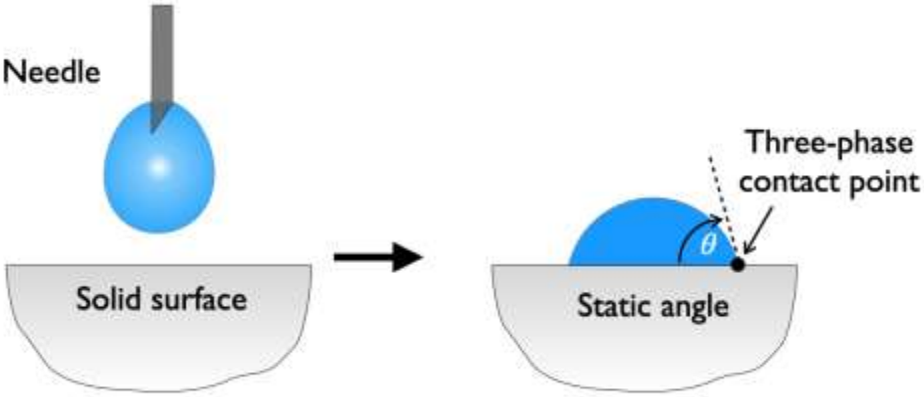

Figure 3.5: schematic representation of contact angle measurement using the sessile drop method [96].

In this work, experimental measurements were carried out using a contact angle goniometer (RAME-Hart Instrument Co. Model: 190C.A.), which is shown in Fig. 3.6. Probe liquids included deionized-water, ethylene glycol and formamide, and were dispensed using a micro-syringe. One turn of the syringe dispenses 2 μL of probe liquid. In this work, liquid drops of about 8-10 μL were chosen to ensure that the shape of the drop was not significantly affected by gravity. The actual steps followed to measure the C.A. includes:

1) Place the CFRP sample on the measurement plate.
2) Dispense a liquid drop and start the measurement using the software interface.
3) Record a snapshot of the contact angle at each 5 seconds for 90 seconds.
4) Determine the equilibrium C.A. by averaging the measurements obtained starting at 30 seconds.

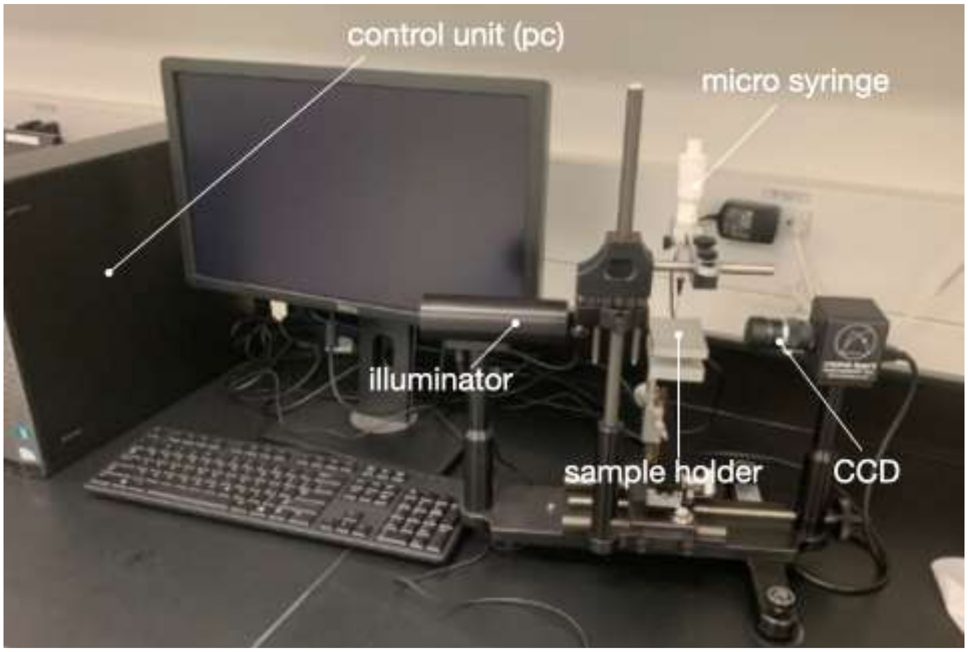

Figure 3.6: Contact angle goniometer employed in this study and available at QNC at University of Waterloo.

The C.A measurement was executed automatically using a dedicated software - see Fig. 3.7. Three reference lines were initially set before starting the test, which included right (yellow vertical line) and left reference lines (green vertical line), and the baseline (green horizontal line). The two vertical lines must be located by two sides of the syringe needle tip. The baseline was set between the liquid / solid interface. After the liquid drop falls on the CFRP surface and click the measure button, two purple lines will fit the shape of liquid droplets, and two blue tangent lines will appear to measure the instant contact angle.

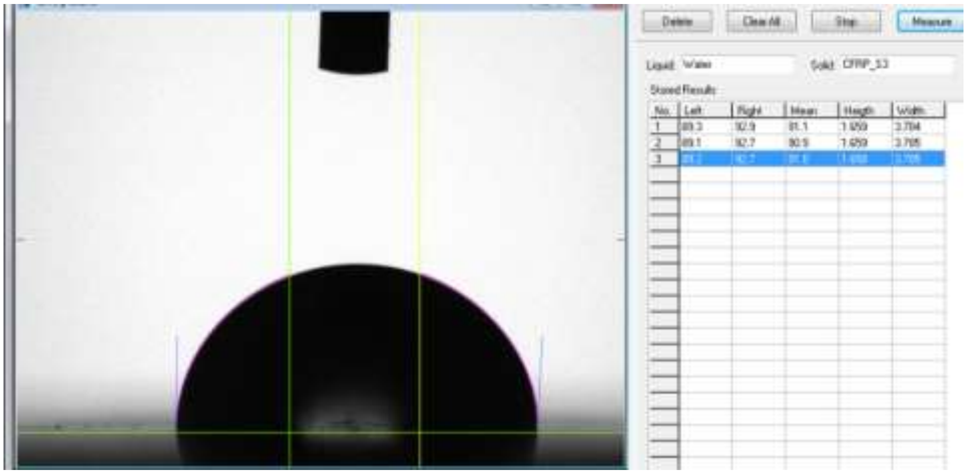

Liquid: Water
Solid: CFRP_S3

Stored Results:

No.	Left	Right	Mean	Heigth	Width
1	89.3	92.9	91.1	1.659	3.704
2	89.1	92.7	90.9	1.659	3.705
3	[illegible]	[illegible]	[illegible]	[illegible]	[illegible]

Figure 3.7: Contact angle measurement software operation demonstration.

It is noted that the final shape of the liquid drop, i.e., wettability, will depend upon the magnitude of the molecular forces established between the solid and the liquid. The most common physical forces and chemical interactions can be (*i*) electrostatic forces (Coulomb); (*ii*) van der Walls interactions (e.g., polar and dispersion forces); and (iii) chemical bonds (e.g., covalent, acceptor-donor interactions, etc.). The establishment of such interfacial forces is the reason why there is *adhesion* between materials. It follows that interfacial forces will affect the ability of a liquid to establish intermolecular contact with a solid. In the case of an adhesive, attainment of good wettability will provide, upon curing, a strong bond with the substrate. Therefore, the interface will be able to sustain sufficient stress and trigger dissipative mechanisms in the adhesive, such as inelastic deformation and crazing. Therefore, it is important to connect these interfacial forces with C.A. measurements.

It is firstly noted that surface tension is the physical property directly related to the force acting between molecules and it is given in [N/m]. The molecules in the bulk of a liquid are surrounded by like molecules and the net force acting on them is zero. However, if two immiscible molecules are separated through an interface, there will be an intermolecular force at the interface, the net force will be different than zero and a tension will exist. Surface tension and surface energy [J/m^2] are used interchangeably in the field of adhesion science and technology. Their origin is the same, as they are originated from the force mismatch occurring at the interface between alike molecules. However, their difference in physical meaning is important, since surface tension is a force that is provided with magnitude and direction (vector), while surface energy is a scalar. The contact angle of a liquid with a solid surface can be linked to surface tension through the Young equation. In reference to Fig. 3.8, from simple vector calculations, it follows:

$$\gamma_{sv} = \gamma_{sl} + \gamma_{lv}\cos(\theta) \qquad \text{Eq. 3.6}$$

where gamma is the surface tension of solid/vapor (*sv*), solid/liquid (*sl*) and liquid/vapor (*lv*) interface.

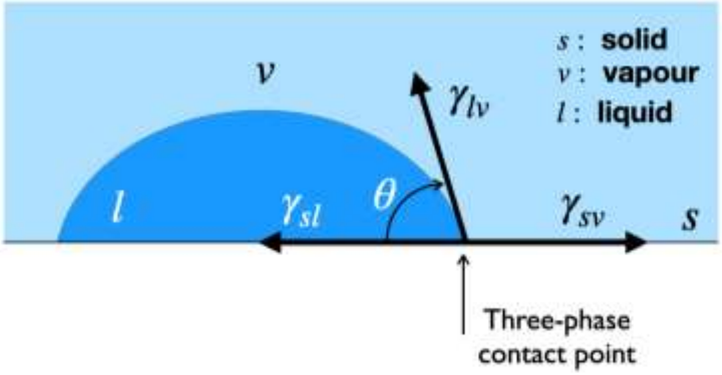

Figure 3.8: schematic representation of contact angle measurement using the sessile drop method.

The Young equation can also be obtained in a more rigorous manner from a thermodynamic point of view using an energy minimization process. Indeed, the interface is at an unstable state with higher energy and the interface area should be reduced to stabilize the high energy state. For the derivation of Young's equation, it is assumed that the surface is ideal, that is, it is smooth (rigid and flat), chemically homogeneous, the liquid does not react with the surface. Besides, gravity does not affect the shape of the drop, which is considered as a spherical cap, and there is no contact angle hysteresis.

3.3.3 Determination of surface energy

Considerations regarding surface energetics are of fundamental importance to understand adhesion, as surface energies are associated with the formation of an adhesive bond. Likewise, surface energies are also associated to fracture of an adhesive bond, since fracture requires the generation of new surfaces. The work of adhesion is defined as the reversible thermodynamic work required to separate the interface from the equilibrium state of two phases to a separation distance of infinity:

$$W_a = \gamma_{sv} + \gamma_{lv} - \gamma_{sl} \qquad \text{Eq. 3.7}$$

While the work of cohesion is given as:

$$W_a = 2 * \gamma_s \qquad \text{Eq. 3.8}$$

However, practical adhesion (G) includes a surface energy term ($G_0 = W_a$ or W_c), depending on whether the interfacial or cohesive fracture is achieved), plus a contribution (β) stemming from energy absorbing processes associated to fracture, such as plasticity:

$$G = G_0 + \beta \qquad \text{Eq. 3.9}$$

It is emphasized that fracture in adhesive bonds involves $\beta \gg G_0$. In order to use the above equations, the surface energies need to be determined. This is not a simple task for solid materials. A popular method used in the adhesion field is the Owens-Wendt method. The O-W method was employed herein to determine surface free energy of the CFRP [97]. The basic assumption is that the surface energy can be divided into dispersive (d) and polar (p) components, such that:

$$\gamma_{sv} = \gamma_{sv}^{p} + \gamma_{sv}^{d} \qquad \text{Eq. 3.10}$$

The closer the ratio between dispersive and polar components, the more interactions are possible at an interface. In second place, it is assumed that the Berthelot's combining rule for the work of adhesion applies:

$$W_{sl} = \sqrt{W_l^d W_s^d} + \sqrt{W_l^p W_s^p} \qquad \text{Eq. 3.11}$$

For previous equations, it follows:

$$W_l = 2 * \gamma_{lv} = 2 * (W_l^d + W_l^p) \qquad \text{Eq. 3.12}$$

$$W_s = 2 * \gamma_{sv} = 2 * (W_s^d + W_s^p) \qquad \text{Eq. 3.13}$$

Therefore:

$$W_{sl} = \gamma_{sv} + \gamma_{lv} - \gamma_{sl} = \gamma_{lv}(1 + cos\theta) \qquad \text{Eq. 3.14}$$

Combining the above equations, one obtains:

$$\gamma_{lv}(1+cos\theta)=\sqrt{2\gamma_{lv}^{d}*2\gamma_{sv}^{d}}+\sqrt{2\gamma_{lv}^{p}*2\gamma_{sv}^{p}} \qquad \text{Eq. 3.15}$$

And dividing by $\sqrt{\gamma_{lv}^{d}}$ both sides, the thermodynamic equilibrium equation of a solid-liquid-vapor system (s-l-v) is obtained:

$$\frac{\gamma_{lv}(cos\theta+1)}{2\sqrt{\gamma_{lv}^{d}}}=\sqrt{\gamma_{sv}^{p}}\frac{\sqrt{\gamma_{lv}^{p}}}{\sqrt{\gamma_{lv}^{d}}}+\sqrt{\gamma_{sv}^{d}} \qquad \text{Eq. 3.16}$$

Where θ is the contact angle; γ_{lv}^{p} and γ_{lv}^{d} are the corresponding polar and dispersive components of the probe liquids and are reported in Tab. 3.5. γ_{sv}^{p} and γ_{sv}^{d} are the polar and dispersive components of solid surface energy. The previous Eq. 16 can be recast in the following form:

$$y=kx+b \qquad \text{Eq. 3.17}$$

Where,

$$x=\frac{\sqrt{\gamma_{lv}^{p}}}{\sqrt{\gamma_{lv}^{d}}} \qquad \text{Eq. 3.18}$$

$$y=\frac{\gamma_{lv}(cos\theta+1)}{2\sqrt{\gamma_{lv}^{d}}} \qquad \text{Eq. 3.19}$$

$$k=\sqrt{\gamma_{sv}^{p}} \qquad \text{Eq. 3.20}$$

$$b=\sqrt{\gamma_{sv}^{d}} \qquad \text{Eq. 3.21}$$

It follows that the slope and the intercept of y, i.e., $\sqrt{\gamma_{sv}^{p}}$ and $\sqrt{\gamma_{sv}^{d}}$, will prove the polar and dispersive components of surface energy.

Table 3.5: Dispersive polar and total surface free energy of the probe liquids employed for contact angle measurement.

	Dispersive energy (mJ/m^2)	Polar energy (mJ/m^2)	Total energy (mJ/m^2)
DI-Water	22	50.2	72.2
Ethylene glycol	30.9	16.8	47.7
Formamide	39	19	58

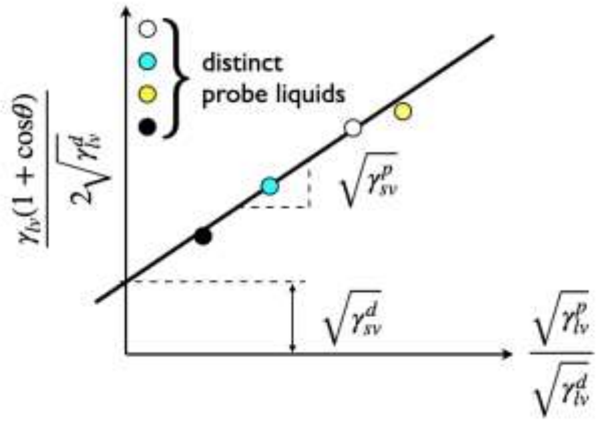

Figure 3.9: Schematic Owens–Wendt plot for determining the surface free energy [98].

3.4 Joint fabrication

Double Cantilever Beam (DCB) and End-Notched Flexure (ENF) tests were carried out in this work. To obtain the samples, composite plates were cut by an abrasive water jet cutter. The plates were cut to form CFRP substrates with dimensions 140x25.4x2.3 mm^3. After cutting, the substrates were subjected to surface preparation, either sanding or UV-laser ablation, as discussed earlier. It is noted that the target area of the UV laser was 25.5×50 mm^2 because of restrictions in the working area of the laser platform, therefore the process was completed in three steps accomplished by moving the sample. The joints were manufactured individually in a mold and bonded using the epoxy adhesives previously described. The bondline thickness was set to 0.25 mm by using shims. Each sample had two shims, the longer one located in the starter-crack region and the shorter one at the very end of the test sample. In Fig. 3.10, the pink parts are nylon shim; the yellow part is adhesive; the gray parts are CFRP adherends.

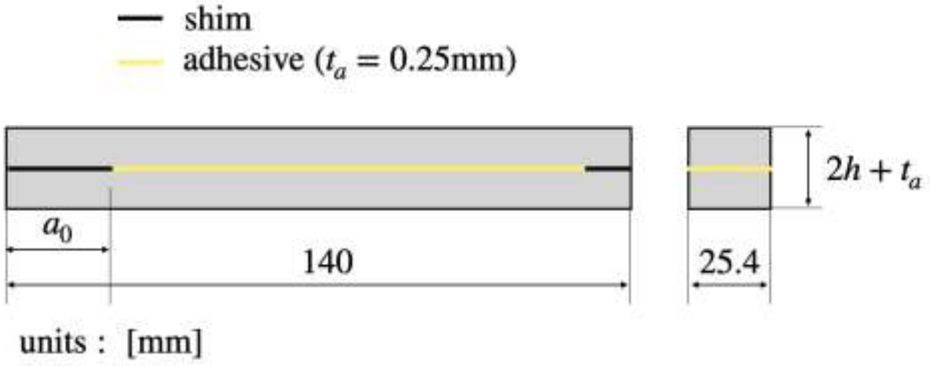

Figure 3.10: Schematic of fabricated CFRP samples.

The CFRP bottom substrates were placed on the baseplate of the mold (Figure 3.11), that ensured alignment during curing. Two heavy plates (B, C in Figure 3.11) were placed on top of the CFRP test samples. Subsequently, the bottom and top plates were secured using screws to aid squeezing the excess adhesive, and to ensure a constant bond-line thickness. Curing was accomplished by placing the mold within an oven pre-heated at 80°C and kept at that temperature for 90 minutes. After that, the oven was turned off, and the samples were left for further 30 minutes in the oven to facilitate cooling and minimize the occurrence of residual stresses. After that, the CFRP adhesive joints were removed from the mold, and the extra adhesive squeezed on the side surfaces was removed to facilitate imaging during testing. It is highlighted that the fabrication process was similar for both adhesives, except for curing. Indeed, the DP 190 adhesive was cured at room temperature (25 °C) for 7 days, as suggested by the manufacturer. After that, the joints were further cured at 71 °C for 4 hours. The specimens were kept in the mold at room temperature for at least 30 minutes to ensure slow cooling. After removing the extra adhesive on the side of specimens, a white paint was used to cover the side surfaces and a black marker was used to draw vertical lines useful to track crack position.

For the DCB specimens, loading blocks were bonded on the CFRP surface to couple them with the testing machine (See Fig. 3.12). Bonding of loading blocks was accomplished using a fast curing adhesive (LOCTITE 480 PRISM).

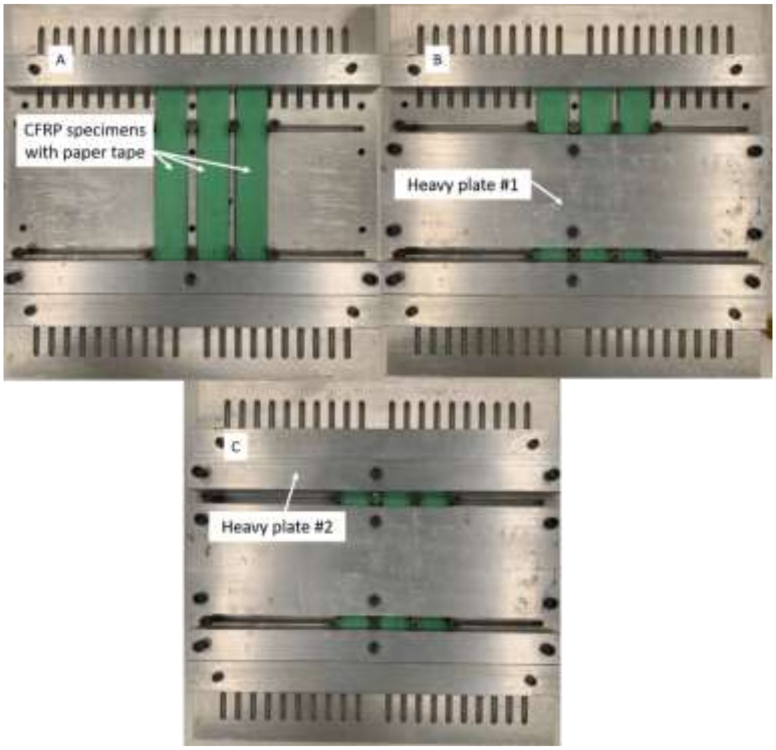

Figure 3.11: CFRP bonding steps with fixing mold without top plates (A), fixing plate on CFRP samples (B), and (C) fully fixed CFRP specimens.

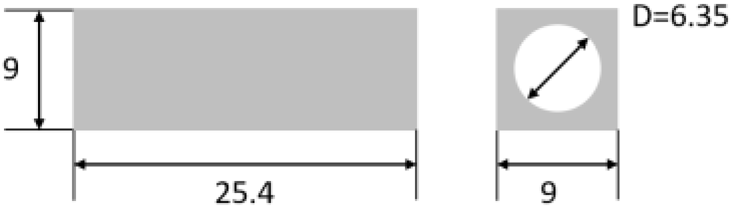

Figure 3.12: Schematic of a loading block applied on DCB specimens.

3.5 Determination of fracture toughness

3.5.1 Fundamentals of fracture mechanics

Basic concepts of fracture mechanics, including strain energy release rate (G), and the critical fracture toughness (G_c), are summarized below. If an elastic body is subjected to external loading and there is no cracking, the external work will be converted to strain energy as:

$$Fdu - dU = 0 \tag{Eq. 3.22}$$

Where, Fdu is external work and dU is the strain energy. However, once the crack grows, part of the energy will be used to create new fracture surfaces as:

$$Fdu - dU - B\mathit{\Gamma}_c da = 0 \tag{Eq. 3.23}$$

Where, $\mathit{\Gamma}_c$ is fracture toughness (energy per unit area). Notice that the above balance equation assumes that dynamic effects are negligible.

Irwin (1956) provided an approach to solve the energy release rate by re-arranging the previous equation as follows:

$$\frac{Fdu}{Bda} - \frac{dU}{Bda} = \mathit{\Gamma}_c \tag{Eq. 3.24}$$

$$\frac{1}{B}(W - U)\frac{d}{da} = \mathit{\Gamma}_c \tag{Eq. 3.25}$$

$$-\frac{1}{B}\frac{d\mathit{\Pi}}{da} = G \tag{Eq. 3.26}$$

Critical condition for fracture occurs when:

$$G = \mathit{\Gamma}_c \tag{Eq. 3.27}$$

So, fracture occurs when:

$$G \geq \mathit{\Gamma}_c \tag{Eq. 3.28}$$

while there is not crack growth if:

$$G < \Gamma_c \qquad \text{Eq. 3.29}$$

The driving force for crack growth is the energy release rate and depends on the geometry of the body, magnitude of the external and internal loading, and loading configuration. The fracture toughness depends on the morphology and chemistry of the interface, mechanical properties of the materials (or the interface), and mode of loading (opening, shear or mixed mode).

There are three types of mode of loading of a crack (see Figure 3.13). When a crack advances in a mechanical component, the stiffness decreases; strain energy changes (increase or decrease); the points of the components at which external load is applied may change; work is done on the components by the applied loading if the points move; energy is being consumed to create two mew surfaces.

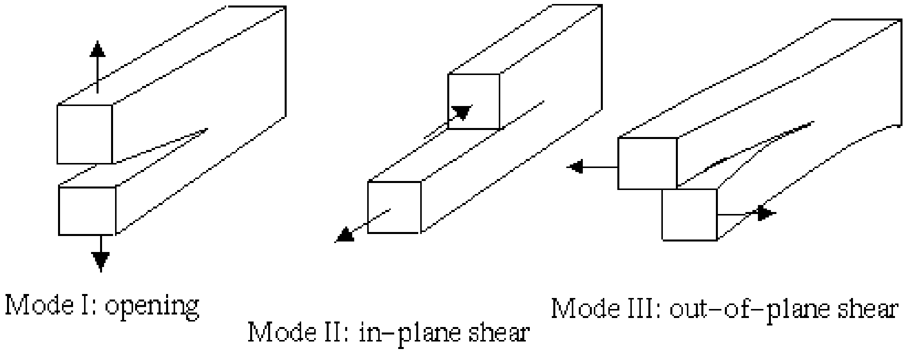

Figure 3.13: Three different types of fracture modes [99].

When crack grow under constant load (see Fig. 3.14),

5.5

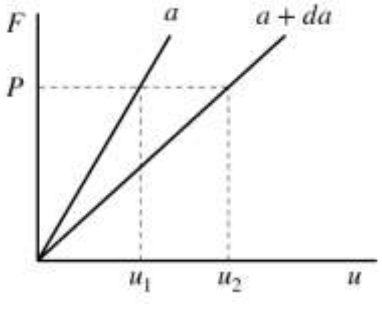

Figure 3.14: F-u chart when loading is constant.

$$dU = \frac{P(u_2 - u_1)}{2} = \frac{Pdu}{2} \qquad \text{Eq. 3.30}$$

$$dW = Pdu \qquad \text{Eq. 3.31}$$

$$d\Pi = dU - dW = -\frac{Pdu}{2} = -dU \qquad \text{Eq. 3.32}$$

When crack grow under constant displacement (se Figure 3.15):

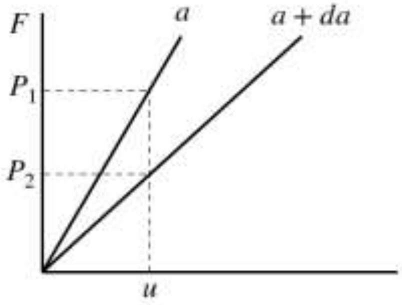

Figure 3.15: F-u chart when displacement is constant

$$dU = \frac{(P_1 - P_2)u}{2} = \frac{dPu}{2} \qquad \text{Eq. 3.33}$$

$$dW = 0 \qquad \text{Eq. 3.34}$$

$$d\Pi = dU \qquad \text{Eq. 3.35}$$

Based on Eq. 3.26,

$$G = -\frac{1}{B}\frac{d\Pi}{da} = \frac{1}{B}(\frac{dU}{da})_P \qquad \text{Eq. 3.36}$$

$$G = -\frac{1}{B}\frac{d\Pi}{da} = -\frac{1}{B}(\frac{dU}{da})_u \qquad \text{Eq. 3.37}$$

To determine G at constant load:

$$d\Pi = dU - dW = -\frac{Pdu}{2} = -dU \qquad \text{Eq. 3.38}$$

$$G = -\frac{1}{B}\frac{d\Pi}{da} = \frac{1}{B}(\frac{dU}{da})_P = \frac{1}{B}\left(\frac{Pdu}{2da}\right) = \frac{P}{2B}(\frac{du}{da}) \qquad \text{Eq. 3.39}$$

$$u = CP \qquad \text{Eq. 3.40}$$

$$G = \frac{P}{2B}(\frac{dCP}{da}) \qquad \text{Eq. 3.41}$$

As a result:

$$G = \frac{P^2}{2B}(\frac{dC}{da}) \qquad \text{Eq. 3.42}$$

To determine G at constant displacement:

$$G = -\frac{1}{B}\frac{d\Pi}{da} = -\frac{1}{B}(\frac{dU}{da})_u = -\frac{1}{B}\left(\frac{Pdu}{2da}\right) = -\frac{u}{2B}(\frac{dP}{da}) \qquad \text{Eq. 3.43}$$

$$P = \frac{u}{C} \qquad \text{Eq. 3.44}$$

$$G = -\frac{u^2}{2B}\left(\frac{d(\frac{1}{C})}{da}\right) = \frac{u^2}{2B}\left(\frac{1}{C^2}\frac{dC}{da}\right) = \frac{u^2}{2B}\left(\frac{P^2 dC}{u^2 da}\right) = \frac{P^2}{2B}\left(\frac{dC}{da}\right) \quad \text{Eq. 3.45}$$

As a result:

$$G = \frac{P^2}{2B}(\frac{dC}{da}) \quad \text{Eq. 3.46}$$

It is clear that there is no difference in the driving force considering load or displacement control.

The energy release rate depends on the loading and configuration of the crack. For instance, for an infinite plate the G-a chart would be the one shown in Figure 3.16.

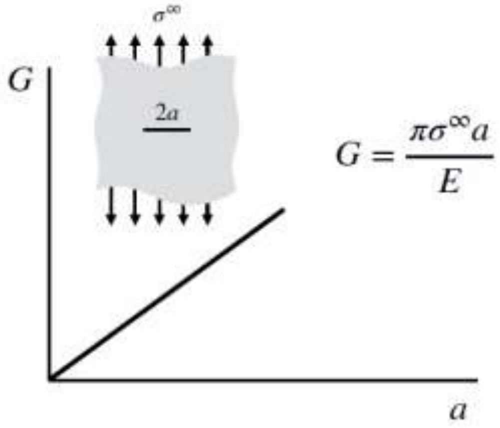

Figure 3.16: G-a chart of a crack happened on an infinite plate.

The resistance curve (R-curve) is a plot of the resistance of the material to crack propagation as a function of crack size (see figure 3.17). In this case, once the condition for growth is achieved, there will be an unstable catastrophic failure since G is always larger than the toughness.

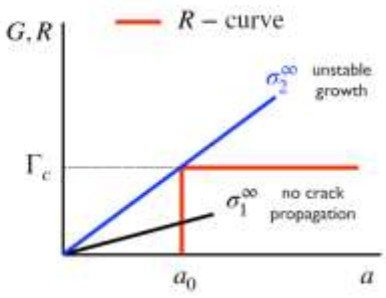

Figure 3.17: R-curve of the crack growth.

Figure 3.18 shows the behavior of a material that has a raising R-curve.

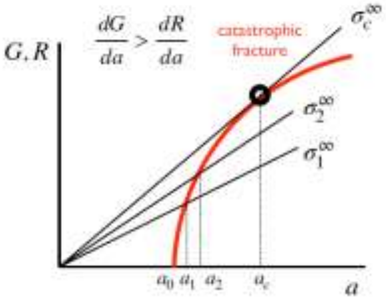

Figure 3.18: G,R-a chart at dG/da>dR/da situation.

In this case the crack is stable if $\frac{dG}{da} \leq \frac{dR}{da}$, else it is unstable. It follows that a material with R-curve behavior has not a unique value of fracture toughness. The tangency point will depend on the configuration of the structure.

The strain energy release of a DCB test is determined based on Eq. 3.46,

$$G = \frac{P^2 a^2}{BEI} \qquad \text{Eq. 3.47}$$

Whereby the compliance as determined from beam theory has been used:

$$u = \frac{Pa^3}{3EI} \qquad \text{Eq. 3.48}$$

$$C = \frac{2u}{P} = \frac{2a^2}{EI} \qquad \text{Eq. 3.49}$$

Where u is the displacement of loading beam, I is moment inertia, and E is Young's Modulus (see Figure 3.19)

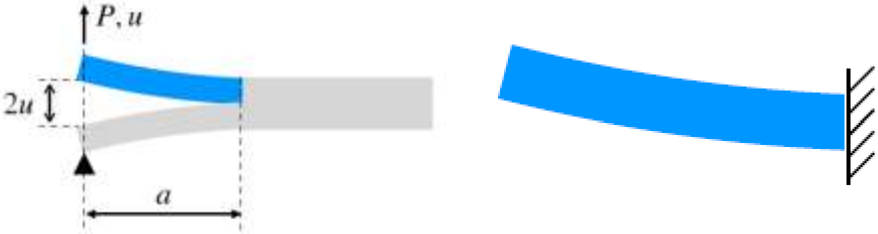

Figure 3.19: Determination of the compliance of a cantilever beam.

It follows that:

$$P = \frac{3EIu}{2a^3} \qquad \text{Eq. 3.50}$$

Therefore, the strain energy release of a DCB can also be written as:

$$G = \frac{9EIu^2}{4Ba^4} \qquad \text{Eq. 3.51}$$

The relationship between *G* and *a* is reported in Figure 3.20 for both load and displacement control. Based on the above discussion, it should be apparent that displacement control would provide a stable crack extension. In the present work, displacement control was selected to obtain significant amount of stable crack propagation.

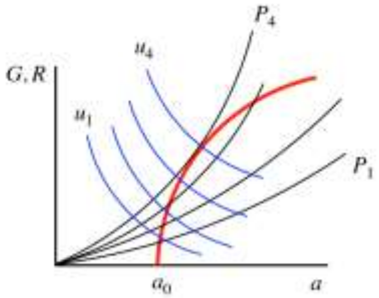

Figure 3.20: R-curve of a DCB test

3.5.2 Mode I fracture tests

DCB tests were carried out using a servo-hydraulic test frame with an MTS Flex Test SE controller. The schematic of the DCB test is shown in Figure 3.21. The pre-crack length of the DCB specimens are reported in Tab. 3.6. The load cell on the test frame had a capacity 2.2 kN, and the fixtures can be replaced to fit the samples, see Figure 3.22. Two DLSR cameras were employed in the tests, which were positioned orthogonal to the DCB specimen. One camera focuses on the side view of CFRP specimens to track the crack propagation during the tests. The other camera focuses on the connection between the fixture and sample to track the applied opening displacement. Each DLSR camera was imaged at a resolution of 1280 × 720 pixels with a frame rate of 60 fps. The loading speed applied on the tests was 0.1 mm/s.

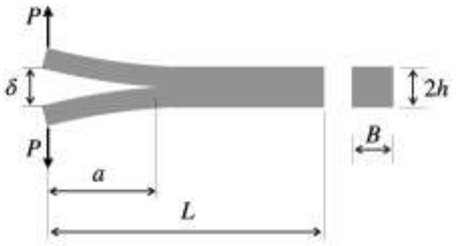

Figure 3.21: Schematic of DCB test

Table 3.6: DCB specimens pre-crack length including adhesive and surface treatment.

07333	Batch 1	B1S1	B1S2		
MS	Pre-crack length [mm]	32.5	32.5		
07333	Batch 2	B2S1	B2S2	B2S3	
MS	Pre-crack length [mm]	32.5	32.5	32.5	
07333	Batch 3	B3S1	B3S2	B3S3	
LS	Pre-crack length [mm]	42.2	39.4	42.5	
07333	Batch 4	B4S1	B4S2		
LS	Pre-crack length [mm]	37	37.5		
DP190	Batch 5	B5S1	B5S2	B5S3	
MS	Pre-crack length [mm]	32.5	32.5	32.5	
DP190	Batch 6	B6S1	B6S2	B6S3	
MS	Pre-crack length [mm]	38	38	40.6	
DP190	Batch 7	B7S1	B7S2	B7S3	
MS	Pre-crack length [mm]	31.5	33	31.5	
DP190	Batch 8	B8S1	B8S2	B8S3	B8S4
MS	Pre-crack length [mm]	20.5	23	23.1	23

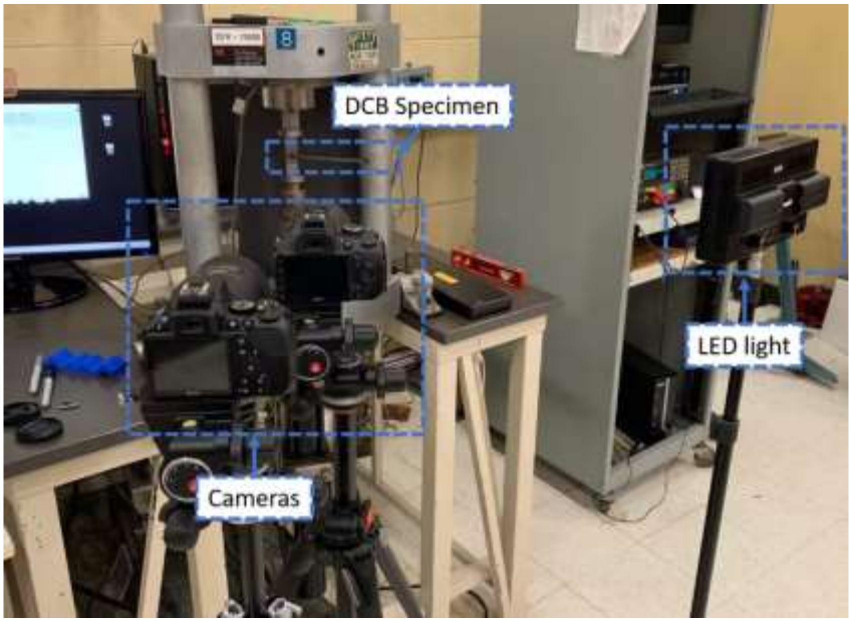

Figure 3.22: Experimental set-up for Mode I DCB tests employed in the present study and available at University of Waterloo E3-2106.

To calculate the fracture toughness of DCB test samples, de Moura et al. [100] provided a feasible solution to calculate the Mode I fracture toughness without tracking the crack propagation length (a). The strain energy in the beams can be calculated as:

$$U = 2[\int_0^1 \frac{M^2}{2E_{11}I}dx + \int_0^a \int_{-h/2}^{h/2} \frac{\tau}{2G_{12}} Bdydx] \qquad \text{Eq. 3.52}$$

Based on Castigliano's theorem:

$$\delta = \frac{\partial U}{\partial P} = \frac{8Pa^3}{E_{11}Bh^3} + \frac{12Pa}{5BhG_{12}} \qquad \text{Eq. 3.53}$$

We can calculate the compliance as:

$$C = \frac{\delta}{P} = \frac{8a^3}{E_{11}Bh^3} + \frac{12a}{5BhG_{12}} \qquad \text{Eq. 3.54}$$

The size of the fracture process zone (FPZ) and the root rotation are accounted for by augmenting the crack length, i.e., introducing the equivalent crack length:

$$a_e = a + |\Delta| + a_{FPZ} \qquad \text{Eq. 3.55}$$

Replace a with a_e in the above equation for C:

$$0 = \frac{8a_e^3}{E_{11}Bh^3} + \frac{12a_e}{5BhG_{12}} - C \qquad \text{Eq. 3.56}$$

By introducing parameters:

$$\alpha = \frac{8P}{E_{11}Bh^3} \qquad \text{Eq. 3.57}$$

$$\beta = \frac{12P}{5BhG_{12}} \qquad \text{Eq. 3.58}$$

$$\gamma = -C \qquad \text{Eq. 3.59}$$

So, it can be substituted as

$$\alpha a_e^3 + \beta a_e + \gamma = 0 \qquad \text{Eq. 3.60}$$

To calculate the revised Young's modulus E_f to replace the E_{11}Assume the crack propagation has not start yet ($a = a_0$), the compliance can be:

$$C_0 = \frac{8(a_0 + |\Delta|)^3}{E_f B h^3} + \frac{12(a_0 + |\Delta|}{5BhG_{12}}$$ Eq. 3.61

E_f can be derive as:

$$E_f = \frac{8(a_0 + |\Delta|)^3}{Bh^3}[C_0 - \frac{12(a_0 + |\Delta|)}{5BhG_{12}}]^{-1}$$ Eq. 3.62

Where,

$$\Delta = h\sqrt{\frac{E_f}{G_{12}}(3 - 2\xi^2)}$$ Eq. 3.63

$$\xi = \frac{\Gamma}{\Gamma + 1}$$ Eq. 3.64

Iterative solution was employed to solve the E_f and the compliance will be

$$\Gamma = 1.18\frac{\sqrt{E_f E_2}}{G_{12}}$$ Eq. 3.65

The final fracture toughness equation is:

$$G_I = \frac{6P^2}{B^2 h}(\frac{2a_e^2}{E_f h^2} + \frac{1}{5G_{12}})$$ Eq. 3.66

3.5.3 Mode II fracture tests

The facility used for ENF tests is a servo-hydraulic test frame with an MTS Flex Test SE controller. The schematic of the ENF test shows in Figure 3.23.

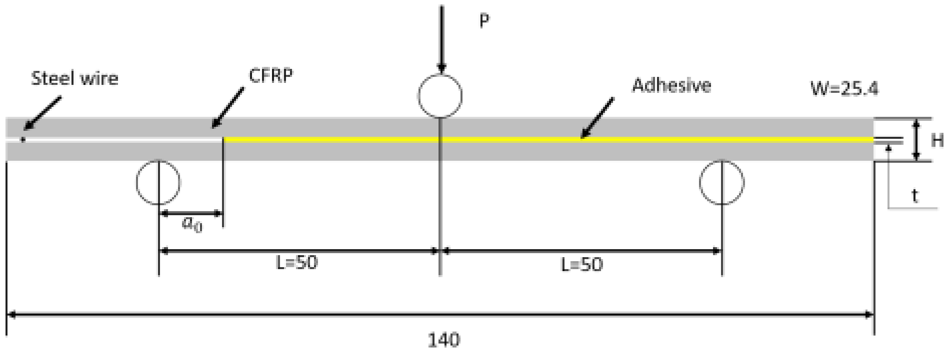

Figure 3.23: Schematic of the ENF test specimen.

Before testing, the ENF samples need to be pre-cracked. The specimens' pre-crack lengths are given in Tab. 3.7.

Table 3.7: Pre-crack length of each ENF specimen.

Batch 1	B1S1	B1S2	B1S3	B1S4	B1S5	B1S6
Pre-crack length [mm]	25	25	25	25	25	25
Batch 2	B2S1	B2S2	B2S3	B2S4	B2S5	B2S6
Pre-crack length [mm]	24	26	23.5	23.5	24	23.5
Batch 3	B3S1	B3S2	B3S3			
Pre-crack length [mm]	32	30	30			

The load cell on the test frame had a capacity of 5 kN, and the fixtures can be replaced to fit the samples, see Figure 3.24. Two DLSR cameras were employed in the tests, which were positioned orthogonal to the ENF specimen. One camera focuses on the side view of CFRP specimens to track the crack propagation during the ENF tests. The other camera focuses on the top surface of the specimen next to the loading pin to monitor any surface damage developing during the tests. Each DLSR camera recording was imaged at a resolution of 1280 × 720 pixels with a frame rate of 60 fps. Before the test started, a steel wire was inserted at the end of the pre-crack zone to reduce the friction between the top and bottom substrate during the tests. Three distinct cross-head displacement rate were employed 0.1 mm/s, 5 mm/s, and 15 mm/s.

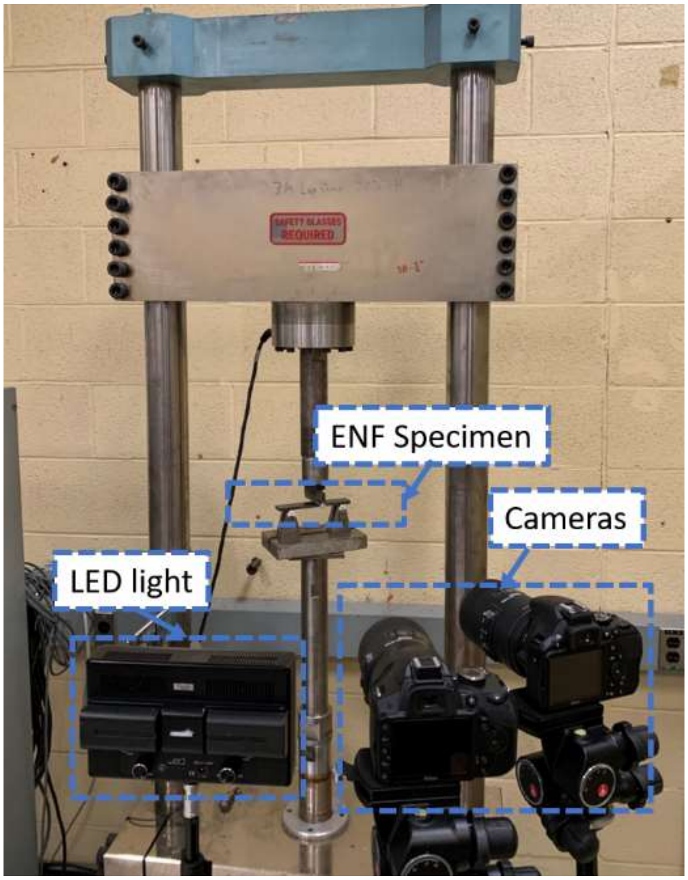

Figure 3.24: Experimental set-up for Mode II ENF tests employed in the present study and available at University of Waterloo E3-2106.

Similar to Mode I fracture toughness calculation, Castigliano's theorem was used to obtain the compliance as:

$$C = \frac{\delta}{P} = \frac{3a^3 + 2L^3}{8E_{11}Bh^3} + \frac{3L}{10BhG} \qquad \text{Eq. 3.67}$$

Therefore, the energy release rate will be:

$$G_{II} = \frac{P^2}{2B}\frac{dC}{da} = \frac{9P^2a^2}{16E_{11}B^2h^3} \qquad \text{Eq. 3.68}$$

Once again, a correction was applied to the Young's modulus; before any crack propagation ($a = a_0$) the compliance reads as:

$$C_0 = \frac{3a^3 + 2L^3}{8E_f Bh^3} + \frac{3L}{10BhG} \qquad \text{Eq. 3.69}$$

Thus, a corrected Young's modulus can be calculated as:

$$E_f = \frac{3a^3 + 2L^3}{8Bh^3}(C_0 - \frac{3L}{10BhG})^{-1} \qquad \text{Eq. 3.70}$$

Similarly, the equivalent crack length a_{eq} can be obtained as follows:

$$C = \frac{3a_{eq}^3 + 2L^3}{8E_f Bh^3} + \frac{3L}{10BhG} \qquad \text{Eq. 3.71}$$

$$\frac{3a^3+2L^3}{8E_{11}Bh^3} = C - \frac{3L}{10BhG} = C_{corr}, \qquad \text{Eq. 3.72}$$

$$3a_{eq}^3 + 2L^3 = 8E_f Bh^3 C_{corr} \qquad \text{Eq. 3.73}$$

However:

$$E_f = \frac{3a_0^3+2L^3}{8Bh^3}(C_0 - \frac{3L}{10BhG})^{-1} \qquad \text{Eq.3.74}$$

$$3a_{eq}^3 + 2L^3 = 8E_f Bh^3 C_{corr} = 8 * \frac{3a_0^3 + 2L^3}{8Bh^3}(C_0 - \frac{3L}{10BhG})^{-1} * Bh^3 C_{corr} \qquad \text{Eq. 3.75}$$

It follows:

$$a_{eq} = \left[\alpha a_0^3 + \frac{2}{3} L^3 (\alpha - 1)\right]^{\frac{1}{3}} \quad \text{Eq. 3.76}$$

Summing up, the Mode II fracture toughness can be calculated as

$$G_{II} = \frac{9P^2 a_e^2}{16 E_f B^2 h^3} \quad \text{Eq. 3.77}$$

Where,

$$E_f = \frac{3a_0^3 + 2L^3}{8Bh^3} (C_0 - \frac{3L}{10BhG})^{-1} \quad \text{Eq. 3.78}$$

$$\alpha = \frac{C_{corr}}{C_{0,corr}} \quad \text{Eq. 3.79}$$

3.6 Analysis of damage mechanisms

3.6.1 Microscopy

Surface characteristics after treatment was analyzed by microscope Keyence VHX-5000 Opto Digital Microscope (Canada) at the University of Waterloo Forming and Crash laboratory. The picture of microscope is provided below (Figure 3.25).

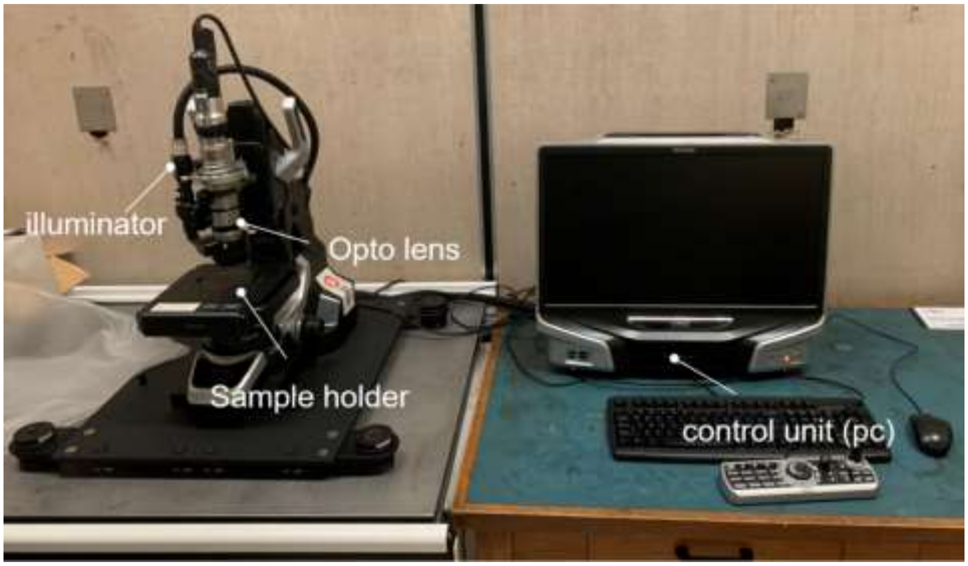

Figure 3.25: Keyence VHX-5000 Opto-Digital Microscope used for surface observation available at University of Waterloo E3-2106-d.

3.6.2 X-Ray CT analysis of substrate damage

Potential damage within the CFRP adherents following mechanical tests was analyzed using X-Ray computed tomography (X-Ray CT) executed with the ZEISS Xradia Versa 520 available at University of Waterloo within the MSAM laboratory. A picture of the system is provided below (Figure 3.26).

Figure 3.26: ZEISS Xradia Versa 520 X-Ray CT cabinet used to assess damage within the CFRP substrates.

Samples with dimensions 2.5 mm × 2.5 mm × 25.4 mm were extracted for selected substrates after testing. The following settings and Fig. 3.27 were used to extract CT images from the samples:

- Source Voltage: 40 kV
- Source Wattage 3 W
- Source-to-sample distance: 20.1166 mm
- Detector-to-sample distance: 133.3032 mm
- Pixel size: 9.0019 µm
- Optical magnification: 0.39328
- Exposure time: 4.0 seconds
- Source filter: Air

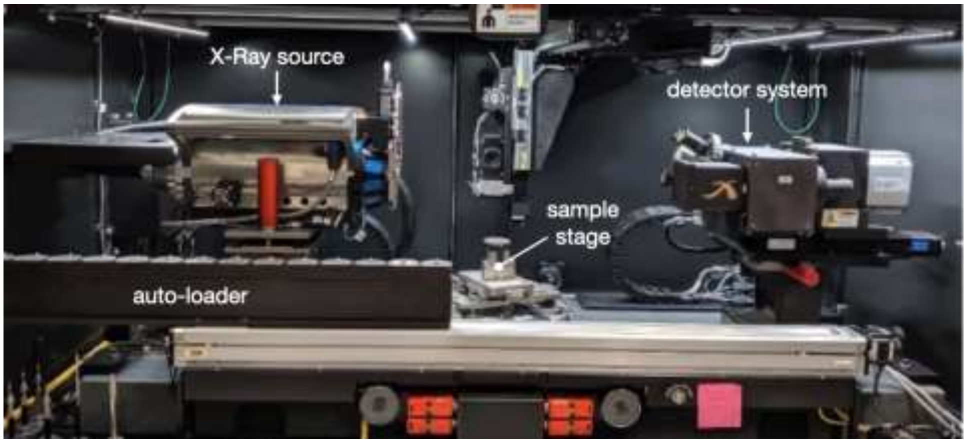

Figure 3.27: ZEISS Xradia Versa 520 machine used for CFRP X-ray scan available at University of Waterloo E7-3419

Chapter 4: Experimental results

In this chapter, the results and outcomes of surface treatments are presented. Contact angle measurements, surface mapping, surface roughness and the determination of surface energy will be presented in section 4.1. The results of DCB and ENF mechanical tests performed to characterize the Mode I and Mode II fracture toughness for NCF-CFRP joints featuring the 3M 07333 adhesive will be presented in section 4.2. The results of DCB tests performed to characterize the Mode I fracture toughness for NCF-CFRP joints with adhesive DP190 will be presented in section 4.3.

4.1 Analysis of surface pre-treatments

4.1.1 Surface morphology and topography

In order to assess the effect of surface pre-treatments small plates of dimensions 25 mm × 25 mm were cut from NFC-CFRP panels using water-jet. The sanding process was described earlier in Section 3.2.1. In particular, the baseline surface was compared with a sanding process lasting either 1 min (S1) or 2 mins (S2), respectively. Microscopy images of the corresponding treated surfaces are shown in Fig. 4.1.

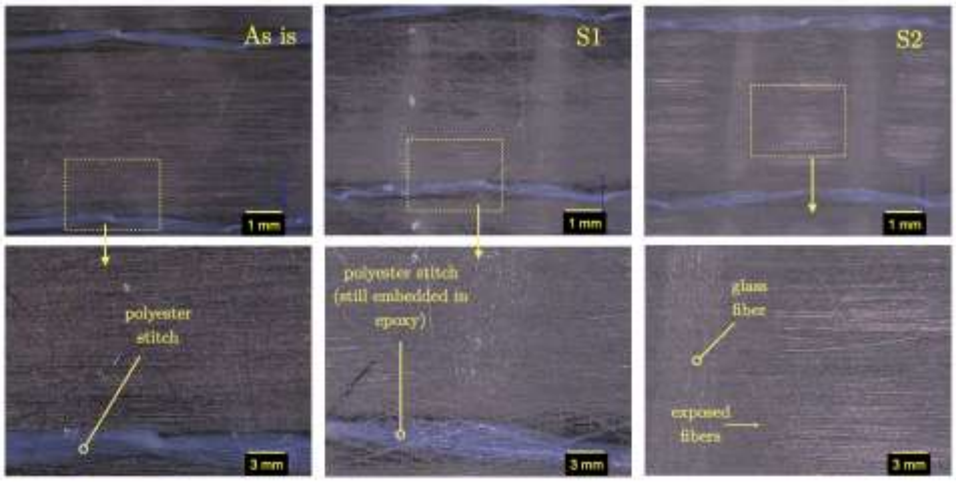

Figure 4.1: Microscopy images of the NCF-CFRP plates before and after sanding.

The original as-produced surface appears relatively smooth, and the presence of polyester stitches can be readily observed from visual inspection since the epoxy matrix was optically translucent. After sanding (S1), the stitches are still embedded within a thin epoxy layer, while the glass fibers become more visible. With prolonged standing (S2), the glass fibers are further exposed, and so are the carbon fibers, although they appear to be well anchored to the epoxy matrix. Notice that exposure of glass fibers was variable across the treated surface since the thickness of surface epoxy matrix layer was not uniform within the CFRP plates. Figure 4.2 shows the characteristics of CFRP surfaces after UV laser treatment executed at a different frequency and laser scanning speed. Xu et al. [101][101] reported that in the ablation process of CFRP panels carried out with a 355 nm short pulse laser, the heat-affected zone and matrix removal depended on the laser scanning direction. In particular, they have shown that when the laser scanning is aligned with the fiber direction, the degradation/removal of the epoxy matrix is more significant. Likewise, in this study, the scanning direction was aligned with that of the carbon fibers to promote better control of material removal and investigate the effect on mechanical performances.

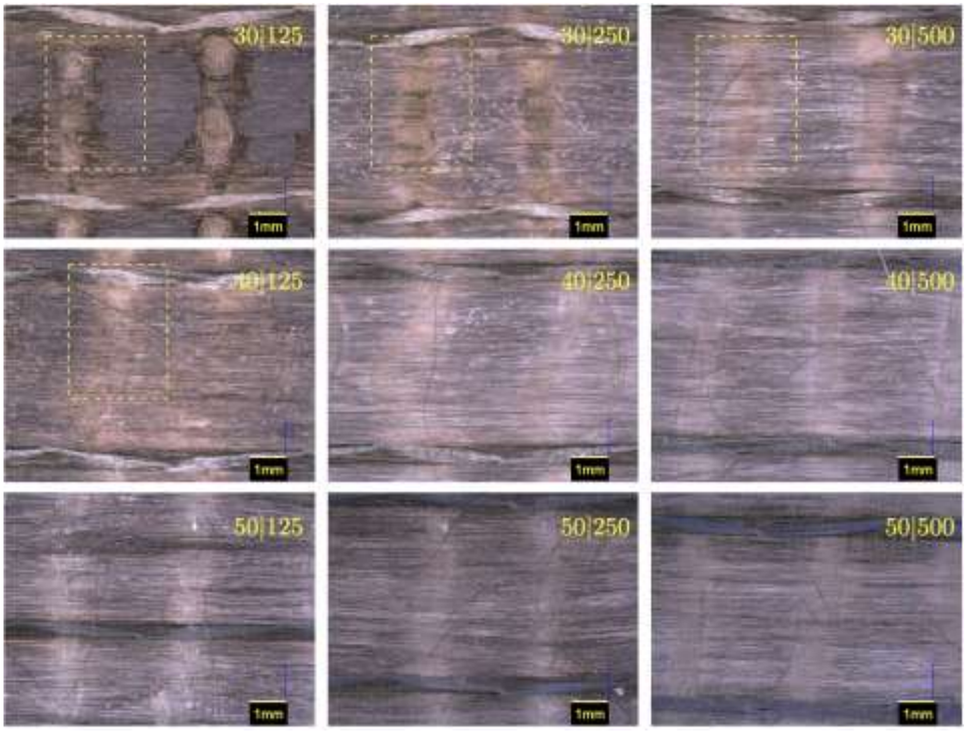

Figure 4.2: Surface characteristics of UV laser treatment at different frequency and moving speed.

It is clear that as both processing variables increase, the effect of the laser beam becomes less apparent. At the lowest pulse frequency and scanning speed (i.e., 30|125), the epoxy resin on the surface was removed to an extent that carbon fibers were exposed and clearly visible. However, the heterogeneous composition of the composite surface, including epoxy, carbon fibers, polyester, and glass, has led to uneven material removal and the formation of a heat-affected zone (HAZ). Examples are given in Fig. 4.2 within the area enclosed by the dashed rectangle - although only at 30|125 exposed carbon fibers could be clearly discerned from optical observations.

Images with higher magnification are reported in Fig. 4.3 and highlight details of the modified surfaces. In particular, it is confirmed the removal of the epoxy matrix accomplished at the lowest pulse frequency, while it is not straightforward to state whether it was removed for the other cases. Furthermore, for the case 30|125, the removal of the epoxy was not uniform since apparent residuals were observed next to the supporting glass fibers (see the horizontal arrows in Fig. 4.3). Polyester stitches can absorb the UV laser wavelength and, as such, these were affected by the laser beam resulting in apparent damage, see, for instance, 40|125 in Fig. 4.3.

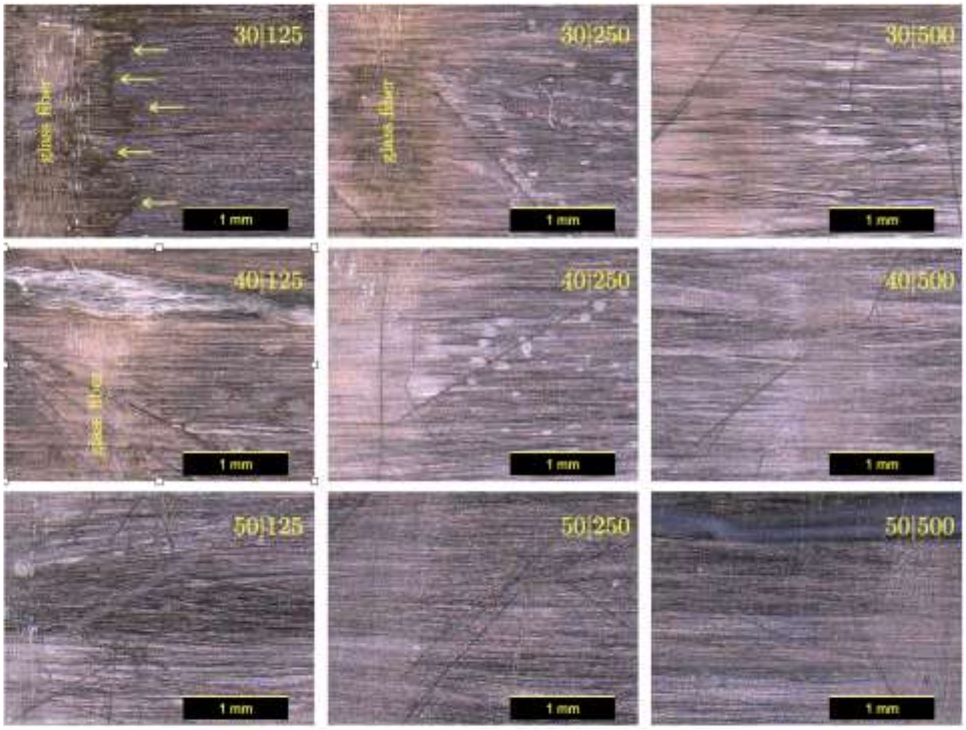

Figure 4.3: Close-up view of the images shown on Fig. 4.2.

The translucent nature of the epoxy matrix leaves some degree of uncertainty concerning the actual condition of the treated surfaces after laser ablation. Additional analyses were made using a confocal microscope to extract topography information. Typical results are shown in Fig. 4.3 in the form of 3D maps and confirm that exposed fibers are clearly visible with a laser ablation carried out at 30 kHz and 125 mm/s. One concludes that in all other cases, the exposure of carbon fibers was limited, as shown by the optical images.

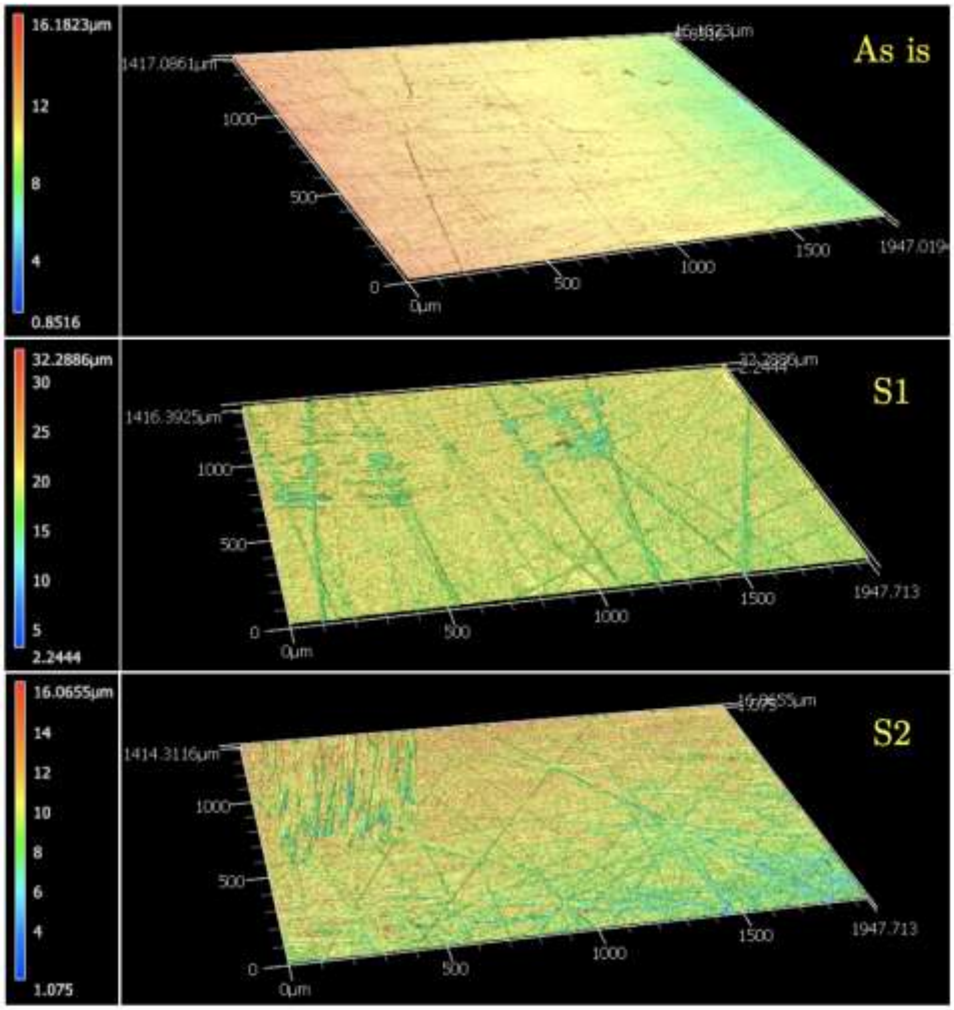

Figure 4.4: Confocal microscopy images of the target surface before and after surface preparation (S1: sanding 1’; S2: sanding 2’; X|Y: pulsed laser ablation at X frequency (kHz) and Y scanning speed (mm/s).

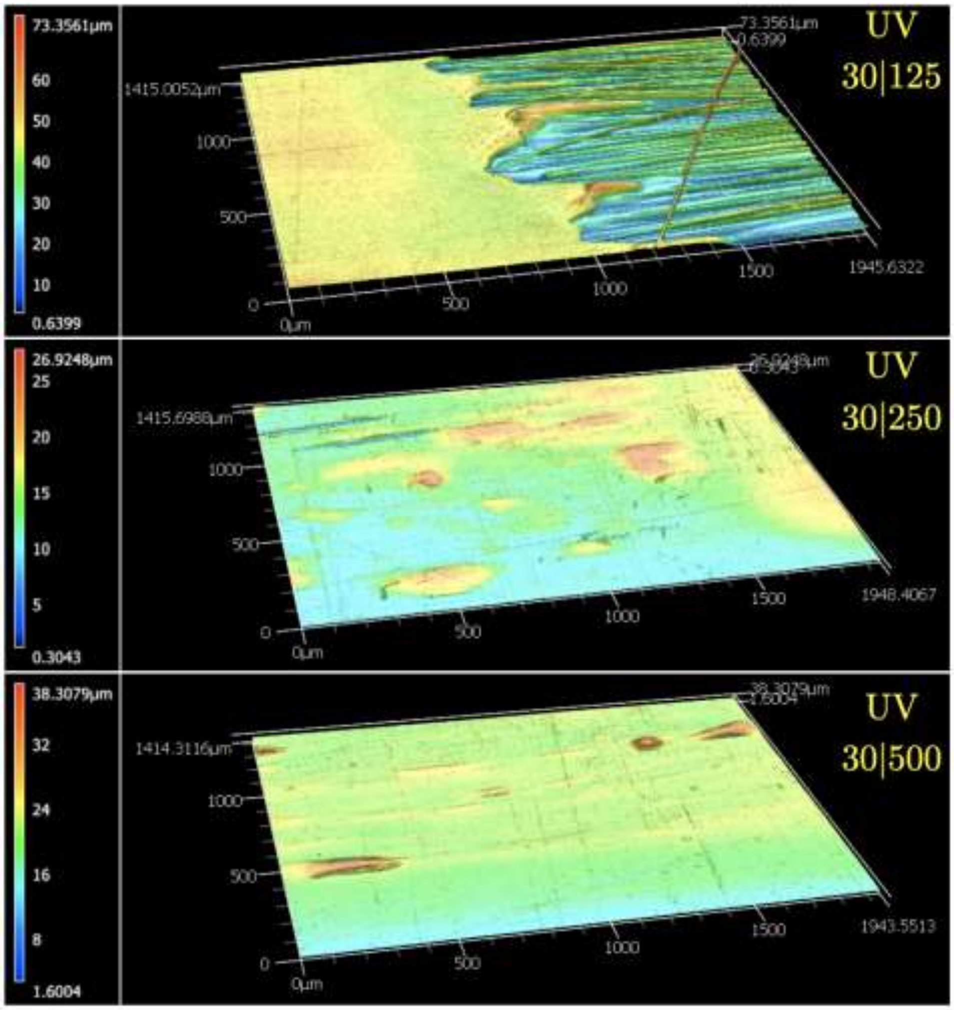

Figure 4.4: (cont.)

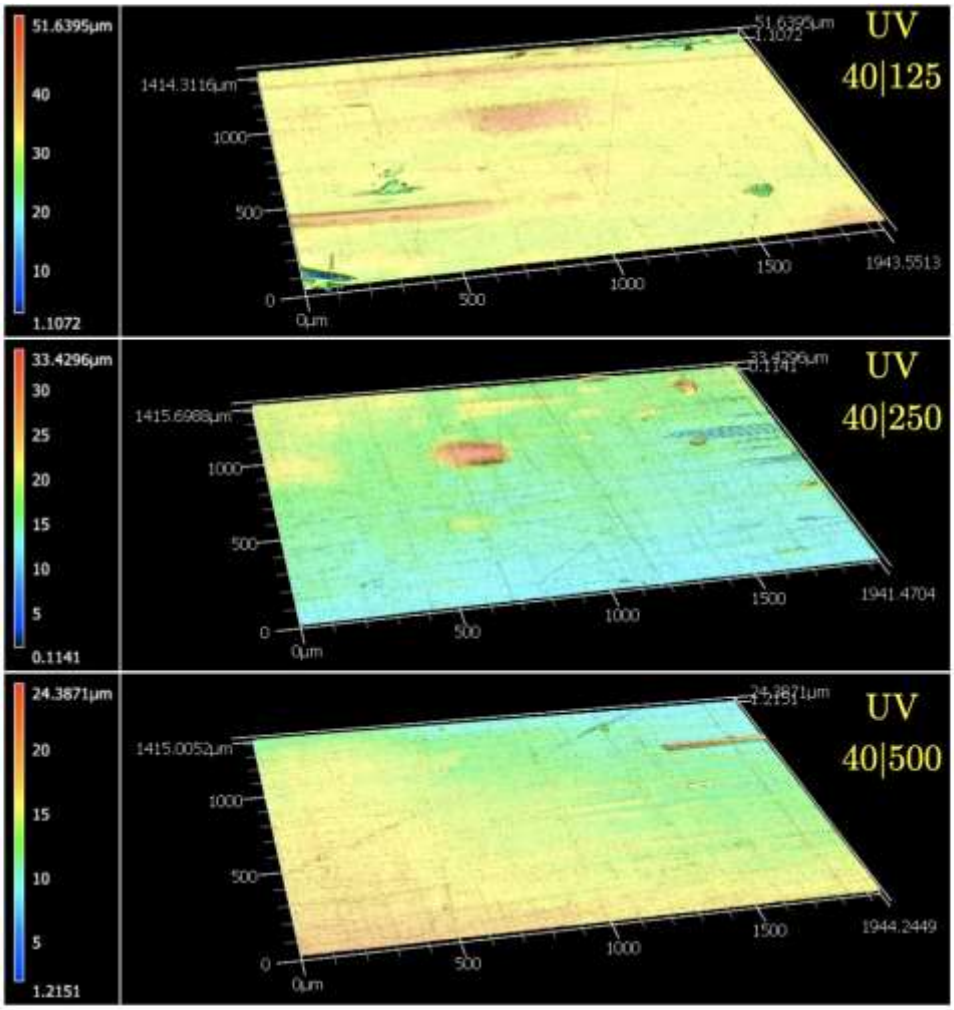

Figure 4.4: (cont.)

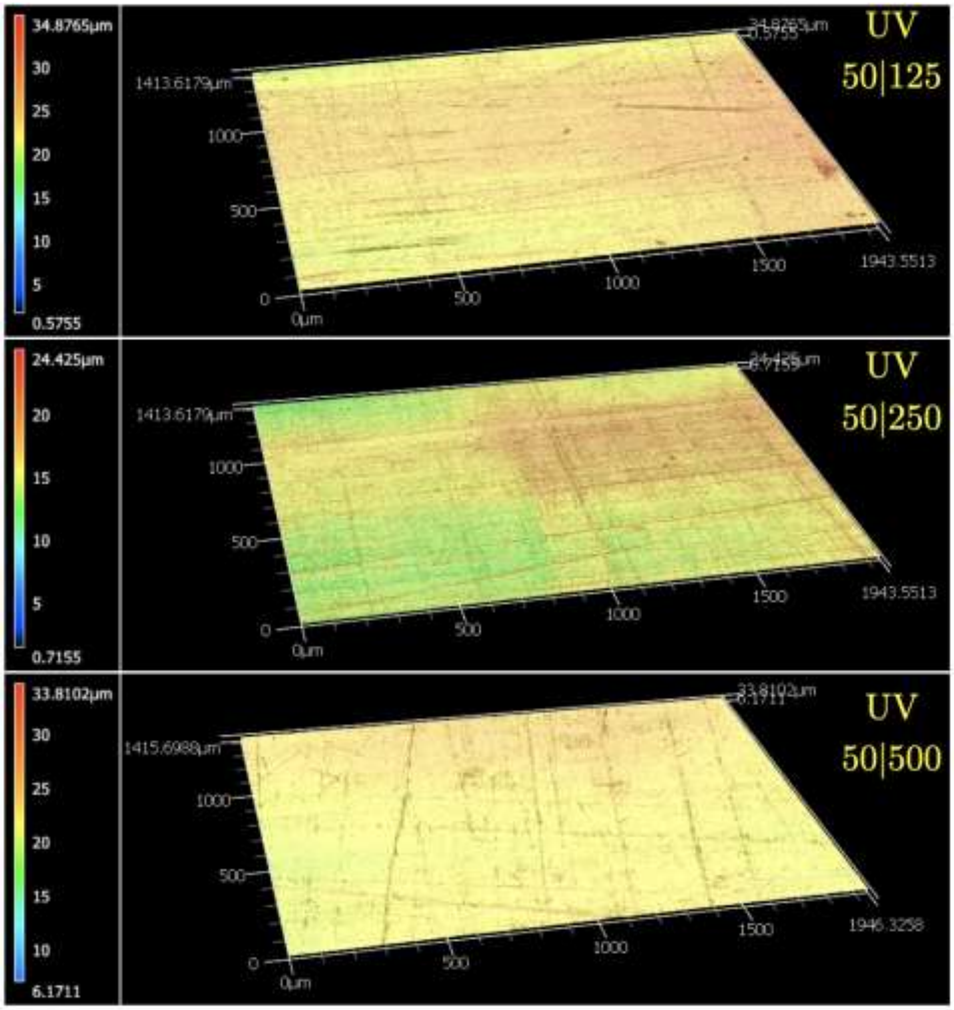

Figure 4.4: (cont.)

Beside the morphological information, the following metrics were extracted from the 3D maps like those shown in Fig. 4.4:

- S_a: the extension of R_a (arithmetical mean roughness value) to a surface.
- S_z: sum of the largest peak height value and the largest pit depth value within the defined area.
- S_{dr}: percentage of additional surface area contributed by the texture (compared to the planar definition area or projected area).

The results obtained for the above metrics are summarized in Tab. 4.1. The profilometry analysis indicates that the average surface roughness of the baseline composite surface decreases after the sanding. Notice that the surface roughness factor (r), defined as the ratio between the actual area (A) of the texture divided by the projected area (A_0), can be obtained from knowledge of S_{dr}. This is further discussed later, while the corresponding values are appended in Tab. 4.1. The analysis of the roughness factor indicates that the texture associated with the sanding process provided additional surface area.

Table 4.1: Surface roughness of CFRP samples with different surface treatment.

	S_a (μm)	S_z (μm)	S_{dr}	$r = \frac{A}{A_0} = 1 + S_{dr}$
As is	1.5	15.58	0.06	1.06
S1	1.26	30.56	0.31	1.31
S2	1.19	15.2	0.29	1.29
UV 30 | 125	8.84	72.65	0.73	1.73
UV 30 | 250	2.32	26.72	0.09	1.09
UV 30 | 500	1.58	37.00	0.15	1.15
UV 40 | 125	1.97	50.30	0.12	1.12
UV 40 | 250	1.84	32.79	0.15	1.15
UV 40 | 500	1.77	24.74	0.12	1.12
UV 50 | 125	1.51	30.66	0.03	1.03
UV 50 | 250	1.31	17.54	0.01	1.01
UV 50 | 500	1.03	33.69	0.07	1.07

For the UV laser treatment, the degree of surface modification and ensuing metrics were sensitive to both pulse frequency and laser speed. However, the most significance changes were obtained at low pulse frequency and scanning speed.

4.1.2 Determination of static contact angles and surface free energy (SFE)

In order to ascertain the effect of surface treatment on the target surface, wettability measurements are an obvious choice because of the apparent simplicity [26], [27]. In this study the wettability of the as-produced (S0) and sanded NCF-CFRP was assessed using a contact angle goniometer, with deionized water (DW), formamide (F) and ethylene glycol (EG) probe liquids. Very small liquid drops (i.e., tens of microliters) were gently laid down such that they could flow and equilibrate with the surface. Typical results are reported in Fig. 4.5, which show typical outcomes of repeated measurements on as produced and sanded surfaces. The C.A. was determined using snapshots of the liquids drops such as those shown in Fig. 4.5 (d).

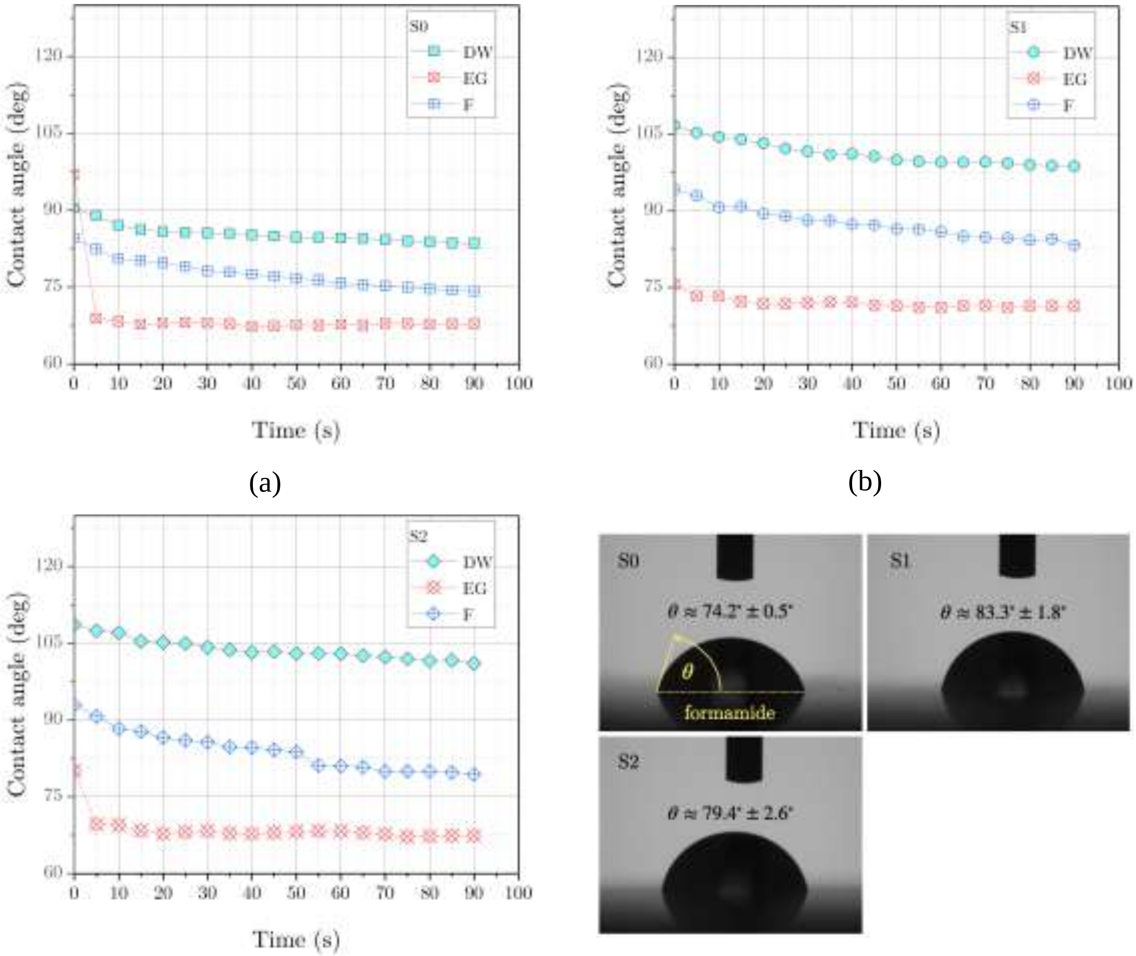

(a) (b)

(c) (d)

Figure 4.5: Evolution of contact angle (CA) as a function of time for the investigated NCF-CFRP surfaces: (a) S0; (b) S1; (c) S2. Each measurement was carried out using 3 probe liquids. (d) Snapshots of the C.A. recorded at 90 seconds from drop dispensing (probe liquid: formamide).

Multiple images were recorded over a time span of 90 seconds and were spaced apart by about 5 seconds. The acquisition speed and the number of images were limited by the hardware available for such measurements. It appears that the C.A. of DW and F keeps decreasing with time over the full observation window, while for EG the C.A. is relatively stable. Similar conclusions can be drawn for bot as produced and sanded surfaces, i.e., the measured C.A. keeps decreasing with time when DW and F are used.

In order to determine the SFE of the solid, some authors suggest determining the contact angle ensuring that the time elapsed from drop dispensing/placement and the actual measurement is as small as possible [102]. However, other authors have indicated that the equilibrium contact angles should be determined once transient effects, such as capillarity, are spread out [15]. It is unlikely that such procedures can afford a reliable estimate of surface energy with the data at hand. Indeed, the first procedure requires high-speed video recordings that were not available for this study. The results provided by the second one would also be uncertain because the C.A. of DW and F keep varying and do not seem to reach a steady state. Nevertheless, both procedures have been assessed, and the contact angles recorded at t=0 s and t=90 s have been supplied in the Owens-Wendt method to determine surface energy.

The results reported in Fig. 4.6 are referred to as the initial C.A., i.e., t=0 s. The first point to highlight is that the linear interpolations for S1 and S2 displayed a rather low correlation, with $R^2<0.5$ in both cases. Furthermore, the total surface energy would not exceed 18 mJ/m^2 and the polar component would be subject to a decrease from about 16 mJ/m^2 (S0) to 0.4 mJ/m^2 (S2). It should be noted that the so obtained total SFE would be lower than typical values reported in the literature [27]. The determination of surface energy using the second set of C.A., i.e., t=90 s, data is reported in Fig. 4.7. There is a substantial improvement in the correlation, as R^2 is >= 0.7. The so obtained surface energy would see an increasing dispersive component, from 12.3 mJ/m^2 (S0) to 27.4 mJ/m^2 (S2); however, the total energy would not increase much further because an increase of the dispersive component is once again counteracted by a decreasing polar part.

The obtained results raise some important questions concerning the interaction between the probe liquids and the complex NCF-CFRP surfaces. In performing measurement of the (static) contact angle it is assumed that the contact area between solid and liquid does not change during the measurement. That is, the drop is in a global energy equilibrium condition, i.e., a stable state that corresponds to the contact angle denoted in the Young's equation. Considering the results reported in Fig. 4.5, and the variation of C.A., one concludes that static measurements as determined on the NCF-CFRP surfaces do not provide reliable information about the liquid-solid interaction.

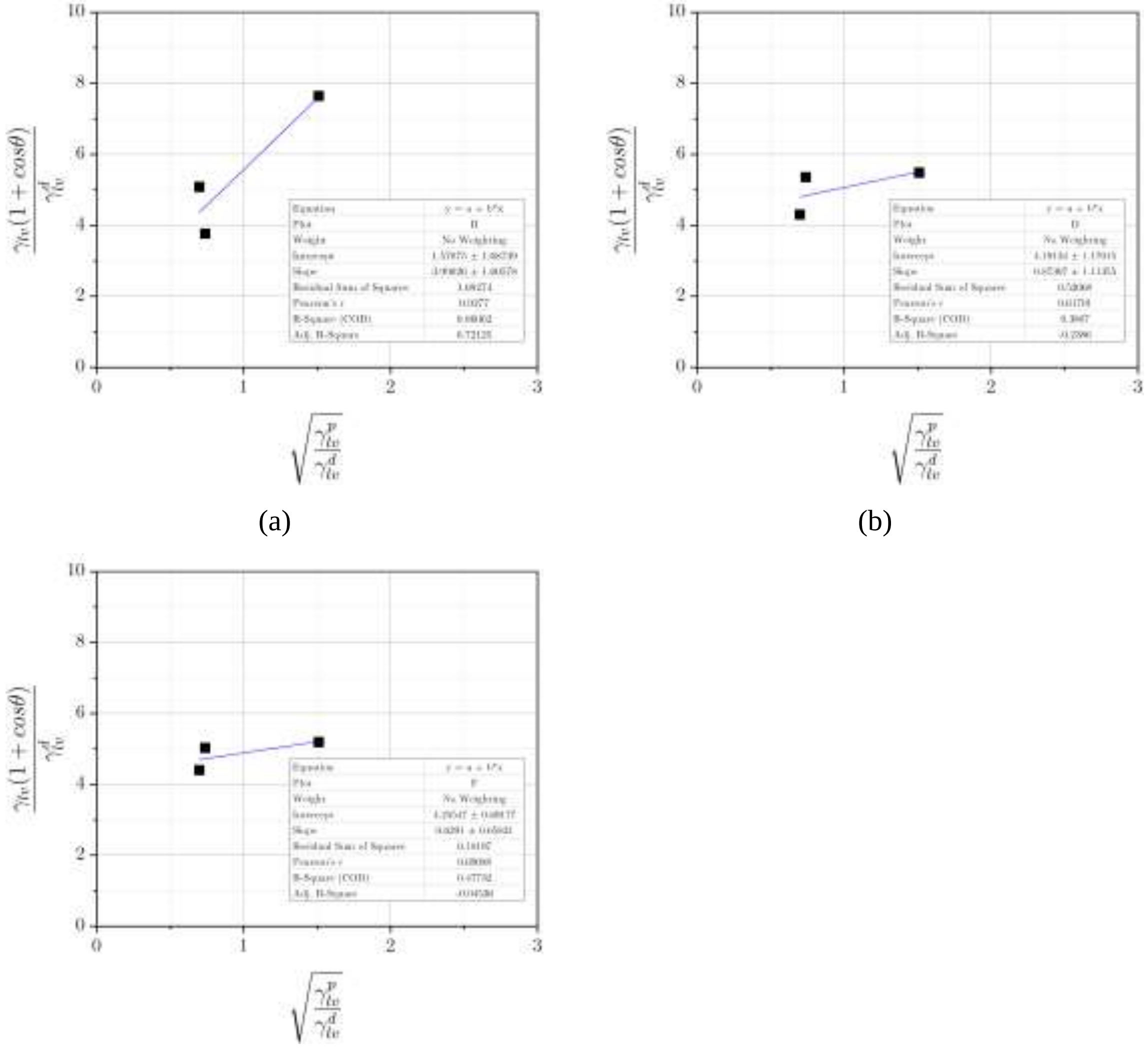

(a)

(b)

(c)

Figure 4.6: Determination of SFE by using the contact angles determined at t=0 s. (a) S0; (b) S1; (c) S2.

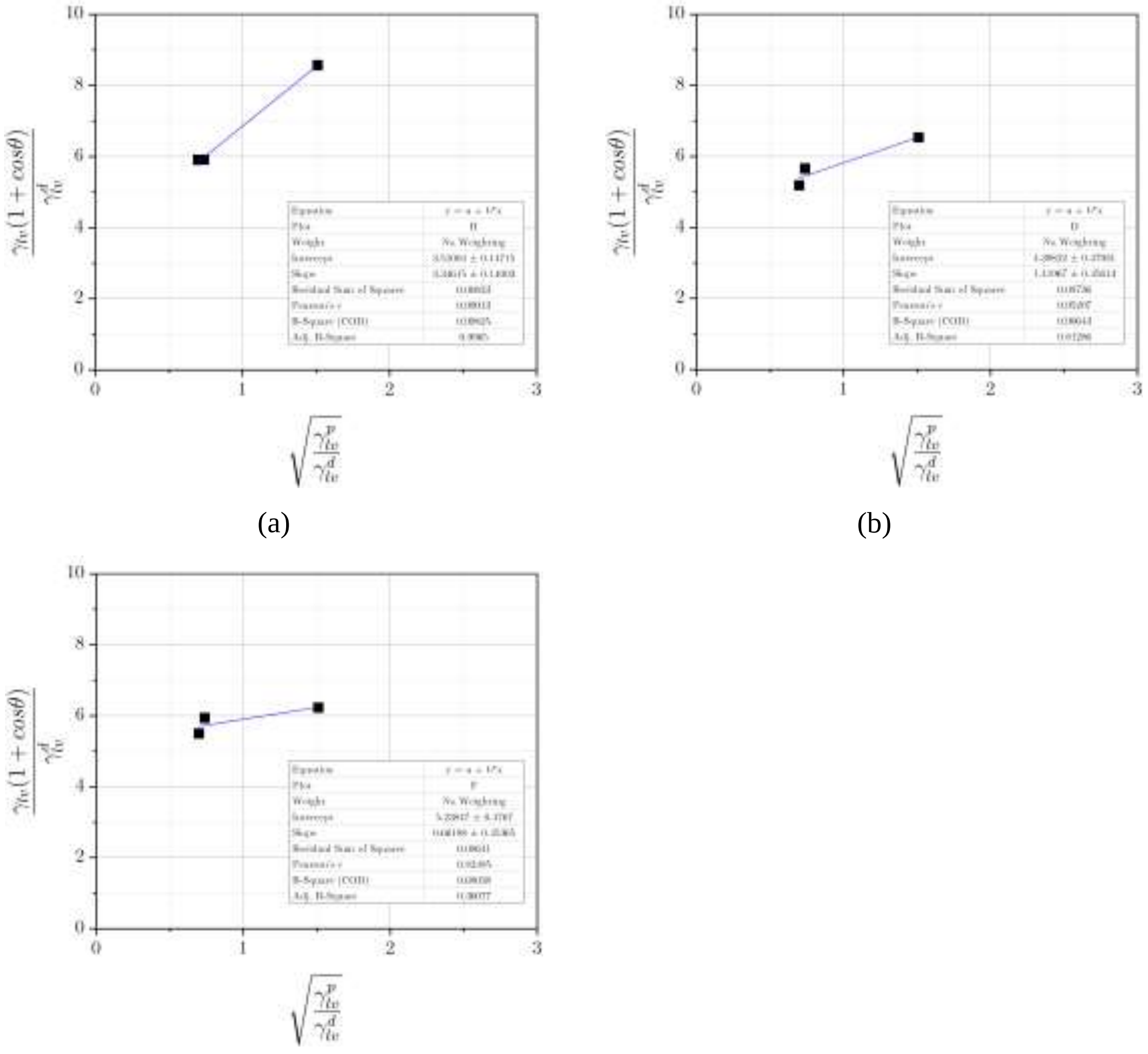

(a)

(b)

(c)

Figure 4.7: Determination of SFE by using the contact angles determined at t=90 s. (a) S0; (b) S1; (c) S2.

Moreover, it is observed that while the probe liquid should not react with the solid surface, it can still penetrate any small crevices or microcracks within a surface layer. This issue is particularly relevant for the measurements carried out herein, given the complex heterogeneous nature of composite surface, especially after sanding or laser ablation. Notice that the penetration of a probe liquid within the material depends on the liquid's molar volume, and the penetration slows down and decreases as the volume increases. The molar volume of the probe liquids employed in this study are given as follows: υ^{DW}=18.0 mL/mol, υ^{F}=39.8 mL/mol and υ^{EG}= 55.7 ml/mol. Therefore, while DW should be able to penetrate the surface structure more easily, for EG it should be somewhat more limited. These observations are fairly good agreement with the data are given in Fig. 4.5, which shows a relatively stable C.A. for EG, and a continuous decrease for both DW and F. As a matter of fact, the selection of probe liquids plays an important role toward obtaining reliable results because a liquid may interact with the target material and/or be subjected to volume reduction following evaporation. Considering the complexity of the treated surfaces, these results ruled out the possibility to obtain accurate estimate of the SFE, especially after surface pre-treatment.

4.1.3 Analysis of advancing contact angles

More robust and reproducible measurements are represented by the advancing and receding contact angles, also referred to with abbreviations A.C.A. and R.C.A., respectively. In this study, also the Greek symbols θ_a and θ_r are invariably used. These can be determined by increasing and decreasing, respectively, the droplet volume as shown in Fig. 4.8. By increasing the droplet volume, the contact angle of the drop will increase, and the contact line remains pinned until the A.C.A. or θ_a is reached. At that point, further increase of drop volume will lead to movement of the contact line, whereas the contact angle remains approximately constant.

(a) (b)

Figure 4.8: Schematic depiction of the procedure employed for the determination of (a)_A.C.A. and (b) R.C.A.

Similarly, by decreasing the drop volume, the contact line will remain pinned and the shape of the drop changes until the R.C.A. or θ_r is reached. Further decrease of drop volume will lead to movement of the contact line. In contrast, the so obtained contact angle remains ideally constant but can vary in measurements because of the non-uniformity of the sample. The difference between A.C.A. and R.C.A., namely the contact angle hysteresis, provides important information regarding the mobility of a liquid on a solid surface. As stated earlier, real surfaces do not have perfect smoothness or chemical homogeneity, and these deviations lead to hysteresis in the measured contact angles. The use of the A.C.A./R.C.A. overcomes metastable free energy spots usually due to surface roughness and while static drops may be affected by evaporation RCA/A.C.A. are virtually insensitive. For the A.C.A./R.C.A. measurements only DW was used. The probe liquid was added and withdrawn very slowly to avoid dynamic effects. Images of the drop profiles were taken every 5 s and selected snapshots taken during liquid dispensing / withdrawal are given in Fig. 4.9.

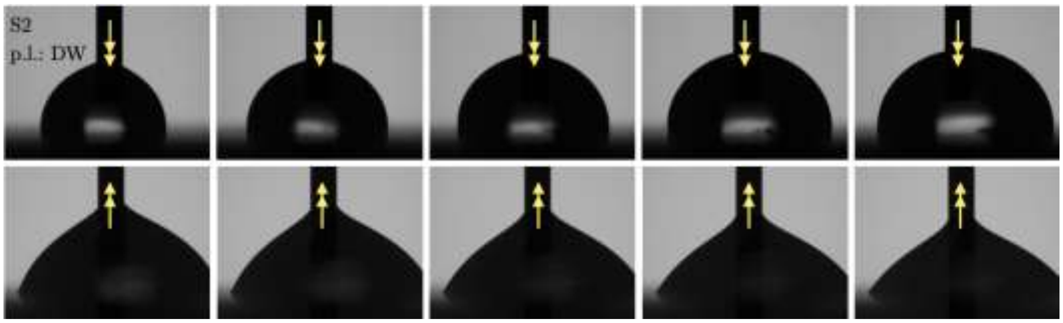

Figure 4.9: Typical snapshots recorded during the experiments. Notice that the R.C.A. was not achieved.

The R.C.A. was somewhat difficult to determine with accuracy. For instance, the images shown in Fig. 4.9 show that the R.C.A. was not achieved because the contact line remained pinned until the receding angle was too small to be measured accurately. Instead, the A.C.A. was obtained with greater accuracy and it was most reproducible with respect to the static measurement. The A.C.A. values for S0, S1 and S2 are reported in Fig. 4.10. The inset figure shows the superposition of two snapshots that highlight the movement of the contact line and the achievement of the ACA. Interestingly, the A.C.A. of all samples is relatively stable and increases slightly after sanding. The average values of the A.C.A. are also provided in the figure and indicate that the initial hydrophobic surface remains so after sanding.

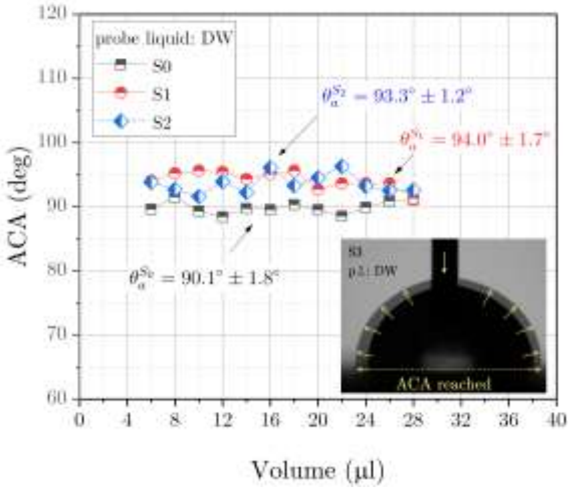

Figure 4.10: A.C.A. of sanded surfaces as determined using DW. The insert shows two snapshots of the liquid superimposed to highlight the achievement of the A.C.A. while the liquid is dispensed.

As discussed earlier, the sanding process increased the roughness of the samples and the apparent contact area (thus, it increased *r*). Considering the roughness data, it seems that the A.C.A. conforms with the Wenzel regime of wettability. Wenzel's model describes the homogeneous wetting regime, whereas the liquid is able to completely penetrate within surface asperities. The apparent C.A. of the liquid on a rough surface is given by:

$$cos\theta^{*} = rcos\theta \qquad \text{Eq.4.1}$$

Where *r* is the roughness factor, which is given by the ratio between actual and projected area of the solid (which was herein determined using optical profilometry, as shown previously). According to this model, if the intrinsic contact angle of the surface is θ<90, roughening will make the surface such that θ*< θ, and vice versa. The roughness factor was determined from surface mapping presented previously and is given as:

$$S_{dr} = \frac{1}{A}[\iint_{A} \left(\sqrt{1+\left(\frac{\partial z}{\partial x}\right)^{2}+\left(\frac{\partial z}{\partial y}\right)^{2}}\right) dxdy] \qquad \text{Eq.4.2}$$

besides, is should be noted that:

$$S_{dr} = \frac{A - A_0}{A_0} = \frac{A}{A_0} - 1$$ Eq.4.3

that implies:

$$r = 1 + S_{dr}$$ Eq.4.4

Using the above relation, one can correct the apparent contact angle (θ^*) and obtain the intrinsic one of the investigated surfaces. By doing so, the above quoted average values become: 90^o (S0), 93^o (S1) and 92.5^o (S2), respectively. The corrected values are obviously very similar to the apparent contact angles because of the limited variation of the surface factor induced by the sanding process. The overall analysis demonstrates that the NCF-CFRP surface is hydrophobic before and after sanding. Wettability measurements executed on the laser treated surfaces have essentially indicated a similar outcome, thereby suggesting that the execution of surface preparation can change morphology and topography of the target surfaces but do not necessarily improve wettability.

Therefore, further evaluations of the surface preparation methods were made directly performing mechanical tests. To this aim, the following treatments were selected for mechanical testing. For the sanding treatment it was selected S1 since there is no major difference in the surface metrics and topography of S1 and S2. Notice that bonding in the as produced conditions was not considered since a previous work carried out at University of Waterloo has shown that the results would provide unsatisfactory joint strength as determined in single lap joint tests [89]. Regarding the UV-laser ablation, an exploratory study was carried out considering 125 mm/s laser speed and pulse frequency 40 kHz (denoted as LS1 in what follows); this processing provided changes of surface metrics with respect to the baseline but did not expose carbon fibers. Besides, the UV-laser ablation at 125 mm/s and pulse frequency 30 kHz was also included in the analysis because the combination of process parameters provides exposed carbon fibers, and then one can assess the effect of exposed fibers on crack propagation and determine if damage occurred at the fiber/matrix interface following laser ablation. Such processing is denoted as LS2.

4.2 Mechanical tests of CFRP joints bonded with 3M 07333 epoxy adhesive

4.2.1 DCB tests and determination of Mode I fracture toughness

4.2.1.1 Effect of sanding

The load-displacement responses and the R-curves of DCB specimens prepared using a sanding treatment are presented in Fig. 4.11. The mechanical tests are displacement controlled at 0.1 mm/s. In general, considering that CFRP/epoxy joints display commonly a scattered response [89], the results reported herein are fairly consistent. In all tests, the load increases linearly and then it reaches a peak. After that, the propagation of a macroscopic crack is commenced (softening) and the applied load gradually decreases as the applied displacement increases. It should be noted that the DCB tests were stopped once the crack travelled approximately 80% of the bonded region. The remaining bondline was fractured using a wedge.

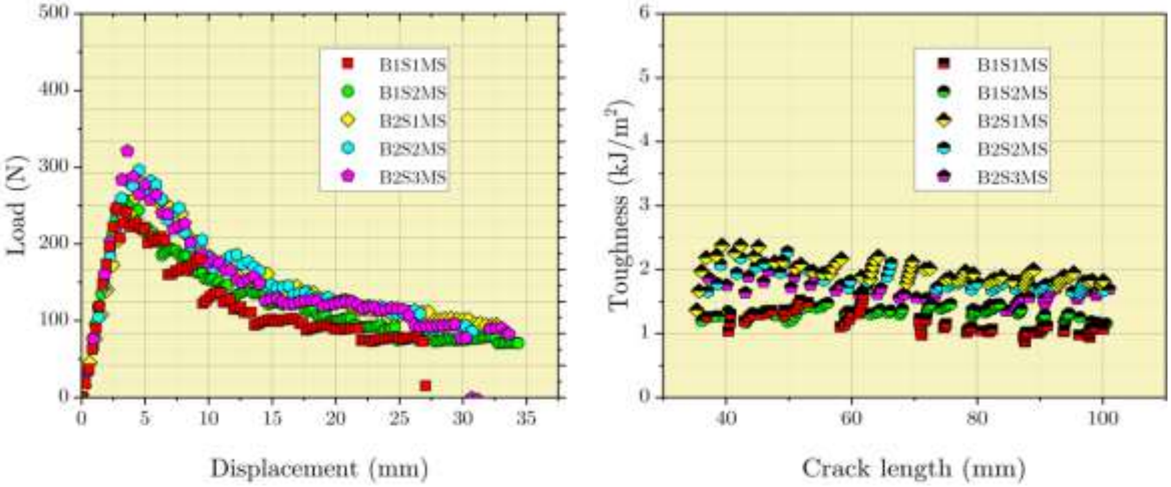

(a) (b)

Figure 4.11: (a) Load vs. displacement and (b) R-curves of the DCB specimens comprising sanded NCF-CFRP adherends (MS: manual sanding).

Load fluctuations during softening are mainly associated with the crack path through the joint. As shown in previous related works, crack growth in CFRP/epoxy joints can include the combination of cohesive fracture within the adhesive, but also interlaminar \ intralaminar fracture of the CFRP substrates, occasionally accompanied by fiber bridging [15]. The ensuing R-curves are relatively flat suggesting that fracture toughness was fairly constant across the probed portion of the bonded region.

Visual inspection of the fracture surfaces indicated that cohesive fracture was the main mechanism of failure in all tests, with the sole exception of B1S1. In particular, post-test images of the severed samples are provided in Fig. 4.12 and show some degree of both interlaminar and intralaminar fracture almost in all tests. In particular, the quoted % values in Fig. 4.12 refer to the degree of cohesive fracture as determined from image analysis.

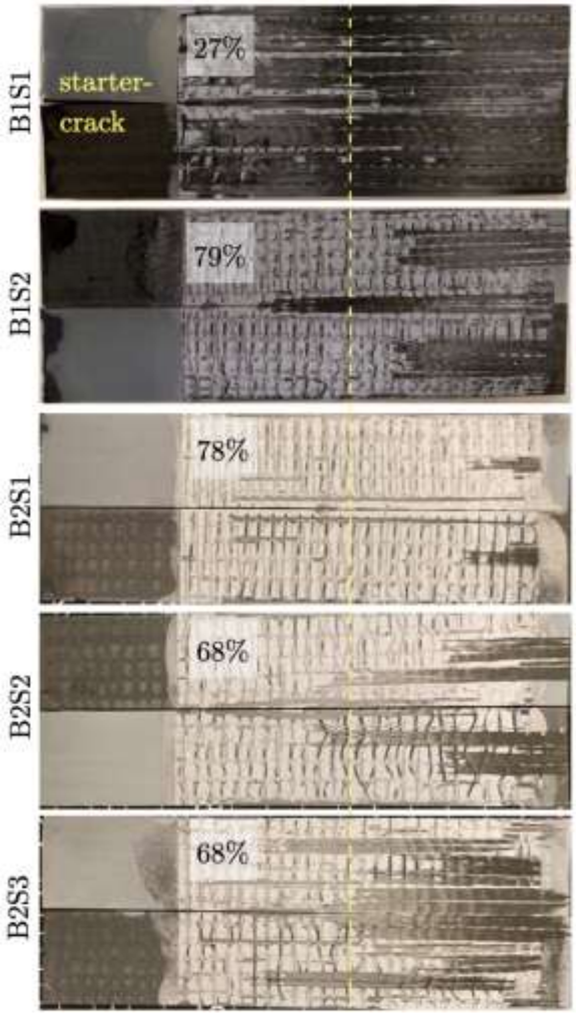

Figure 4.12: DCB sanding post-testing visual inspection of the fractured surfaces. Crack propagation occurring from right to left. The dashed line indicates the approximate location at which the tests were interrupted

Interlaminar/intralaminar fracture was the dominant mechanism of failure in B1S1, most likely due to the execution of the sanding process and/or potential induced defects on the mating area that triggered peeling out of the outmost composite layer. Closer visual inspection also revealed that the adhesive did not adhere well on the exposed glass fibres and polyester stitches. This point was further addressed with optical microscopy and the results will be discussed later. The overall results are summarized in Tab. 4.2, which reports the average fracture toughness and annotation of the dominant mechanism of failure.

Table 4.2: Average fracture toughness obtained in DCB tests.

Description	Sample #	G_{IC} (N/mm)	Mechanism of fracture (*dominant*)
• NCF-CFRP/epoxy joints • Adhesive: 3M 07333 • Surface treatment: sanding	B1S1	1.14±0.16	Interlaminar
	B1S2	1.27±0.10	Cohesive
	B2S1	1.95±0.17	
	B2S2	1.79±0.19	
	B2S3	1.57±0.18	

With the exception of B1S1, all tests have shown cohesive fracture and the results were consistent with rather small range of variation. However, B1S2 displayed a slightly lower toughness, most likely because of a variation of bondline thickness, e.g., fabrication defect.

The mechanics of crack propagation was also investigated with the aid of a CCD camera that recorded the deformation undergone by the DCB during mechanical testing. The resulting images allowed to shed light on the evolution of damage across the bondline, including any potential bridging effect in the crack wake. Video footages were recorded for each test, however, only B1S1 and B2S1 are presented here to highlight the differences in the observed (dominant) fracture mechanisms, i.e., mixed inter- /intralaminar versus cohesive fracture.

The results of B1S1 are discussed first and are gathered in Fig. 4.13. A few sudden load drops occurred during the tests, and an instance is highlighted within the red box shown in Fig. 13(a), and the ensuing crack jump is shown in Fig. 4.13(b). Both phenomena can be addressed to the peculiar mechanism of deformation and fracture of the joint. Because the crack propagated inside the CFRP substrate, it follows that carbon, glass and/or polyester fibers could be peeled out, thereby bridging the adherents during opening and effectively providing closing bridging tractions. Post-failure inspection of the fractured surfaces indicated that most bridging is likely associated with the peeling of polyester and glass fibers that are embedded within the non-crimp fabric textile; notice that transversely oriented glass fibers are placed between the carbon fiber tows to provide support during handling/manufacturing. The described mechanism is illustrated through the snapshots of the deformed DCB recorded during the test and reported in Fig. 4.13(c). The snapshots (1-4) are taken at the positions highlighted in Figs. 4.13(a) and (b) and show polyester and glass fibers that are either bridging the crack (horizontal arrow) or are already broken in the crack wake (vertical arrows).

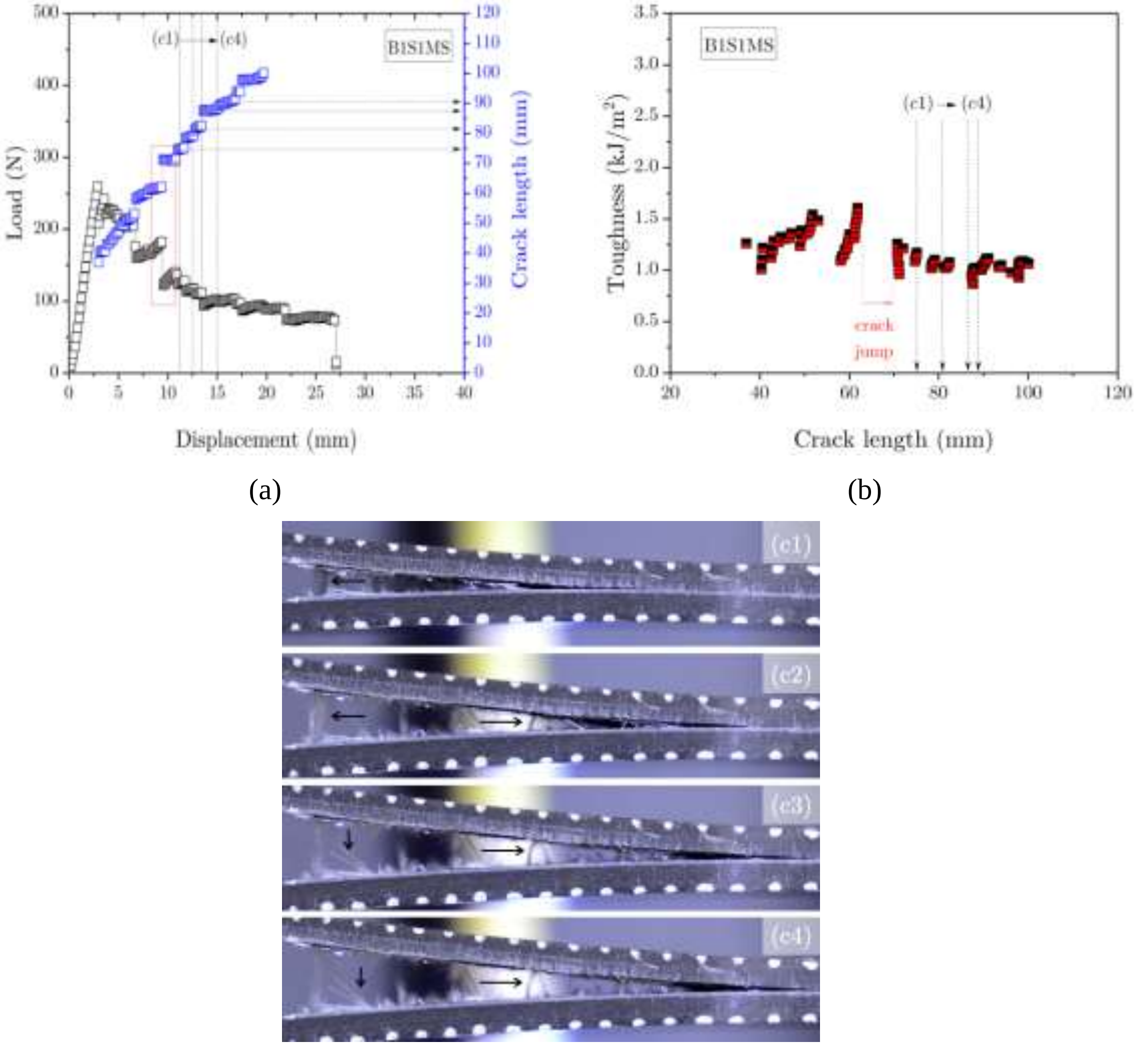

(a)

(b)

(c)

Figure 4.13: Results of DCB test on sample B1S1. (a) Load versus displacement and crack-length versus displacement curves. (b) R-curve. (c) Snapshots of the deformed configuration extracted from the video footage recorded during mechanical testing.

A similar analysis was carried out for the DCB joint B2S1, which displayed cohesive fracture. The corresponding data is gathered in Fig. 4.14.

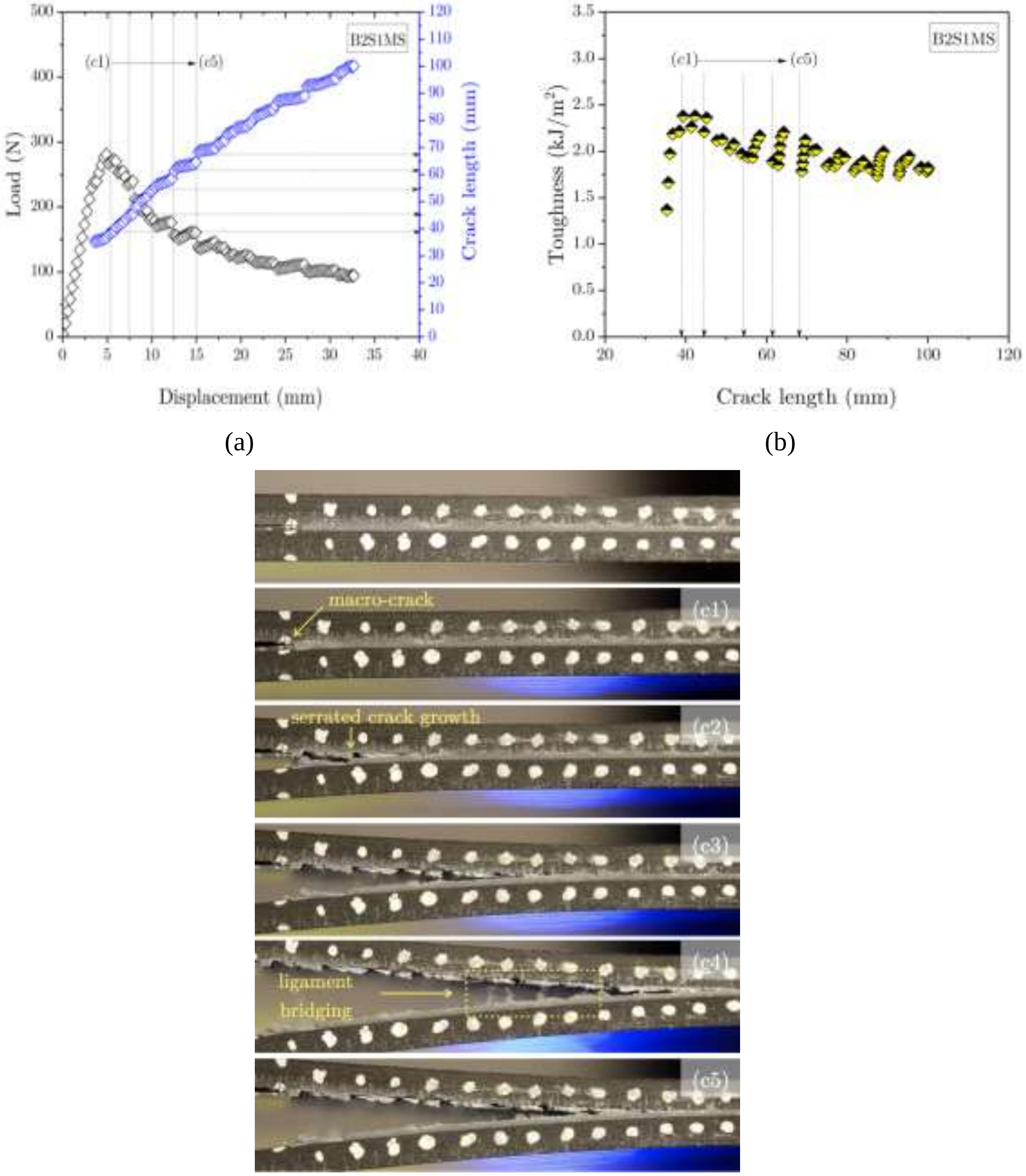

(a)

(b)

(c)

Figure 4.14: Results of DCB test on sample B2S1. (a) Load versus displacement and crack-length versus displacement curves. (b) R-curve. (c) Snapshots of the deformed configuration extracted from the video footage recorded during mechanical testing.

Also, in this case, the softening region and crack propagation are relatively smooth. However, the occurrence of small load fluctuations was also observed in this case. Snapshots of the deformation and fracture process are used again to shed light on the mechanisms of failure and are appended in Fig. 4.14(c). Notice that the images (c1-c5) are taken at the points highlighted in Fig. 4.14(a). The snapshots suggest the occurrence of cohesive fracture (that was corroborated by the visual inspection). In particular, crack growth appears to occur according to a serrated pattern, as highlighted in snapshot (2) of Fig. 4.14(c). The peculiar crack path suggests that the crack veers from the upper to the lower substrate promoted by the weak adhesion of the adhesive on top of the exposed glass fibers. In the process, a few small and isolated adhesive ligaments are formed. These last undergo deformation and failure in the crack wake as the front advances through the bondline – see the example highlighted with the rectangular dashed region within snapshot (c4) in Fig. 14(c).

A more refined assessment of the fracture surfaces was carried out using an optical microscope and the ensuing images are reported in Figure 4.15. As stated previously, failure of most specimens was dominated by cohesive fracture, except B1S1MS. It is possible to observe that glass fibers, polyester stitches and carbon fibers were all exposed. Besides, the images confirmed the occurrence of weak adhesion at epoxy/glass and epoxy/polyester interfaces, as these are basically exposed with no significant trace of epoxy (although one cannot rule out completely the presence of epoxy based on visual inspection). Also, the imprint of the glass fibers from the mating substrate are visible (see for instance B2S1MS). A few small spots of CFRP damage are observed in all specimens, which involves peeling out of the CFRP outmost surface layers (mixture of interlaminar and intralaminar fracture).

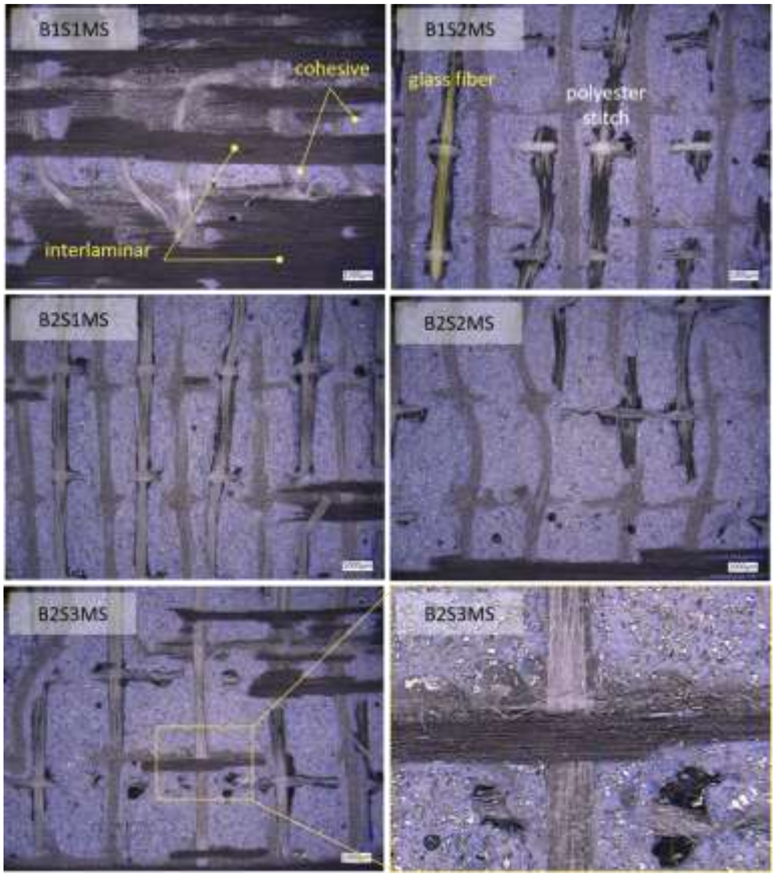

Figure 4.15: Microscopy images of DCB fracture surfaces with sanding surface treatment and 07333 adhesive (crack propagation from left to right).

4.2.1.2 Exploratory study about the effect of a UV-laser (355 nm) irradiation

Load-displacement and *R*-curve response of DCB specimens with UV laser treatment LS1 and LS2 are presented in Fig. 4.16. Note that LS1 is the process carried out at 30 kHz pulse frequency, while both were carried out at 125 mm/s lasing speed. Beside the variation of the initial slope of the load-displacement curves, which was due to the variance of the pre-crack length was from 37.5 mm to 42.2 mm, the results are fairly consistent. However, the selected UV laser ablation could not match the results of the sanding process. Indeed, cohesive fracture was not achieved in any test. The results indicate a brittle failure of the joints, which is corroborated by the low fracture toughness and the flat R-curves, that support the absences of any sort of toughening mechanisms.

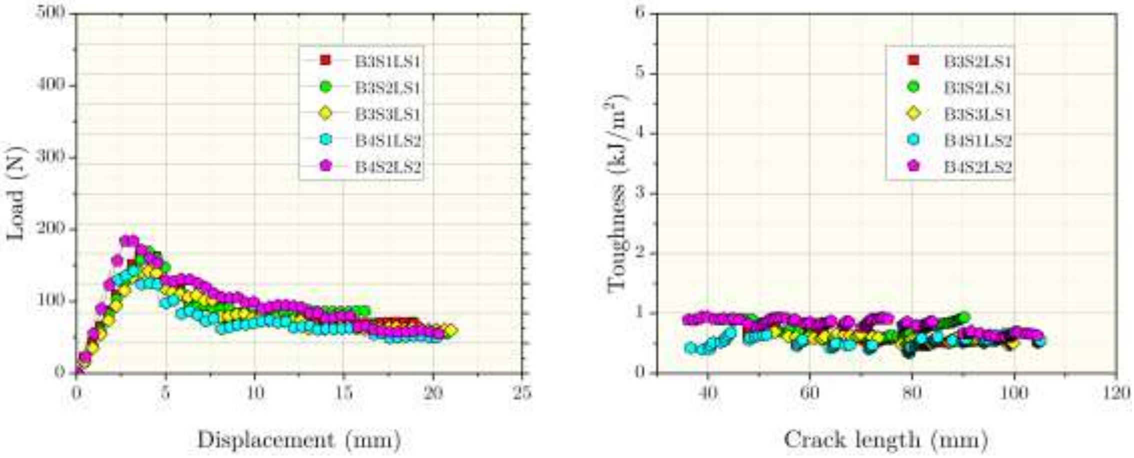

(a) (b)

Figure 4.16: (a) Load vs. displacement and (b) R-curve response for DCB specimens comprising CFRP adherends with UV laser surface treatment (LS1: 40 kHz; LS2: 30 kHz).

In short, the two laser treatments led to the same results, and no significant difference was observed when changing the pulse frequency, although the surface texture appears to be different – with exposed fibers being present at 30 kHz pulse frequency. Comparing with the data reported earlier, it is clear to see that the peak load recorded in DCB tests with sanding surface treatment was much higher (1.9 times) than the peak load of the laser treated specimens. After testing, visual observations of the fractured surface were carried out and representative images are reported in Fig. 4.17. Visual observations confirm the brittle nature of the joint fracture, as an apparent interfacial fracture occurred in all samples. Besides, it is speculated that the laser process LS1 induced damage at the glass/epoxy interface, as loose glass fibers could be observed upon inspection of the fracture surfaces.

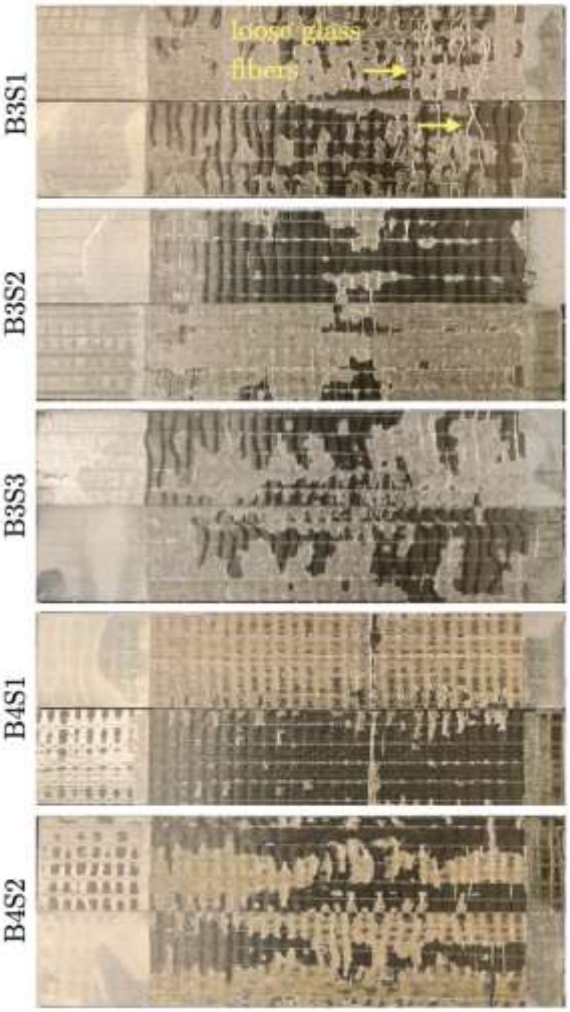

Figure 4.17: DCB UV laser post-testing visual inspection of the fractured surfaces. Crack propagation occurring from left to right.

The overall results are summarized in Tab. 4.3, including the average propagation fracture toughness and annotation of the dominant failure mechanism. All tests have shown interfacial fracture, and the results were fairly consistent. The fracture toughness after the developed UV laser treatment is significantly lower than that obtained following sanding.

Table 4.3: Fracture toughness of DCB samples with UV laser treatment and 3M 07333 adhesive.

Description	Sample #	G_{IC} (N/mm)	Mechanism of fracture (*dominant*)
• NCF-CFRP/epoxy joints • Adhesive: 3M 07333 • Surface treatment: LS1, LS2 (UV laser ablation)	B3S1LS1	0.60±0.07	Interfacial
	B3S2LS1	0.70±0.12	
	B3S3LS1	0.58±0.05	
	B4S1LS2	0.45±0.06	
	B4S2LS2	0.69±0.09	

The video footage belonging to B3S2LS1 was used to provide a general description of the failure process that is reasonably representative of all samples. The results are gathered in Fig. 4.18.

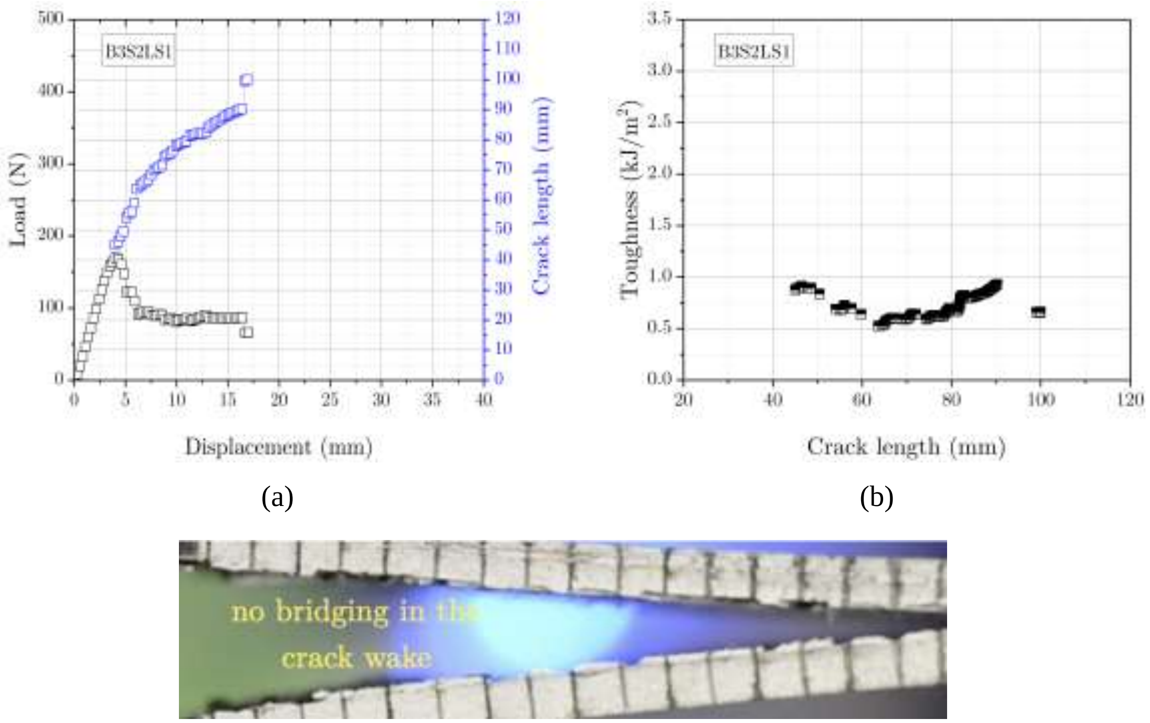

(a) (b)

(c)

Figure 4.18: Results of DCB test on sample B3S2. (a) Load versus displacement and crack-length versus displacement curves. (b) R-curve. (c) Snapshots of the deformed configuration extracted from the video footage recorded during mechanical testing.

The most remarkable difference is the much lower peak load and maximum displacement achieved during testing. The debonding process over the probed area (100% of the total bondline) took place with a maximum opening of 16 mm; to set the stage for comparison, please note that for a sanded sample a similar crack advance would require double opening displacement. Besides, the R-curve displayed a variation in the obtained toughness since it initially decreased and then increased again. A potential explanation may be laid down on the basis of the observed crack path. Indeed, the crack front occasionally veered from the upper to the lower interface. In the process, damage and fracture of the de-bonded adhesive layer is involved and increases the fracture energy. The video footage of the tests did not display any significant additional dissipation mechanisms besides the front veering described above. For instance, Fig. 4.18(c) shows that there are no fibers or adhesive ligaments bridging the crack face. This observation holds consistently for the whole duration of each test.

Microscope images are reported in Fig. 4.19 and confirm the occurrence of weak adhesion at CFRP/epoxy interfaces.

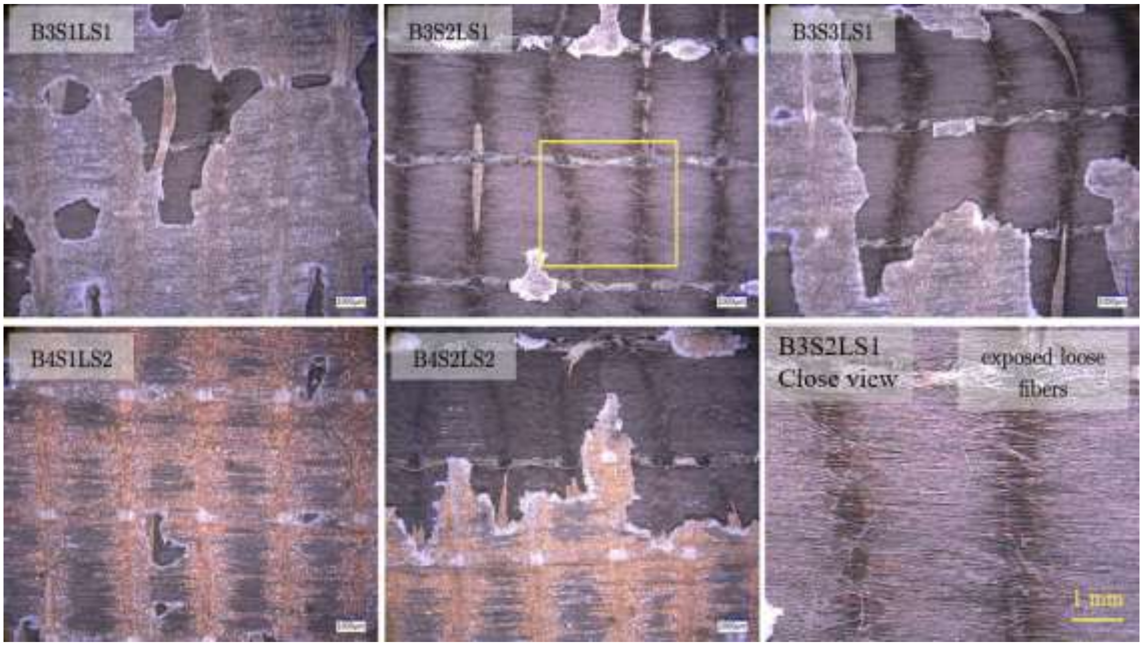

Figure 4.19: Microscopy images of DCB fracture surfaces with UV laser treatment and 3M 07333 epoxy adhesive (crack propagation from left to right).

The images also confirm the presence of loose fibers for the LS1 processing. Such loose fibers were not observed with LS2, which is consistent with previous profilometry and microscopy analyses. More work should be done to identify a proper combination of processing parameters that can promote a stronger adhesion. However, the laser platform employed in the present work can only process small areas, and, therefore, sample preparation is very time-consuming. For this reason, the laser treatment was not pursued further, and additional investigations should be the subject of future works.

4.2.2 ENF tests and determination of Mode II fracture toughness

The ENF tests were carried out to assess the 3M 07333 structural adhesive against crack propagation in Mode II, i.e., shear. Besides, the influence of different loading rates was explored. As such, mechanical tests were executed at 0.1 mm/s (DR01), 5 mm/s (DR5), and 15 mm/s (DR15). Please note that such analysis for Mode I tests was reported elsewhere [89]. Details about the test setup were provided in Section 3.6.2. The fracture behavior was analyzed on the basis of the obtained force-displacement responses, the fracture toughness, in-situ imaging of the fracture process, and fractographic analyses.

4.2.2.1 Displacement controlled tests at 0.1 mm/s

The load-displacement curves and R-curve of the ENF with sanded CFRP substrates are reported in Fig. 4.20.

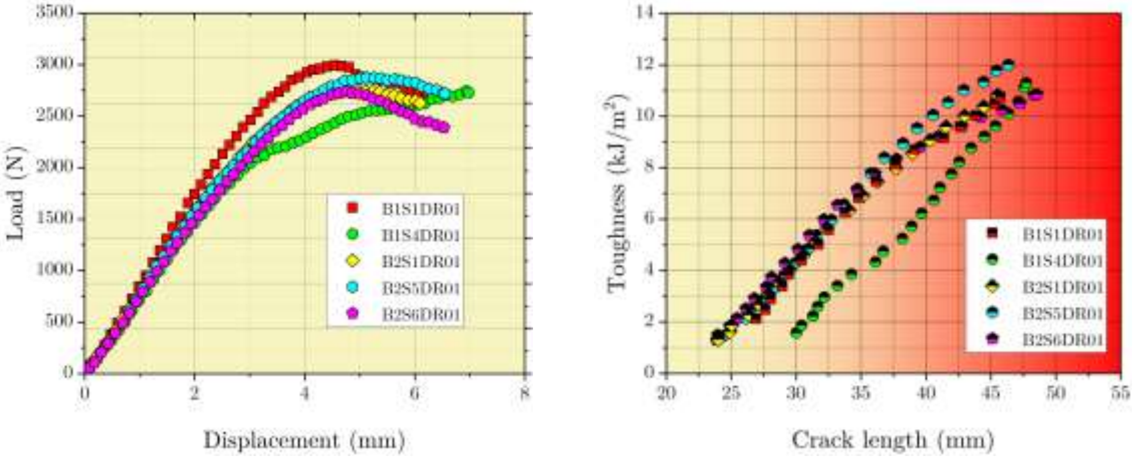

(a)

(b)

Figure 4.20: (a) Load vs. displacement and (b) R-curve response for ENF specimens comprising CFRP adherends with sanding surface treatment.

The results are generally fairly consistent, whereby the initial linear response is quite similar in all tests, while some deviations are observed after the formation of a macroscopic crack. The most significant deviation was observed during testing of B1S4DR01, which was addressed to intralaminar damage of the CFRP substrate (see Fig. 4.21). For the remaining four specimens, the average peak load is 2827±112 N, which is quite consistent considering that the samples belong to distinct fabrication batches (B1 and B2). Likewise, the corresponding R-curves reported in Fig. 4.20(b) were consistent and comparable. However, none of the tests achieved a steady state crack growth as the R-curve was essentially always raising with the crack length. Therefore, while the maximum toughness achieved in mode II tests is quite large and much larger than the Mode I fracture toughness, in the remainder only the initiation fracture toughness will be provided. Each test was interrupted when the crack front approached the location of the loading pin. Further loading upon approaching this location has resulted in bulk damage to the upper CFRP substrate.

After mechanical tests, the samples were carefully separated by using a wedge, and a visual inspection of the fracture surfaces was executed. A view of fracture surfaces is provided in Fig. 4.21. The following regions are defined: (1): starter-crack (anti-sticking insert); (2): pre-crack; (3): Mode II crack growth region; (4): post-test wedge splitting region. Most specimens were dominated by a cohesive fracture in the zone (3), except ENF B1S4, which has shown intralaminar fracture nearby the specimen side, probably because of interfacial stress concentration or damage induced during sample cutting (or both). The visual inspection also revealed differences in the fracture surfaces' appearance with respect to Mode I tests that will be further discussed later. The overall results are summarized in Tab. 4.4, which reports the initiation fracture toughness as well as the associated dominant mechanisms of failure. The average toughness across the different specimens was equal to 1.28±0.05 N/mm (the average does not include B1S4).

Table 4.4: Fracture toughness determined in ENF tests carried out at 0.1 mm/s displacement rate.

Description	Sample #	$G_{II,i}$ (N/mm)	Mechanism of fracture (*dominant*)
• NCF-CFRP/epoxy joints • Adhesive: 3M 07333	B1S1DR01	1.21	Cohesive
	B1S4DR01	1.57	Mixed cohesive/interlaminar

• Surface treatment: sanding • Displacement rate: 0.1 mm/s	B2S1DR01	1.27	Cohesive
	B2S5DR01	1.32	Cohesive
	B2S6DR01	1.32	Cohesive

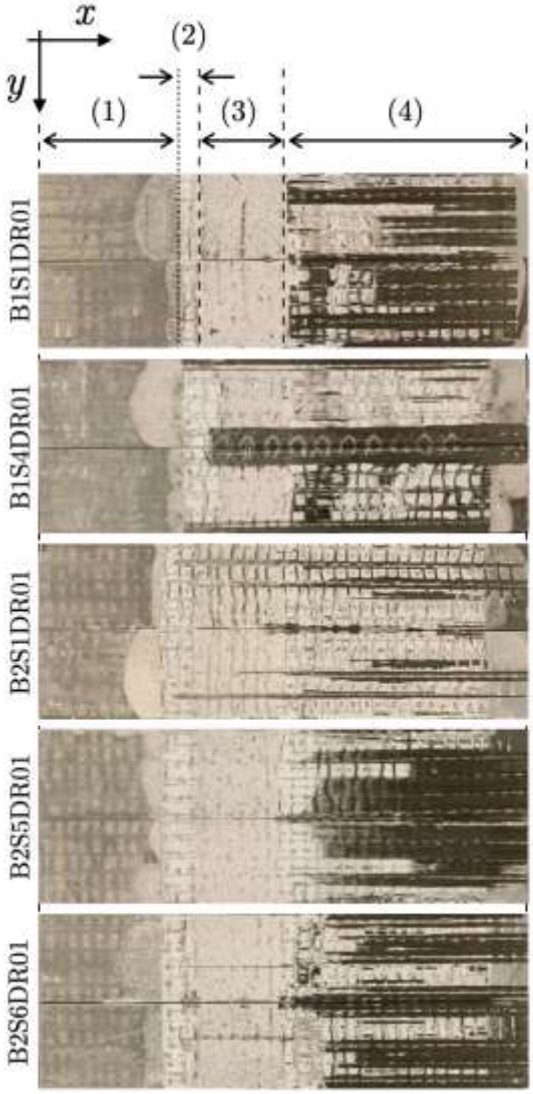

Figure 4.21: Post-failure analysis of the fractured surfaces. Crack propagation from left to right.

To better clarify the mechanics of crack growth and the reasons why a steady state was not achieved, the fracture process was assessed with the support of video footage recorded using a CCD camera. The analysis makes reference to B2S5DR01, and the corresponding data is reported in Fig.

4.22. The figure includes the load-displacement and cracks length-displacement curves, the R-curve, and the snapshots of the data points highlighted in these plots. Regarding Fig. 4.22(c), each letter corresponds to the points in Fig. 4.22(a) and (b).

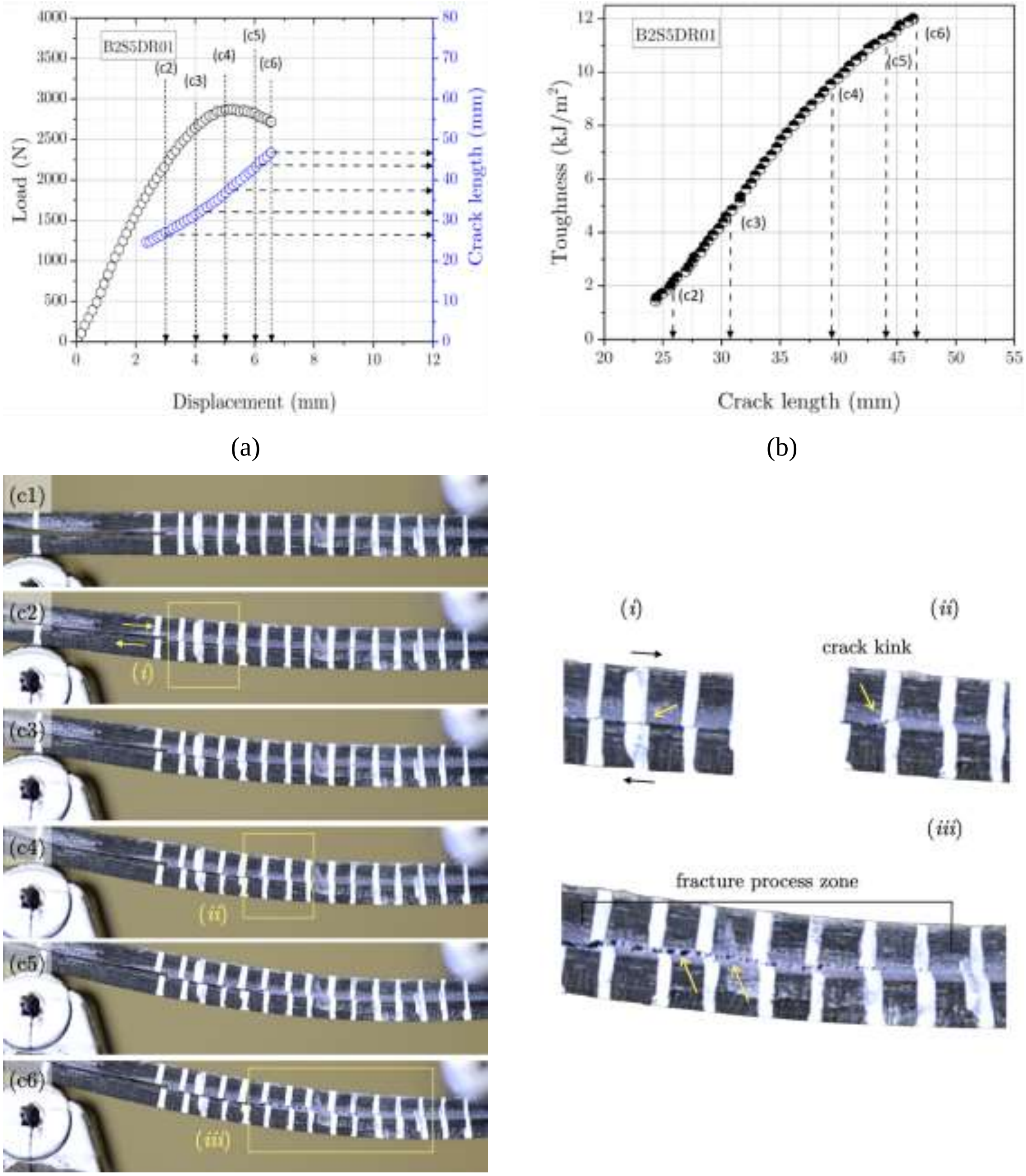

(a) (b)

(c) (d)

Figure 4.22: ENF B2S5DR01. (a) Load versus displacement and crack-length versus displacement curves. (b) R-curve. (c) Snapshots of the deformed configuration. (d) Details of damage development extracted from the video footage.

The combined analysis of these figures demonstrates macroscopic fracture taking place at point (c2) in the load-displacement response whose corresponding deformed configuration is shown in Fig. 4.22(c). The location of the crack front is further highlighted in Fig. 4.22(d), which provides an enlarged view of the area (*i*). The yellow arrow points to the front location, and the misalignment of the vertical white lines drawn on top and bottom substrates highlights the shear deformation taking place across the bondline. At this stage, the crack is apparently located near the lower interface. Upon further loading, the load reaches point (c4), and the crack kinks within the adhesive layer, as shown in the inset (*ii*) in Fig. 4.22(d). The deformation of the adhesive layer is accompanied by substantial whitening that involves an area of a finite length ahead of the crack front. The whitening could be discerned easily from the video footage of the tests, but, unfortunately, it is less noticeable from snapshots such as those provided in Fig. 4.22(d). Adhesive whitening is due to the plastic deformation of the adhesive under shear, which in general is quite large under Mode II loading [103] . Besides, it should be recalled that the 3M 07333 adhesive displays a very ductile behavior because of the synthetic rubber included in its formulation - see Chapter 3.1. With further loading, the crack front moves toward the midpoint of the joint.

The analysis of the video footage indicated the formation of a characteristic cracking pattern, whereas small cracks or cavities initially grew slanted with respect to the load direction. The orientation is approximately at 45°, which is the direction of the maximum resolved tensile stress in the bondline, which implies the initial microcracks have likely grown in Mode I [104]. The occurrence of such a cracking pattern generates a large process zone, which is better illustrated in Fig. 4.22(d). The process zone continued to grow till the crack was close to the loading pin. Therefore, a fully developed process zone and steady-state crack growth were not observed during the test. The approximate size of the process zone when the crack front approached the loading pin was estimated from the analysis of binary images of the bondline such as that given in Fig. 4.23. The binary image shows that the crack path extended from the region near the lower interface and diverted within the adhesive layer, while leaving in its wake a large number of small cavities spread over a length of about 15 mm.

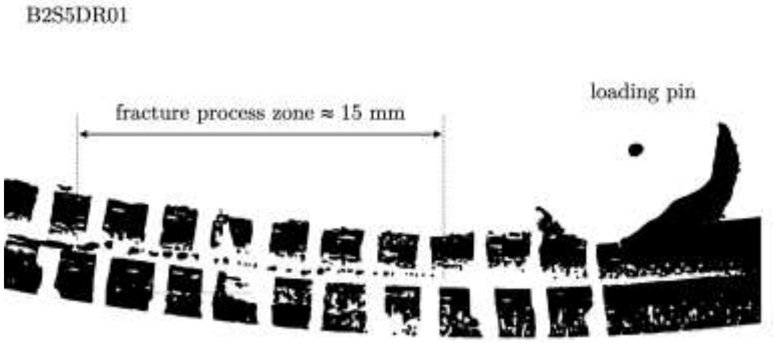

Figure 4.23: Binary image of the deformed ENF illustrating the process zone size.

The development of damage in the crack wake was mostly similar for all tests. For instance, as shown in Fig. 4.24, a very similar cracking pattern was observed for B1S1. However, following crack kinking, in other tests the damage was mostly located nearby either the top or the bottom interface (or both). Although the side view may suggest an interfacial fracture, the analysis of fracture surfaces reported in Fig. 4.21 demonstrates the occurrence of a cohesive fracture.

Figure 4.24: Side view of ENF samples with 0.1 mm/s displacement rate.

In order to explore the characteristics of the fracture surfaces at a finer detail, optical microscopy analyses were carried out and typical results are reported in Fig. 4.25 The analysis of crack path at the top substrate demonstrate that the crack propagated in the region nearby the interface, indeed uncovered glass fibers belonging to the NCF-CFRP substrate are clearly discernible.

In any case, the images show a ductile fracture with parabolic microcracks resembling fish scales (highlighted by the yellow dashed lines) which are attributed to the intense plastic straining associated to the ductile nature of the structural adhesive employed herein.

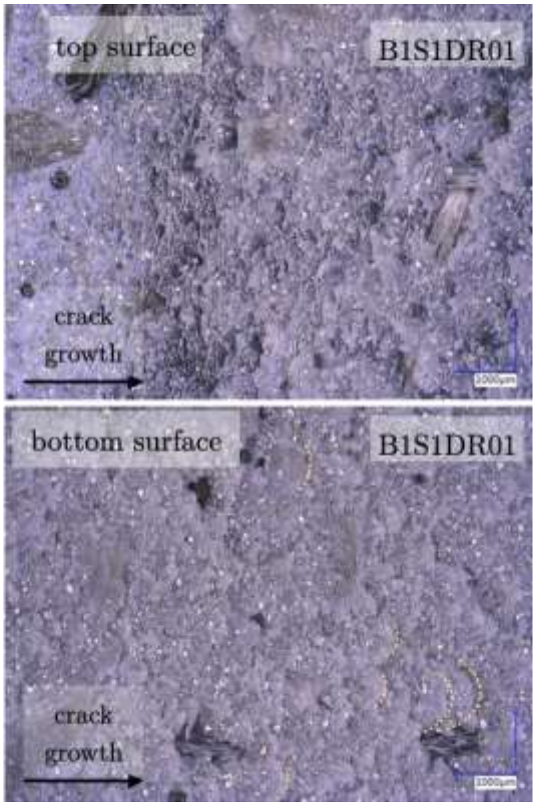

Figure 4.25: Microscopy images for ENF specimens at 0.1 mm/s (crack growth from left to right).

4.2.2.2 Displacement controlled tests at 5 mm/s

The load-displacement responses and R-curves of the ENF specimens tested at 5 mm/s are reported in Fig. 4.26. The nuance of the curves is very similar to previous tests. The R-curves displayed a raising behavior which again indicates that a steady state crack growth was not achieved, and a constant toughness could not be extracted from the tests. As done before, to prevent the development of substrate damage, all tests were interrupted before the crack front reached the region nearby the loading pin.

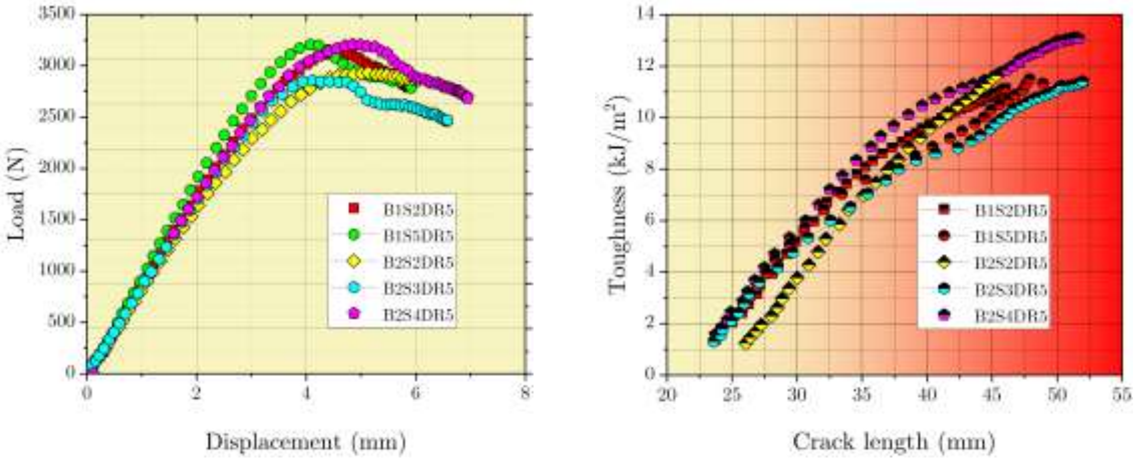

(a) (b)

Figure 4.26: (a) Load vs. displacement and (b) R-curve response for ENF specimens comprising CFRP adherends with sanding surface treatment.

The fracture surfaces are shown in Fig. 4.27 and a visual inspection indicated that cohesive fracture was the main mechanism of failure in all tests. Once again, the video footages revealed the formation of an extended process zone and no significant differences were observed with respect to loading at a slower cross-head displacement rate. The overall results are summarized in Tab. 4.5, and similarly to the ENF specimens tested at 0.1 mm/s, only the initiation fracture toughness is reported.

Table 4.5: Fracture toughness determined in ENF tests carried out at 5.0 mm/s displacement rate.

Description	Sample #	$G_{II,i}$ (N/mm)	Mechanism of fracture (*dominant*)
• NCF-CFRP/epoxy joints • Adhesive: 3M 07333 • Surface treatment: sanding • Displacement rate: 5 mm/s	B1S2DR5	2.03	Cohesive near the interface
	B1S5DR5	2.15	
	B2S2DR5	1.24	
	B2S3DR5	1.30	
	B2S4DR5	1.38	

The average toughness across the various tests was equal to 1.62±0.43 N/mm, i.e., the toughness is somewhat higher than that recorded at DR01.

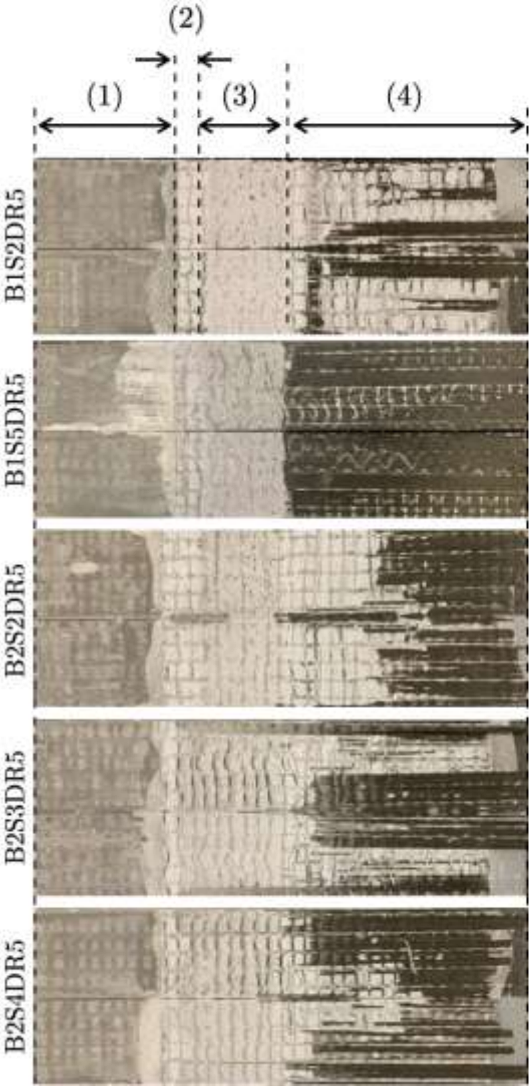

Figure 4.27: Post-test images of ENF 15 mm/s specimens.

The mechanisms of deformation and fracture were essentially similar to that observed at the lower displacement rate, although the crack path was closer to the upper interface. This is shown in Fig. 4.28 that highlights the progress of damage in a few samples belonging to different fabrication batches.

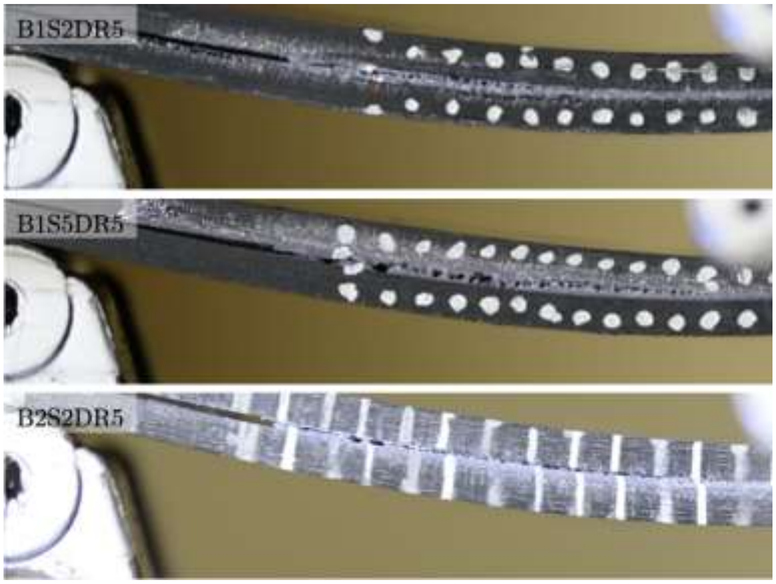

Figure 4.28: Typical crack path recorded during ENF tests executed at 5 mm/s.

This point is confirmed through optical imaging of the fractured surfaces that are provided in Fig. 4.29. Beside the large straining undergone by the adhesive, that resembles the mechanism observed in previous tests, it is inferred that the crack path was much closer to the upper interface, as testified by the uncovering of glass fibers and polyester stitches.

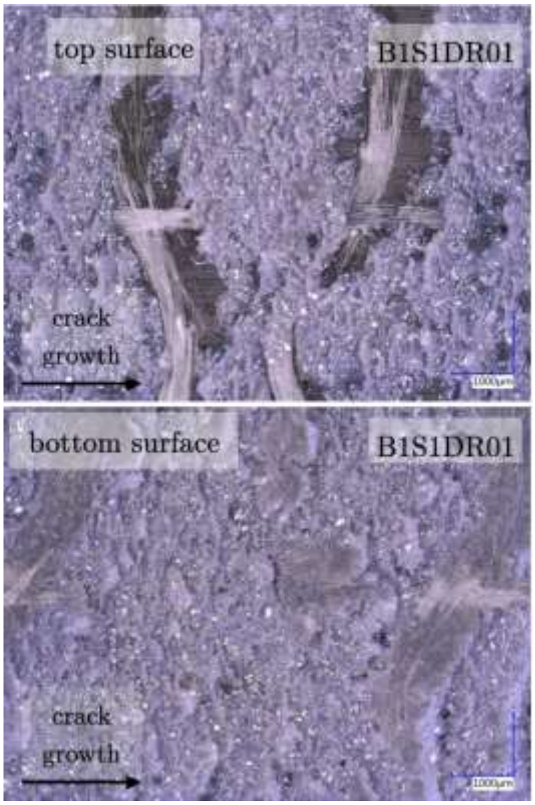

Figure 4.29: Microscopy images of typical fractured surfaces in ENF tests carried out at 5 mm/s (crack propagation from left to right).

4.2.2.3 Displacement controlled tests at 15 mm/s

The results of ENF tests were carried out at 15 mm/s are provided in Fig. 4.30. The variation of the initial slope for B1S3 and B1S6 was caused by different pre-crack length. These samples suffered a catastrophic fracture, i.e., bulk damage initiated within the upper adherent and propagated catastrophically through the joint. It is worth noting that prior to catastrophic failure, damage and fracture of the adhesive layer was observed. For the other three specimens, the pre-crack length was slightly increased. In addition, the tests were interrupted at a cross-head displacement of about 6.0 mm to prevent a catastrophic fracture. Also, the video footage was used to track potential damage within the bulk CFRP and eventually remove the data affected by such damage in the determination of fracture toughness. The so obtained R-curves indicate that also in this case a steady state crack growth was not achieved.

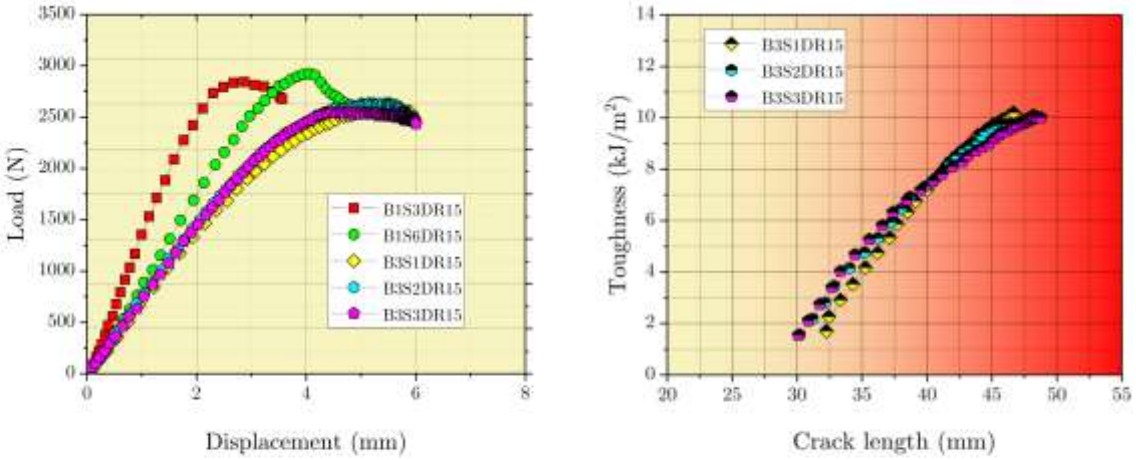

(a) (b)

Figure 4.30: (a) Load vs. displacement and (b) R-curve response for ENF specimens comprising CFRP adherends with sanding surface treatment.

The fracture surfaces were similar to previous tests carried out at 5 mm/s; indeed, the crack path was closer to the upper interface. A global view of the fracture samples is provided in Fig. 4.31. The initiation toughness for each test is provided in Tab. 4.6. The average toughness of DR15 samples is 1.60±0.08 N/mm.

Table 4.6: Initial toughness of ENF specimens at DR15.

Description	Sample #	$G_{IIini.}$ (N/mm)	Mechanism of fracture (dominant)
• NCF-CFRP/epoxy joints • Adhesive: 3M 07333 • Surface treatment: sanding • Displacement rate: 15 mm/s	B3S1DR15	1.70	Cohesive
	B3S1DR15	1.57	Cohesive
	B3S1DR15	1.54	Cohesive

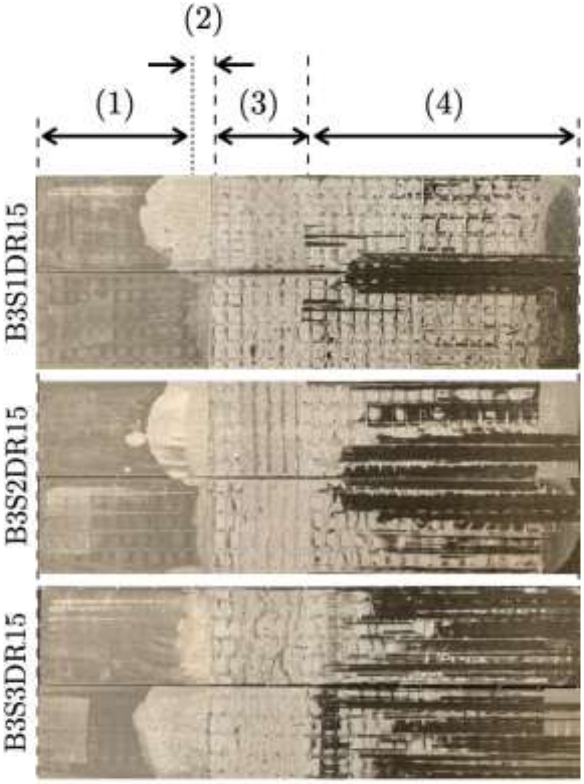

Figure 4.31: ENF 15 mm/s post-testing visual inspection of the fracture surfaces. Crack propagation occurring from right to left.

Given the high speed of the tests, it was difficult to make direct correlation between load-displacement data and the images that could be extracted from the video footages. Nevertheless, images of the deformation and fracture process were extracted to assess the mechanism of failure and are reported in Fig. 4.32. The snapshots illustrate a cracking pattern similar to that observed earlier at 5 mm/s. Further assessment of the fracture process was carried out with the aid of an optical microscope. Typical results are shown in Fig. 4.33 and demonstrate that the crack path was again very close to the upper interface with significant exposure of glass fibers and polyester stitches. These results suggest that increasing the displacement rate shifted the crack path closer to the interface. It is likely that the rate dependency of the adhesive material has played a role in this respect. However, no oscillations were observed on the load-displacement curves, which may imply the absence of dynamic (inertia) effects during crack propagation.

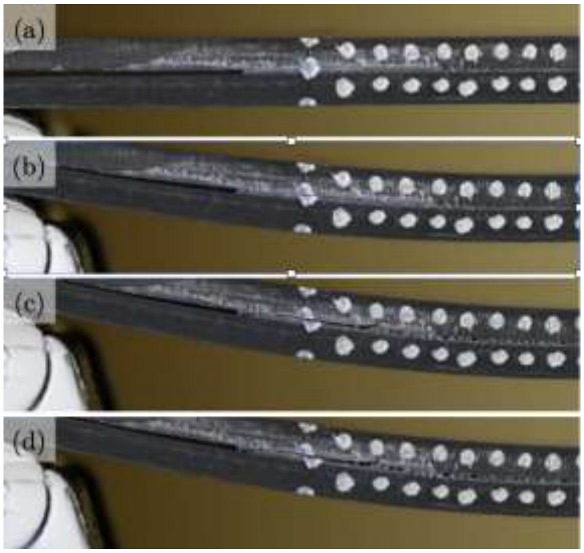

Figure 4.32: Snapshots of the deformation process of the ENF specimens at 15 mm/s.

.

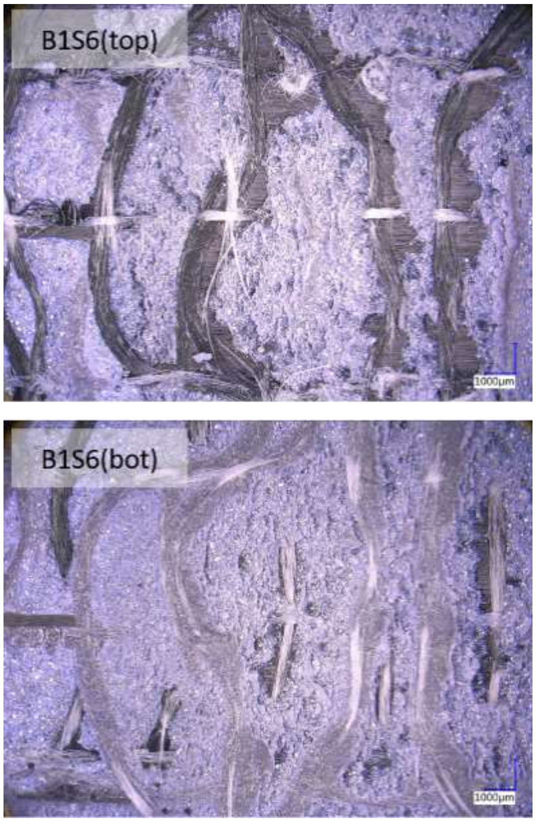

Figure 4.33: Microscopy images for ENF specimens at 15 mm/s (crack propagation from left to right).

4.2.3 X-Ray CT assessment of CFRP bulk damage due to bending

As discussed earlier, bulk damage occurred within the NCF-CFRP substrates during mechanical tests of ENF samples. The damage originated in the loading pin-sample contact area and, at the highest displacement rate, propagated through the bondline to the lower adherent resulting in a catastrophic fracture. Besides, it was noted that the initiation of bulk CFRP damage was always concurrent with the crack front being in close proximity to the loading pin (at the midpoint of the sample). Notice that the data extracted for the determination of R-curves was always cut-off much earlier and before the front approached the above-stated location. In addition, to support this approach, a second CCD camera was placed next to the sample and targeted the loading pin area directly to monitor the occurrence of damage, in time and space, and make sure that the data used for the determination of toughness was free of any influence associated with bulk damage. This was ensured by interrupting each test when the cross-head displacement was about 6 mm. It is speculated that damage originated from the excessive bending deformation of the beams, whose effect was exacerbated by the contact stress induced by the pin. The damage was analyzed using X-Ray computed tomography (X-Ray CT) executed with the ZEISS Xradia Versa 520 available at the University of Waterloo within the MSAM laboratory. A description of the system was provided in Section 3.6.2.

The sample was extracted from an interrupted ENF test at the instant in which the crack front was located nearby the pin and bulk damage was quite apparent. The top adherent was sliced using a water jet and the scanned volume was about 3 x 2.8 x 9 mm^3. Each slice, i.e., each CT image, was separated apart of about 9 μm. Four representative images are taken herein to illustrate the main points offered by the CT scans and are reported in Fig. 4.34.

The CT image taken at z= 54μm highlights some basic information that can be extracted from the analysis, including clear visualization of the stitches, the adhesive layer and the contact-induced damage zone. The direction of crack growth is also highlighted. The image corresponding to z= 333μm aims to illustrate an instance of bondline porosity, that was otherwise difficult to appreciate from visual inspection. However, the analysis of multiple images did not reveal any concerning high occurrence of porosity, and one can conclude that bondline porosity was not a major fabrication issue. The image corresponding to z= 468μm has twofold usefulness. The region enclosed in the box shows an area involving intralaminar fracture, as there is a stitch that appears on the other side of the adhesive layer. It is not easy to distinguish the clear boundary between the adhesive layer and the CFRP, however, the presence of the stitch clearly indicates that a residual of CFRP certainly remained on the adhesive, which demonstrates the interlaminar nature of the fracture process – at least locally. In addition, the multiple white spots that are visible in all images reported herein, are likely explained as originated by the multiple fillers comprised in the adhesive formulation described in Materials and Methods section. The precise composition, quantity, and functions are trade secrets and are not entirely disclosed by the manufacturer.

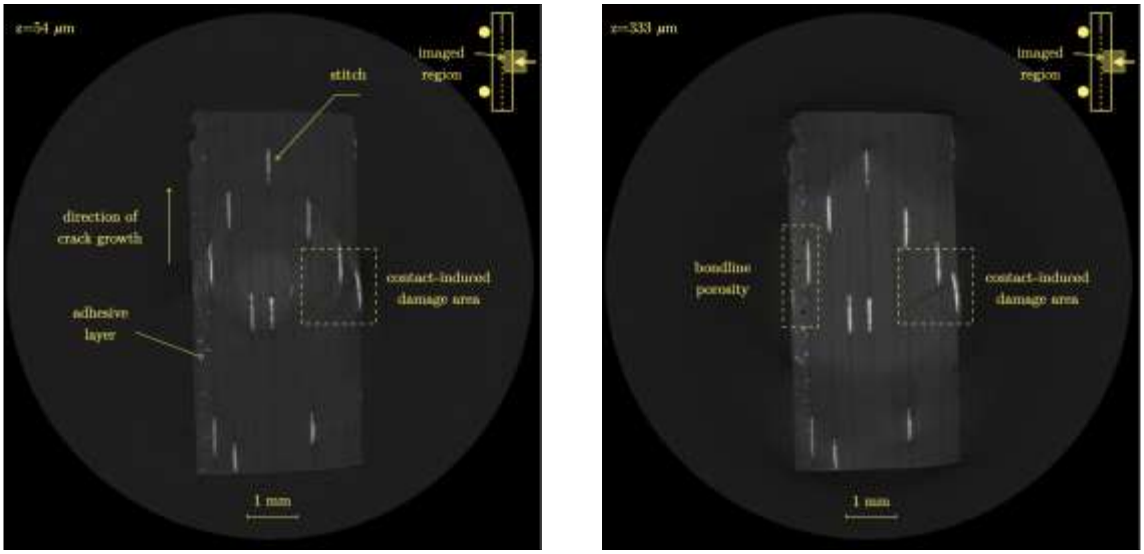

(a) (b)

Figure 4.34: X-Ray computed tomography images of damage belonging to a NCF-CFRP/epoxy joint belonging to an interrupted ENF test (ENF B1S1DR01). The images were extracted at different depths, which are given as follows: (a) 54 μm; (b) 333 μm; (c) 468 μm; (d) 5211 μm.

Finally, the last image taken at z=5211 μm highlights an additional instance of the interlaminar crack path within the joint that may be facilitated by sanding-induced damage on top of the CFRP plate. Indeed, it is apparent that the crack can find its way through the stitch such that the crack path is diverted from the bondline to the substrate. It is important to emphasize that the separation/opening of the ENF sample after test interruption was accomplished manually using a wedge. Likewise, for the DCB tests, as mentioned earlier. In such conditions, it was always observed a certain degree of interlaminar fracture in the wedge-induced separation region. While it is not entirely clear why wedge opening induced such degree of interlaminar fracture, it is emphasized that this was not the main mechanism of failure in the portion of the sample where the crack was driven by the applied load and displacement - with the sole exception of B1S1, as noted earlier.

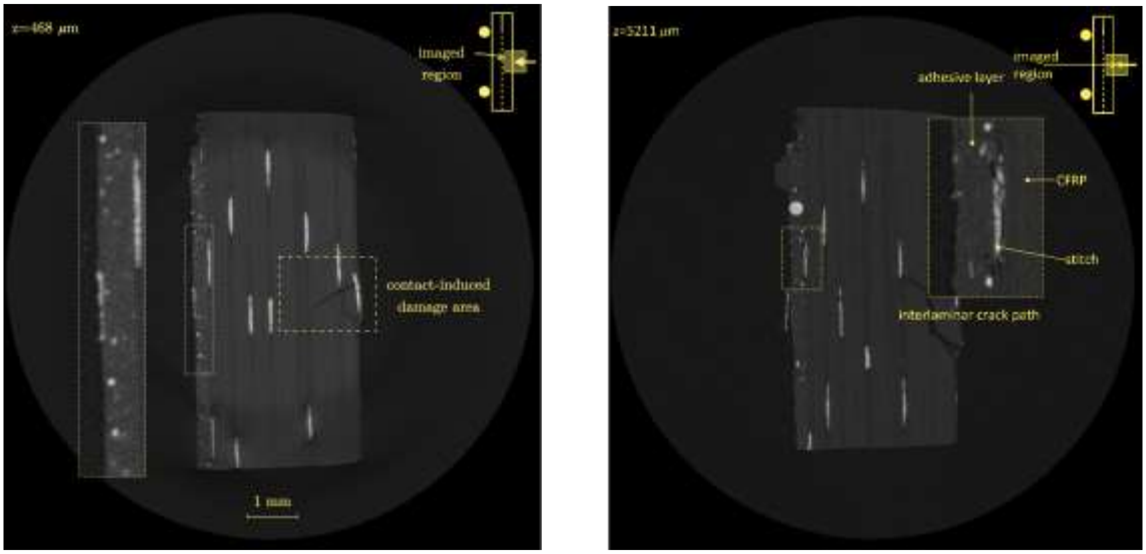

(c) (d)

Figure 4.35: (cont.)

4.3 Mechanical tests of CFRP joints bonded with 3M Scotch-Weld^{TM} DP190 epoxy adhesive

4.3.1 Sample fabrication: first iteration

In the first fabrication batch, because of the unexpected low viscosity of epoxy resin, the bondline thickness of the DCB specimens was inconsistent across the bonded area. As a result, the load-displacement response of the samples displayed an anomalous behavior, whereas an initial large peak load was followed by a relatively steep softening response and an almost constant applied load. This is shown in Fig. 4.35(a) for three samples manufactured in the first batch. A subsequent investigation of the fracture surfaces through visual inspection, indicated that a lack of adhesive was responsible for the anomalous response. In particular, post-failure fracture surfaces are shown in Fig. 4.36(b).

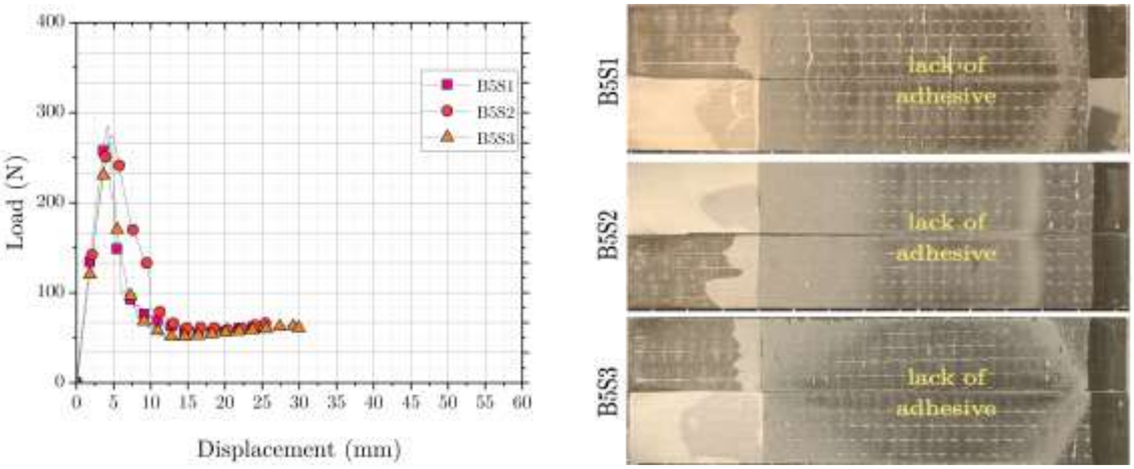

(a) (b)

Figure 4.36: (a) Load vs. displacement and (b) fractured surfaces of the DCB samples bonded with the 3M DP190 structural epoxy.

Following the analysis of the test results, a first modification to the fabrication procedure was made by reducing the applied pressure during curing. The corresponding results are shown in Fig. 4.37 and show a much regular load-displacement response, in particular, for B6S3.

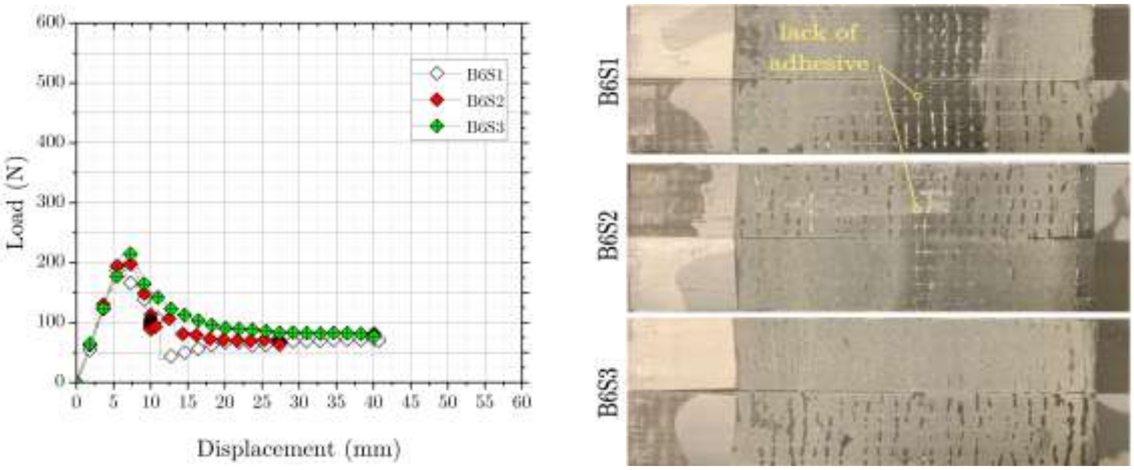

(a) (b)

Figure 4.37: (a) Load vs. displacement and (b) R-curve response for DCB batch 6 specimens comprising CFRP adherends with DP190.

Indeed, with the sole exception of the latter sample, the remaining ones displayed a load drop at an opening of about 10 mm. This is a strong indication of a defect within the bondline. Indeed, as illustrated in Fig. 4.37(b). there was again a lack of adhesive in B6S1 and B6S2.

4.3.2 Sample fabrication: second (successful) iteration

It was surmised in the follow-up investigation that the initial manual squeezing carried out to spread the excess adhesive was responsible for the problem encountered in B5 and B6. The manual squeezing was carried out by gently pressing the substrates before placing the assembly within the mold. Therefore, remedial actions were taken, and a new batch was prepared without using the extra squeezing step to verify the hypothesis. Besides, a slight increase of the bondline thickness to 0.35 mm was determined to have a beneficial effect on the results consistency, as shown in Fig. 4.38.

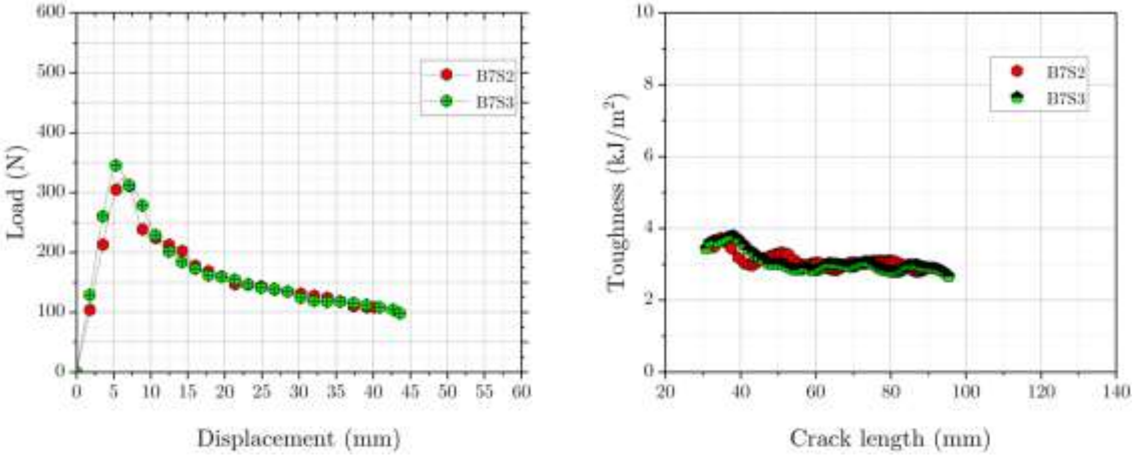

(a) (b)

Figure 4.38: (a) Load vs. displacement and (b) R-curve response for the DCB specimens bonded with the DP190 after improving the manufacturing process.

In particular, the load-displacement responses are illustrated in Fig. 4.38(a) and show an excellent consistency in both peak load and the subsequent softening response. In particular, the peak load was followed by a smooth softening. The fracture toughness was quite consistent and basically constant (flat R-curve). It is worth noting that the average toughness was also higher than that of the 3M 07333 adhesive. In particular, the results are summarized in Tab. 4.7 along with the mode of fracture. As anticipated, the toughness is relatively high and almost equal to 3.0 kJ/m^2.

Table 4.7: Fracture toughness of batch 7 DCB specimens with DP190 adhesive.

Description	Sample #	Fracture toughness (N/mm)	Mechanism of fracture
• NCF_CFRP/ epoxy joints • 3M DP190 adhesive • Surface treatment: sanding	B7S2	3.06±0.18	Cohesive
	B7S3	3.02±0.25	Cohesive with small fraction of interfacial fracture

The post-failure inspection of the fractured surfaces confirmed the occurrence of cohesive fracture and that there was no lack of epoxy across the bondline. The images of the fractured samples are provided in Fig. 4.39. The analysis of the fracture surfaces suggests a cohesive fracture, but it is also possible to note that some small spots of interfacial fracture were present. The exposure of glass fibers was more apparent compared to the 3M 07333, thus suggesting that a different interaction might have taken place with the CFRP surface. Additional investigations were made using the optical microscope and the results are discussed in what follows.

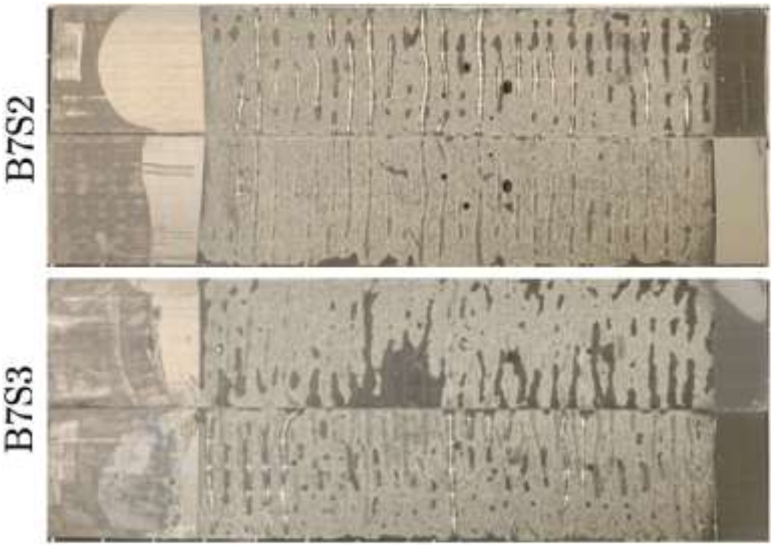

Figure 4.39: DCB DP190 adhesive post-testing visual inspection of the fracture surfaces. Crack propagation occurring from right to left.

The mechanisms of deformation and fracture of the DP190 adhesive are discussed in more detail by making reference to B7S2 sample, whose results are summarized in Fig. 4.40. In particular, Fig. 4.40(a) shows the load-displacement response and the crack length-displacement curve. While Fig. 4.40(b) illustrates the ensuing R-curve. The peak load is followed by a smooth softening response accompanied by a stable increment of the equivalent crack length. However, small load fluctuations are visible during softening, and they are reflected in the R-curve.

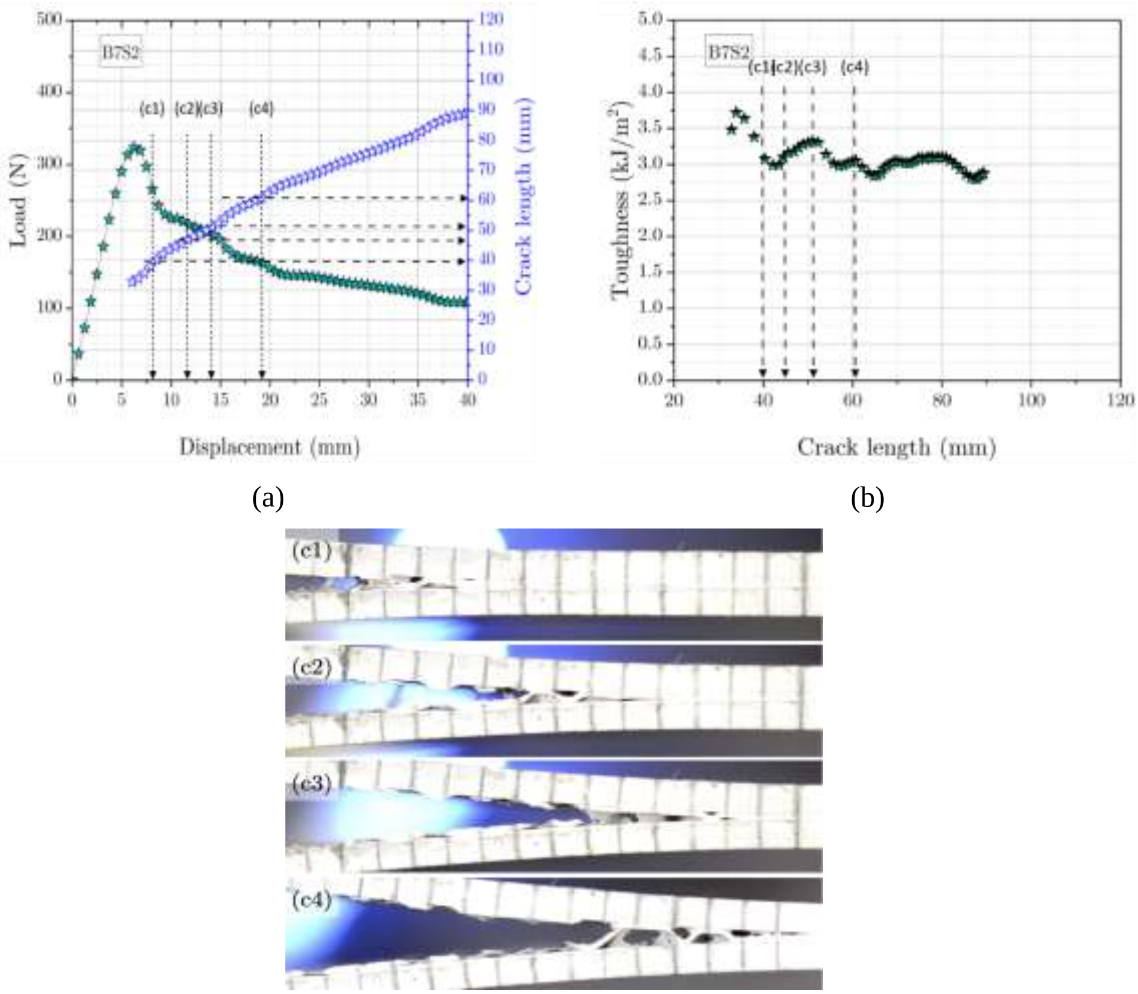

(a) (b)

(c)

Figure 4.40: Results of DCB test on sample B7S2. (a) Load versus displacement and crack-length versus displacement curves. (b) R-curve. (c) Snapshots of the deformed configuration extracted from the video footage recorded during mechanical testing.

Snapshots of the deformed sample configuration extracted from the video footage reveal the origin of these fluctuations. Indeed, the bondline damage and fracture process featured the remarkable formation of bridging adhesive ligaments in the crack wake. In particular, it seems that the cracking front veers from the upper to the lower interface and vice versa leaving an array of ligaments in the wake. The formation of these ligaments was observed across the entire bondline, as the front progressed. Deformation and failure of these ligaments surely contributed to the overall dissipation and explain the oscillations observed in the R-curves. The snapshots also indicate that the ligaments were not developed in uniform fashion across the width of the sample. For instance, the snapshot (c3) indicates that a portion of the adhesive layer bridging the crack is oriented in the transverse direction. This is a very interesting outcome that has been facilitated by the specific structure of the composite material employed in this study. The ligaments were promoted by the lack of adhesion between the epoxy and the exposed glass fibers following surface preparation. A precise control on the formation and deployment of these ligament would be possible if the alignment/positioning between the glass fibers of the top and bottom substrate could be controlled. The analysis of the fractured surface was extended using an optical microscope and the results are provided in Fig. 4.41.

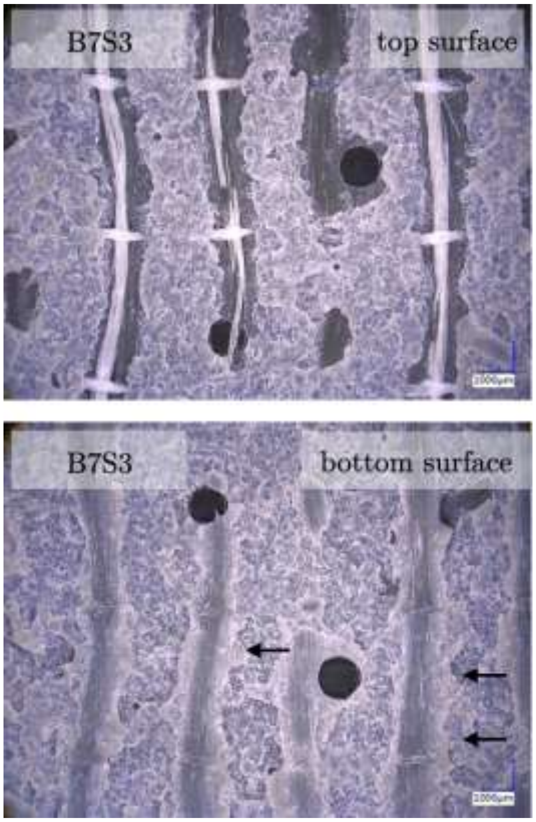

Figure 4.41: Microscopy images of DCB fracture surfaces with DP190 adhesive (crack propagation from left to right).

The selected images best show the origin of the ligaments, which are understood to be due to the lack of adhesion between the epoxy and glass fibers. Indeed, in these locations the adhesive was detached from the CFRP and underwent deformation and stretching until fracture. The horizontal arrows in Fig. 4.41 pinpoints the significant whitening of the adhesive that is associated to the above deformation mechanism.

4.3.3 Assessment of the interplay between bondline thickness and ligament bridging

The effect of ligament bridging was further investigated by increasing the thickness of the adhesive layer values > 0.4 mm. The results of DCB tests are provided in Fig. 4.42. A few remarks can be made. First of all, the load-displacement responses are quite consistent and the overall toughness was > 4 kJ/m^2.

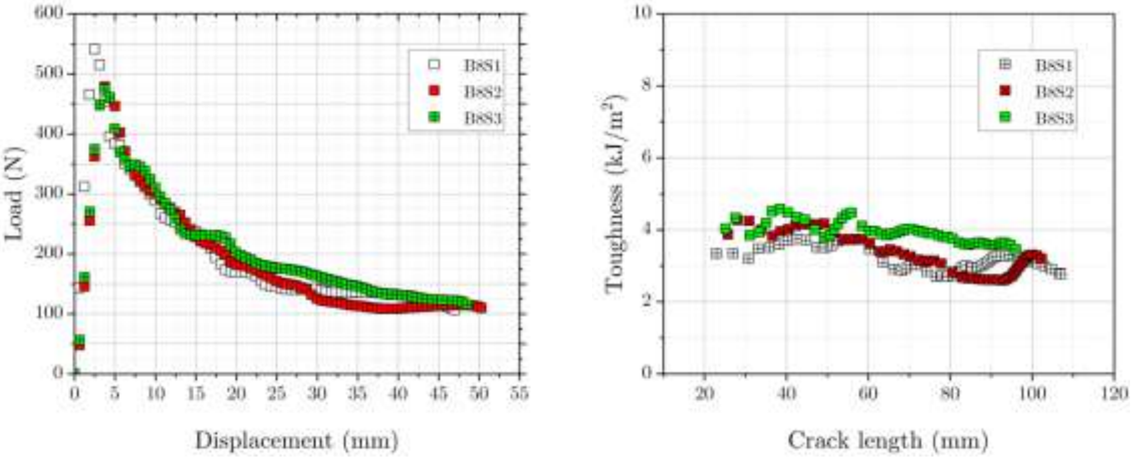

(a) (b)

Figure 4.42: (a) Load vs. displacement and (b) R-curve response for DCB specimens comprising CFRP adherends with DP190 adhesive.

The formation of the ligaments is testified by the snapshot shown below.

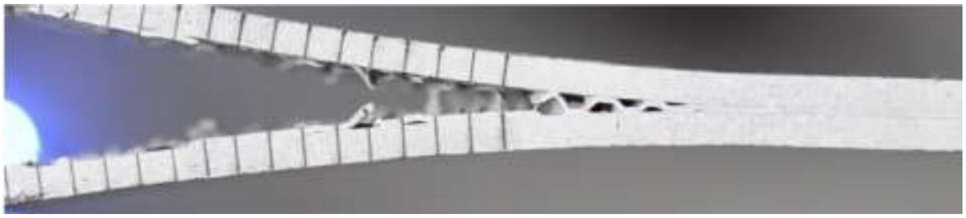

Figure 4.43: An instance of adhesive ligaments bridging the crack faces in B8.

The post failure visual inspection of the samples that indicated some spot of interfacial fracture in all samples, and most of all in B8S2. In the latter case, it might have been promoted by a competition between stretching and fracture of the thicker bondline and interfacial debonding.

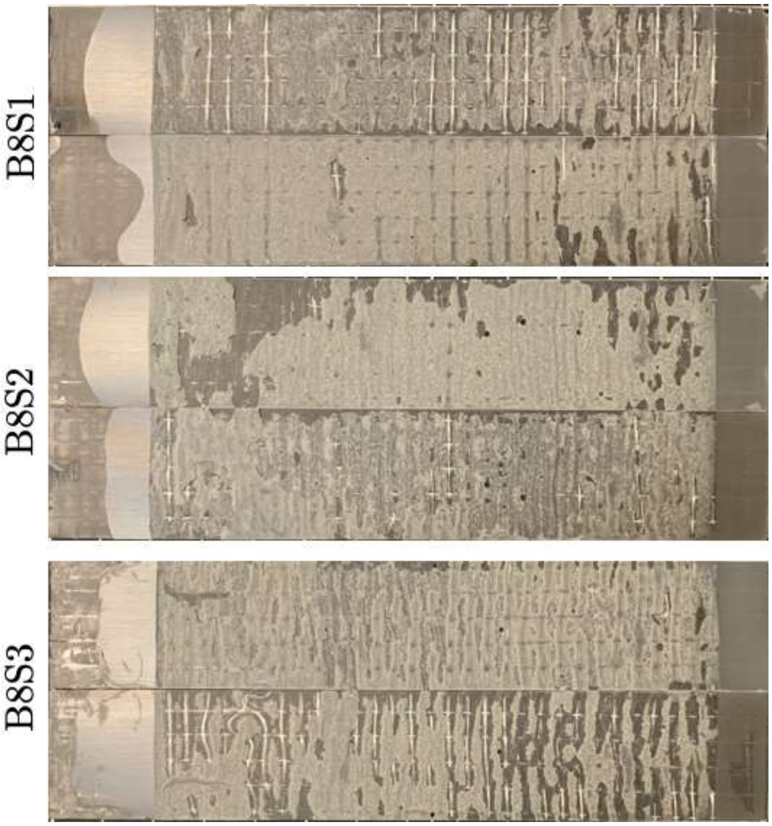

Figure 4.44: DCB DP190 batch 8 post-testing visual inspection of the fractured surfaces. Crack propagation occurring from right to left.

The overall results of B8 are summarized in Tab. 4.8. The fracture toughness is consistent and once again much greater than that adhesive found for the 3M 07333.

Table 4.8: Fracture toughness of batch 8 DCB specimens with DP190 adhesive.

Description	Sample #	Fracture toughness (N/mm)	Mechanism of fracture
• NCF_CFRP/ epoxy joints • 3M DP190 adhesive • Surface treatment: sanding	B8S1	3.20±0.32	Cohesive
	B8S2	3.33±0.53	
	B8S3	3.93±0.28	

Chapter 5: Discussion

5.1 Surface preparation and wettability

Surface preparation of the NCF-CFRP composite is an essential step for the mechanical performance of adhesive joints. First of all, previous work [89] has shown the sole surface degreasing of the current composite material does not provide satisfactory results in terms of bond strength and fracture toughness. Therefore, a surface preparation step is of fundamental importance before bonding. In the case of composite materials, the aim of surface pre-treatment is not necessarily the increase of surface roughness of the mating substrates, and it is rather the need to remove potential contaminants, such as silicon-based mold-release compounds [26]. In this study, both manual sanding and UV laser ablation were assessed.

First, the analysis of the obtained results enabled to recognize the composite surface's complexity, comprising not only carbon fibers and an epoxy matrix but also polyester stitches and supporting glass fibers close to the outer surface. Representative image of the CFRP surface in the as-produced conditions is provided in Fig. 5.1.

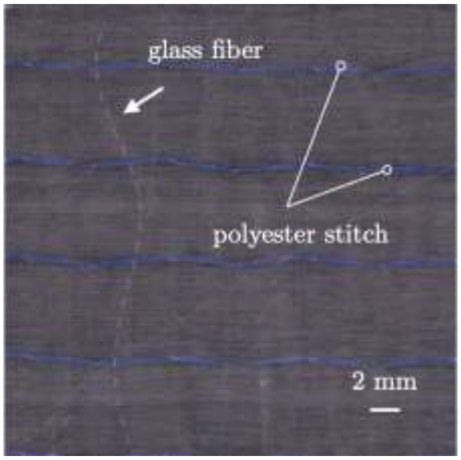

Figure 5.1: NCF-CFRP surface with polyester stitches and glass fibers highlighted.

Following the sanding treatment, a small layer of the epoxy matrix was removed while the carbon fibers were still embedded within the matrix. Indeed, no loose carbon fibers could be observed from optical microscopy and surface profilometry. Likewise, the sanding treatment could partially expose the glass fibers and the polyester stitches, but the exposure was minimal. These observations are best illustrated in Figs. 5.2(a) and (b).

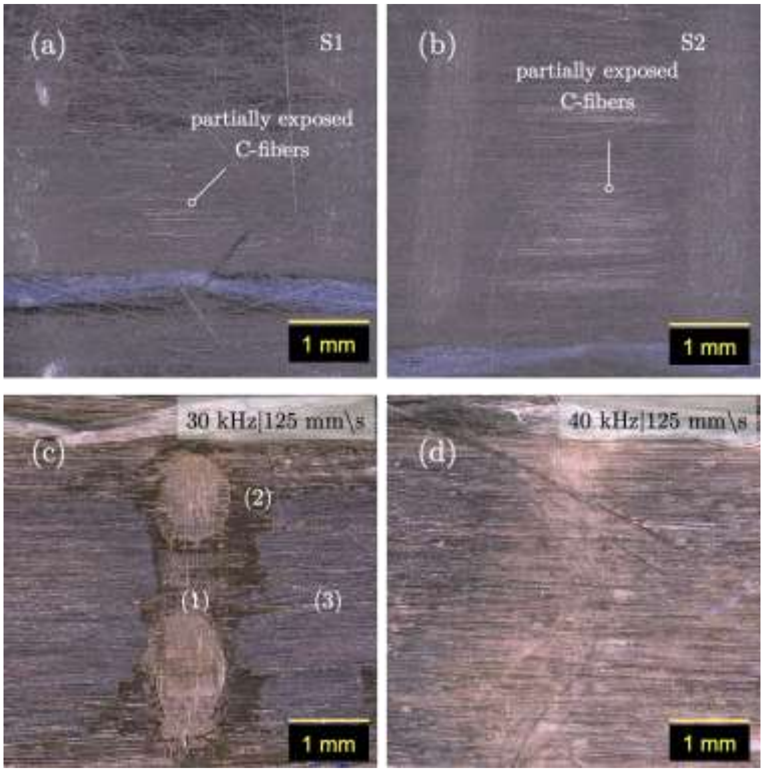

Figure 5.2: Optical images of the treated surfaces: (a) sanding S1; (b) sanding S2; (c) laser treated at 30 kHz and (d) 40 kHz).

Besides sanding, this study has also explored the effect of UV laser irradiation (355 nm) as a means to remove the outmost layer of the composite epoxy matrix. Among the various processing variables, the analysis focused on the scanning speed and pulse frequency (while keeping the power constant and equal to the maximum value allowed by the hardware). The analysis of surface morphology and topography metrics revealed that scanning speed and pulse frequency play a relevant role. Low frequency and low speed enabled removal of surface matrix leaving carbon fibers exposed. Increasing the laser speed and pulse frequency led to processing conditions that barely affected the initial surface. For instance, CFRP surfaces treated at the same speed by different pulse frequencies are shown in Fig. 5.2(c) and (d) and demonstrate the different level of glass fiber exposure and removal of epoxy matrix.

The analysis allows concluding that various pulse frequencies profoundly affected the resulting surface topography and composition. At the lower frequency, the laser could partly remove the epoxy matrix atop the glass fibers (1) and the carbon fibers (3). In addition, because of the heterogeneous composition of the CFRP surface and the different optical absorbance and thermal conductivity of the composite constituents, the effect of the laser was not uniform across the surface – see, for instance, the residual epoxy matrix remaining nearby the glass fiber (2). The UV laser wavelength can be absorbed by the polyester stiches and, as such, these were affected by the laser beam resulting in apparent damage. Thermal and chemical ablation are the main mechanisms involved with UV laser irradiation of CFRP [24]. As pointed out in [105], given the fast time scale of each UV laser pulse, the material removal mechanism is mainly contributed by thermal evaporation rather than photochemical fracture of the polymer. As such, the combined action of these removal mechanisms leads to material erosion as well as the formation of a plasma plume that contains byproducts of the process, e.g., fibers filaments and degraded epoxy. The process is depicted schematically in Fig. 5.3.

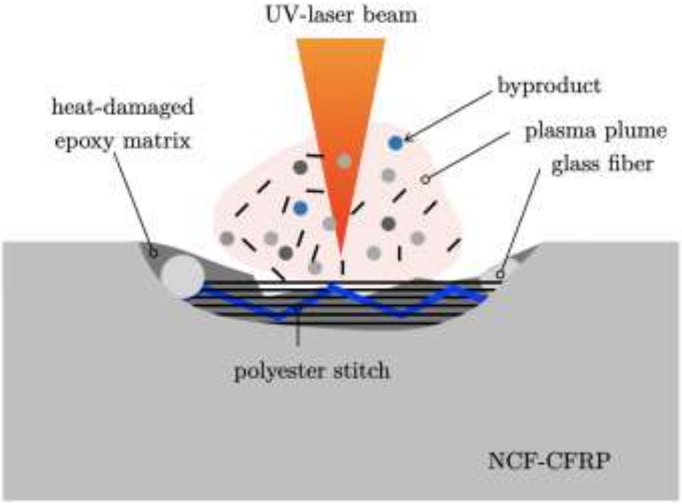

Figure 5.3: Schematic of the mechanisms potentially involved in UV-laser material removal (byproduct is the contamination/weak boundary layer in the figure).

The wettability analysis has shown a complex interaction between the treated composite and the probe liquids; therefore, a robust evaluation of SFE was not achieved. The laser treatment exacerbated the problem because of the complex surface structure. However, the previous analysis of water wettability using A.C.A. measurements indicated that the target surface is hydrophobic and so remains after sanding. In this work, it was deemed more beneficial to proceed further with mechanical characterization to assess the effects of surface treatments. Indeed, as recently stated in [22], the surface treatment of CFRP materials that results in a high percentage of epoxy matrix on the bonding surfaces may be enough for good quality composite joints, and there should not be a need to primarily increase surface energy or wettability to achieve quality bonds. But it was determined that a surface treatment must not affect the matrix/fiber interface. This last factor has important consequences on the mechanical strength of composite joints since bonding directly to lose carbon fibers can lead to poor adhesion and mechanical strength [15], [26].

5.2 Mode I DCB tests

The Mode I fracture toughness was determined considering two distinct surface preparation methods and two types of epoxy adhesives. On the one hand, the 3M 07333 structural adhesive formulation is provided with synthetic rubber in order to enhance ductility and resistance to impact and crash. On the other hand, the 3M DP190 adhesive is a two-component epoxy that comprises a variety of fillers, including carbon black. This last can improve the cohesive strength of the adhesive, besides electrical conductivity [106].

The obtained results are summarized in Fig. 5.4. It should be noted that the apparent bondline thickness was determined using optical microscopy performed by observing each side of the samples. It is recognized that such measurements may not necessarily return accurate values of the bondline; however, the results are deemed satisfactory for the sake of the current discussion.

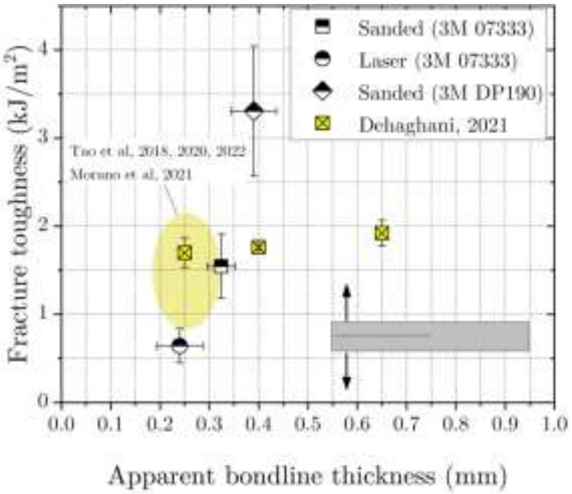

Figure 5.4: Mode I fracture toughness versus bondline thickness of the investigated adhesives as obtained using the DCB test coupon.

The Mode I fracture toughness of the laser-treated samples was the lower bound (<1 kJ/m^2). This is readily explained, considering that the mechanism of failure was merely interfacial and there was limited dissipation in the course of the separation process. Fracture occurred at the interface between the composite and the epoxy adhesive. However, for the processing condition LS1, there were exposed carbon fibers, and the failure process involved debonding at the adhesive/fiber interface. It is speculated that the matrix removal using the UV laser (LS1) caused damage to the fiber/matrix interface, and the loose fibers acted as a weak link in the DCB tests. For the processing LS2, the microscopy observations indicated very limited exposed fibers; therefore, the fracture was mainly at the interface between the epoxy adhesive and the matrix. Microscopy images reported in Fig. 5.5 illustrate the above-described mechanisms of failure.

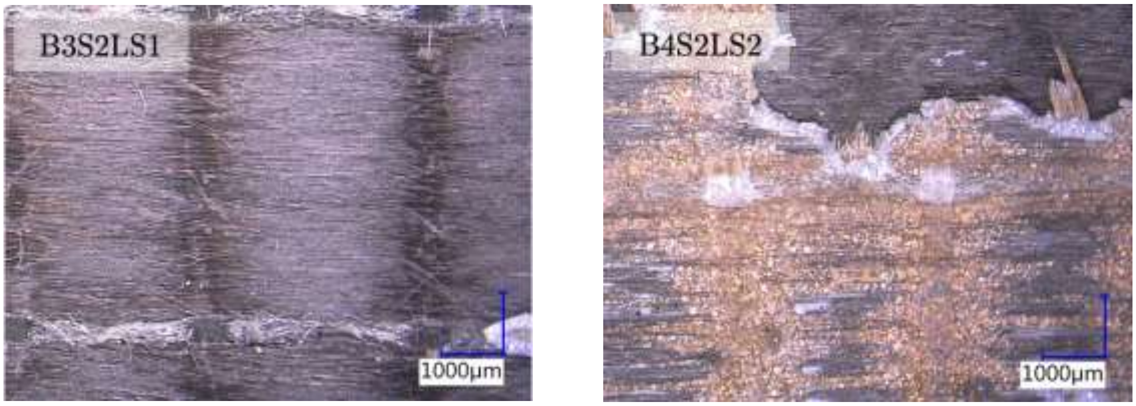

(a) (b)

Figure 5.5: Fracture surfaces of DCB samples subjected to laser treatment. (a) LS1; (b) LS2.

In particular, Fig. 5.5(a) shows the fracture surface from the composite side, with loose fibers highlighted. Fig. 5.5(b) represents the fracture surface of the samples from the adhesive side. Close inspection indicates the potential presence of byproducts (orange color) from the laser treatment, which could act as a weak boundary layer and weaken the joint.

As noted by Rauh et al. [85], when using a laser wavelength above 300 nm there is a tangible risk that the laser energy will couple into the carbon fibers, thereby deteriorating the fiber-epoxy interface. It should also be recognized that to remove "surface" contaminants that would be detrimental to adhesion, it is not necessary to have the epoxy matrix completely removed. However, the most common contaminants, such as silicone release compounds, can be embedded within the matrix after fabrication, in such cases, complete matrix removal is the only viable option to ensure effective cleaning, and contaminants free surface. Therefore, if a smoother cleaning process is aimed for, with little or no carbon fibers exposed, the presence of residual contamination has to be accepted.

The Mode I toughness of the 3M 07333 following sanding was much improved since a cohesive fracture was observed in all tests. The obtained results are also in excellent agreement with those reported Dehaghani in [91]. In particular, the combined results suggest a weak dependency of the fracture toughness on the bondline thickness for the 3M 07333 (see Fig. 5.4). The average toughness obtained herein is ≅1.5 kJ/m^2. This value is deemed satisfactory and is larger than that reported in previous work for bonded CFRPs comprising the Araldite 420 A/B (Huntsman) toughened epoxy [15] (whose values fall in the region highlighted by the yellow area in Fig. 5.4).

Finally, the second type of structural epoxy, i.e., 3M DP190, provided the best results in terms of fracture toughness. For this adhesive type, controlling the bondline thickness was challenging as the application of consolidation pressure induced the adhesive to squeeze out of the bondline (see the previous chapter for more details). Better results were obtained by increasing the layer thickness. However, it is unlikely that the improved toughness can be solely explained in terms of increased bondline thickness. Indeed, besides the occurrence of cohesive fracture, mechanical tests featuring the DP190 epoxy were characterized by the systematic formation of adhesive ligaments. An example is provided in Fig. 5.6.

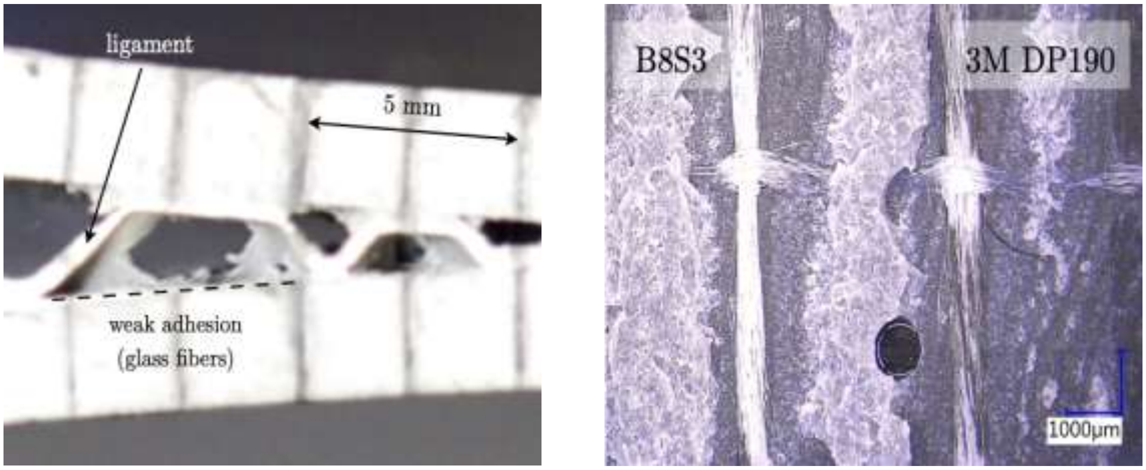

(a) (b)

Figure 5.6: (a) 3M DP190 adhesive ligaments that are bridging the crack faces. (b) Corresponding fracture surface.

The mechanism of formation can be addressed to the peculiar surface structure/composition of the NCF-CFRP. In all DCB tests featuring sanded substrates, a weak adhesion was observed at the adhesive/glass fibers interface. This is again illustrated in Fig. 5.6(b), which shows a number of exposed glass fibers across the fractured surface of the joint. The de-cohesion process of the DP190 from the glass fibers occurred closer to the interface, likely because of the higher cohesive strength of this adhesive (i.e., the cohesive strength of the adhesive > interfacial strength). The mechanism of formation of the ligaments is exemplified in Fig. 5.7(a), the schematic assumes that debonding from the glass fibers plays the most relevant role, which is confirmed by the fractured surfaces in Fig. 5.7(b).

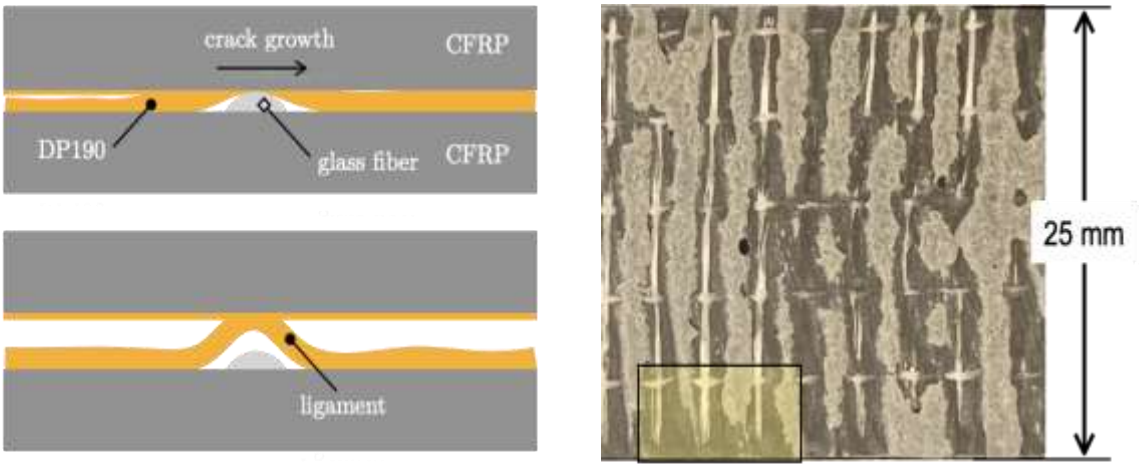

(a) (b)

Figure 5.7: Fracture surfaces of DCB joints bonded with (a) 3M 07333 and (b) DP190 structural adhesives.

The analysis also indicates that the alignment and exposure of the glass fibers have played a role since the size of the ligaments detached from the bondline is not constant and depends on the morphology of the treated surface. Besides, the area highlighted in light yellow in Fig. 5.7(b) aims to explain why from the sideview very large ligaments were observed, such as that shown above in Fig. 5.7(a). In fact, large patches of adhesive were detached from the edges of the DCB, likely because of stress concentration or cutting-induced defects affecting the CFRP.

5.3 Mode II ENF tests

Regarding mode II fracture tests, as stated earlier, steady state crack growth was not achieved. Nevertheless, the obtained results provided some interesting information. First of all, the R-curves obtained in mechanical tests carried out at different cross-head displacement rates (DR) have shown an initiation toughness that slightly increased with the applied displacement rate. The obtained data is summarized in Fig. 5.8.

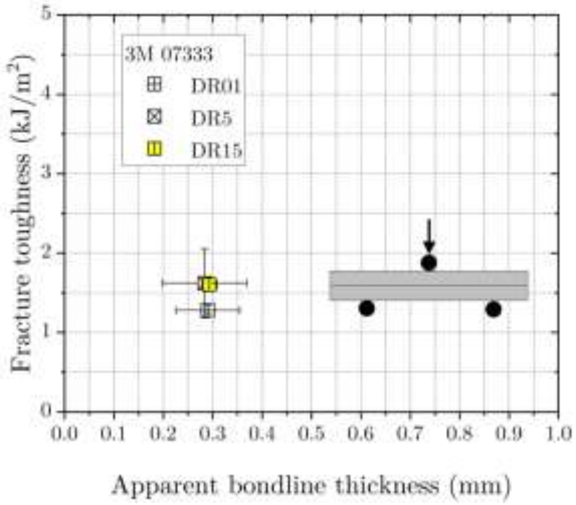

Figure 5.8: Mode II initiation fracture toughness versus bondline thickness of the 3M 07333 adhesive. (DR: cross-head displacement rate).

The dependency of the results on the cross-head displacement rate seems weak, i.e., although the average toughness slightly increases as DR increases from 0.1 mm/s to 5 mm/s, a further increase to 15 mm/s does not induce significant changes in the toughness. Besides, for increasing DR, the crack path shifted to a region closer to the interface. This is likely due to a rate effect associated with the deformation of the adhesive layer.

Finally, Fig. 5.9 reported below compares the mechanisms of fracture of the 3M 07333 adhesive under Mode I and Mode II. The direct comparison highlights distinct fracture mechanism. Indeed, there are many voids on the fracture surfaces of DCB samples, and an instance is highlighted by the arrow pointing downward in Fig. 5.9(a). The rubber modified 3M 07333 epoxy consists of an epoxy matrix featuring a dispersion of synthetic rubber. During straining, the rubber can form micro-voids that grow by plastic deformation and coalesce until the final fracture. However, it is difficult to state with certainty whether the voids originated from the above deformation mechanisms or simply by entrapped air during the fabrication process. Higher resolution observations (i.e., SEM) would be needed to shed light on this point.

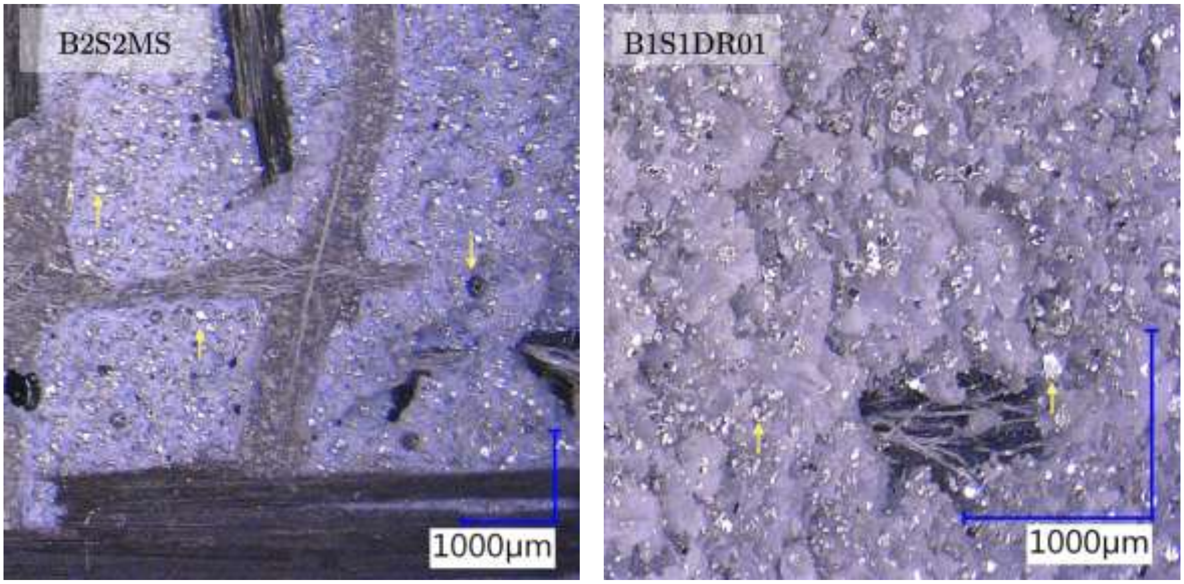

(a) (b)

Figure 5.9: Comparison between fracture surfaces of (a) DCB and (b) ENF NCF-CFRP/epoxy joints with 3M 07333 adhesive (crack propagation from left to right).

In the same figure, the arrows pointing upward pinpoint aluminum flakes that are included in the adhesive formulation. Notice that these flakes are also discernible in Fig, 5.9(b). The aluminum flakes are usually employed to promote cohesive fracture in adhesive joints [107]. The mechanism of fracture under shear was different and dominated by a ductile fracture with parabolic microcracks, which are attributed to the intense plastic (shear) straining of the adhesive layer.

Chapter 6: Conclusions and recommendations

6.1 Conclusion

The present study focused on the analysis of adhesive bonded NCF-CFRP composite materials as obtained through HP-RTM. The research work included: surface pre-treatment and characterization, mechanical testing and fractographic analysis. Surface preparation is crucial for the mechanical performance of adhesive joints. In this work, manual sanding and UV laser irradiation (355 nm) were adopted. The morphology and topography of the target surfaces before and after surface preparation were carefully evaluated. Besides, the wettability was investigated using contact angle measurements. Two load cases were considered for mechanical testing of the composite joints, the DCB test to determine the Mode I fracture toughness and the ENF test to assess the Mode II fracture toughness. In-situ CCD imaging during testing, post-failure visual inspection, and optical observations was used to shed light on the mechanisms of deformation and fracture of the joints.

The following conclusions can be drawn.

- **The interaction between probe liquids and the NCF-CFRP surface has an adverse effect on wettability measurements**

The static contact angles have shown a continuous variation over a significant time window thus raising important questions concerning the interaction between the probe liquids and the complex NCF-CFRP surfaces. The determination of a static contact angle assumes the solid\liquid contact area to remain unchanged during the measurement, i.e., the drop is in a global energy equilibrium condition. Among potential reasons for such behavior, it is worth mentioning that the probe liquids may have interacted with the target material, e.g., they might well be subjected to volume reduction following evaporation or penetration within any small crevices or microcracks of the complex heterogeneous composite surface layer. More robust measurements were obtained using advancing contact angle measurements with deionized water. The results have shown a good agreement with Wenzel’s wetting regime and indicated that the composite surface has a hydrophobic character before and after surface treatment. Whether this outcome is dependent on the surface structure of the composite, comprising epoxy matrix, carbon, glass and polyester fibers, or merely on the chemistry of the matrix material remains to be established.

- **A simple sanding treatment can provide satisfactory results, i.e., cohesive fracture**

The results of mechanical tests executed on adhesive joints with sanded interfaces have shown satisfactory results, in that the fracture process involved cohesive fracture within the adhesive layer with both adhesives. It is however noted that adhesion to polyester and glass fibers was much weaker and triggered near-interfacial debonding. This last did not seem to affect negatively the performance of the joints, rather, it has triggered additional dissipation in DCB joints bonded with the DP190 adhesive through large adhesive ligament bridging. The fact that sanding induces cohesive fracture does not rule out the need to assess other surface preparation strategies, i.e., pulsed laser. Indeed, sanding remains a manual process, as such, it is time consuming and operator dependent.

- **The UV-laser processing requires additional iterations**

The present study has included an exploratory investigation of UV-laser irradiation of NCF-CFRP composite plates. The interaction between the complex surface structure of the composite, comprising epoxy matrix as well as carbon, glass and polyester fibers, did not allow to obtain satisfactory results, neither in terms of wettability nor fracture toughness. Besides, it was determined that the processing condition that exposed carbon fibers has indeed generated damage at the epoxy matrix/carbon fiber interfaces, i.e., exposed fibers were loose. This suggests that the radiation wavelength of the laser implies coupling of the laser energy within the carbon fibers and, as such, a photothermal ablation mechanism. What is more, the laser processing that did not expose carbon fibers could not allow for improving fracture toughness as the presence of potential byproducts of the process has likely created a weak boundary layer.

- **The interplay between adhesive type and the composite surface structure can trigger additional dissipation mechanisms**

The DP 190 adhesive provided bridging ligaments during fracture tests that enhanced dissipation. It is believed that the cohesive strength of the DP190 is larger than that of the 3M 07333 and that should help explaining the high density of adhesive ligaments bridging the crack faces. Notice that bridging enabled by adhesive ligaments (i.e., bondline detached from both interfaces and bridging the crack faces) has been shown to be a powerful toughening mechanism of composite joints [26], [27]. The obtained results indicates that some form of bridging is enabled by the peculiar architecture of the NCF-CFRP. However, the occurrence of such ligaments is not entirely under control as it depends on the alignment between the glass fibers belonging to the top and bottom substrates.

- **The (initiation) fracture toughness in Mode II does not show large sensitivity to the displacement rate**

Steady-state crack growth was not achieved in Mode II tests. The fracture toughness largely increased with crack growth and only the initiation values were quoted in this work. The deformation pattern observed during mechanical testing suggested that a large straining occurred during shearing of the adhesive layer owing to the ductility of the adhesive, which was facilitated by the addition of synthetic rubber. Besides, increasing the displacement rate shifted the crack path toward the interface, suggesting that the rate-dependent behavior of the adhesive might have played a role. The ENF tests were not executed with the DP190. The toughness of the DP190 was very high and fracture of the composite was triggered before crack initiation within the adhesive layer.

6.2 Recommendations for future works

- The study of surface wetting should be expanded considering additional probe liquids that can allow a better control of liquid dispensing during advancing and receding contact angle measurements.
- Further analysis of the interaction between laser irradiation and the complex surface structure of the composites is suggested. It is likely necessary to narrow down the processing window and fine tune the laser treatment by making sure that no damage is induced at matrix/epoxy interfaces as well as that any weak boundary layer is generated in the process. Besides, it would be advisable to also explore near-IR and IR lasers. Indeed, these are driven by optical fibers and may allow a much efficient processing in terms of time and size of the target area.
- High resolution electron microscopy and surface analytical chemistry analysis may be helpful to reveal the interplay between surface treatment and actual surface morphological and chemical modifications. Besides, it might provide a deeper understanding of the mechanisms of fracture.
- It is suggested to perform additional Mode II tests using longer samples to assess the propagation fracture toughness following the full development of the fracture process zone. However, it is recognized that this task might require the use of thicker laminates to prevent nucleation of damage within the composite substrate at the pin contact point during three point bending tests.

- The ability to trigger ligament bridging is a very interesting outcome that has been facilitated by the specific structure of the composite material employed in this study. The ligaments were promoted by the lack of adhesion between the epoxy and the exposed glass fibers. A precise control on the formation and deployment of these ligaments could be enabled by tailoring the architecture of the NCF. Therefore, as a potential extension it might be interesting to investigate on whether the composite and/or adhesive joints fabrication process can be tailored to trigger such ligaments in a controllable fashion.

Letters of copyright permission

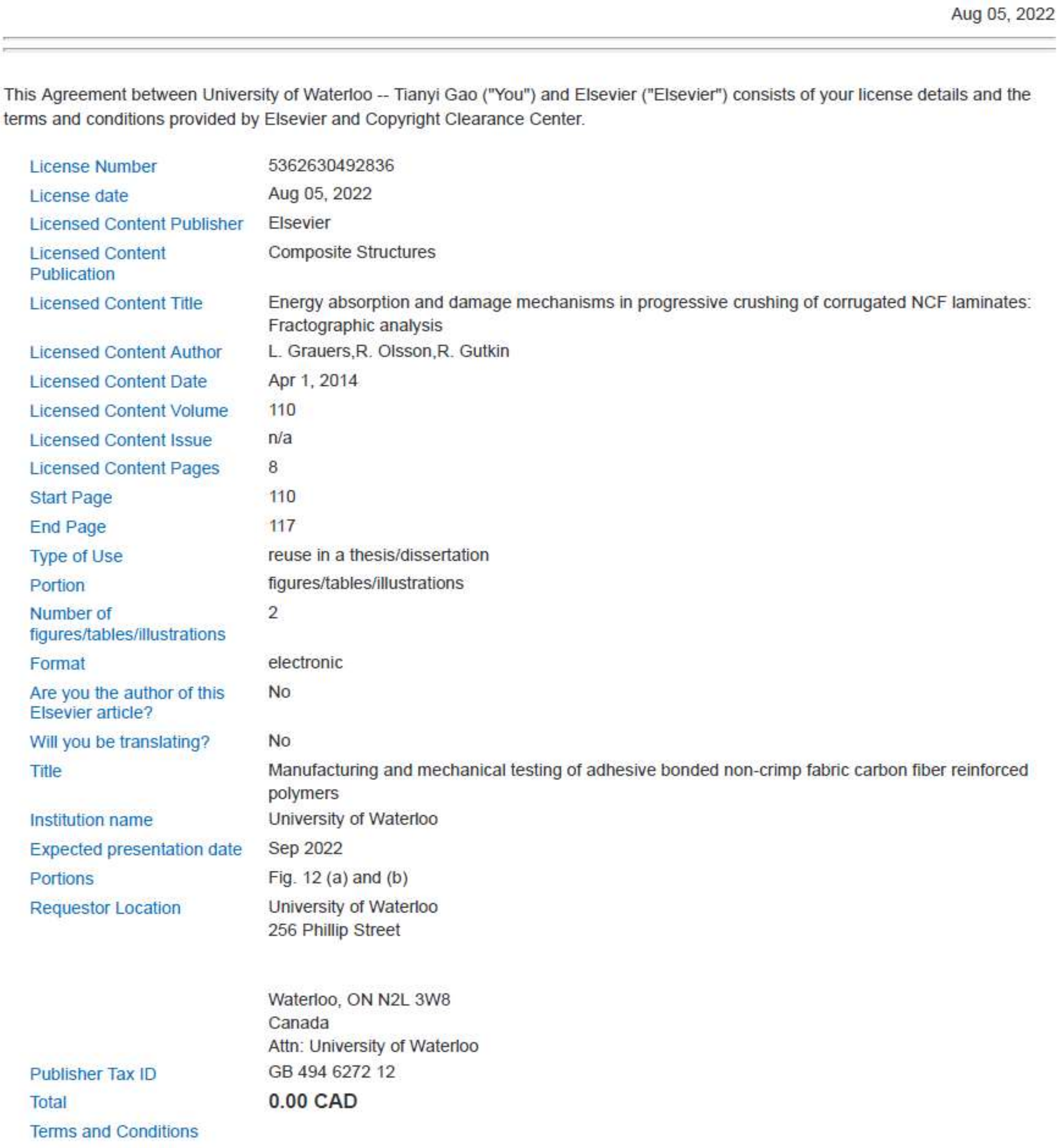

Aug 05, 2022

This Agreement between University of Waterloo -- Tianyi Gao ("You") and Elsevier ("Elsevier") consists of your license details and the terms and conditions provided by Elsevier and Copyright Clearance Center.

License Number	5362630492836
License date	Aug 05, 2022
Licensed Content Publisher	Elsevier
Licensed Content Publication	Composite Structures
Licensed Content Title	Energy absorption and damage mechanisms in progressive crushing of corrugated NCF laminates: Fractographic analysis
Licensed Content Author	L. Grauers,R. Olsson,R. Gutkin
Licensed Content Date	Apr 1, 2014
Licensed Content Volume	110
Licensed Content Issue	n/a
Licensed Content Pages	8
Start Page	110
End Page	117
Type of Use	reuse in a thesis/dissertation
Portion	figures/tables/illustrations
Number of figures/tables/illustrations	2
Format	electronic
Are you the author of this Elsevier article?	No
Will you be translating?	No
Title	Manufacturing and mechanical testing of adhesive bonded non-crimp fabric carbon fiber reinforced polymers
Institution name	University of Waterloo
Expected presentation date	Sep 2022
Portions	Fig. 12 (a) and (b)
Requestor Location	University of Waterloo 256 Phillip Street Waterloo, ON N2L 3W8 Canada Attn: University of Waterloo
Publisher Tax ID	GB 494 6272 12
Total	**0.00 CAD**
Terms and Conditions	

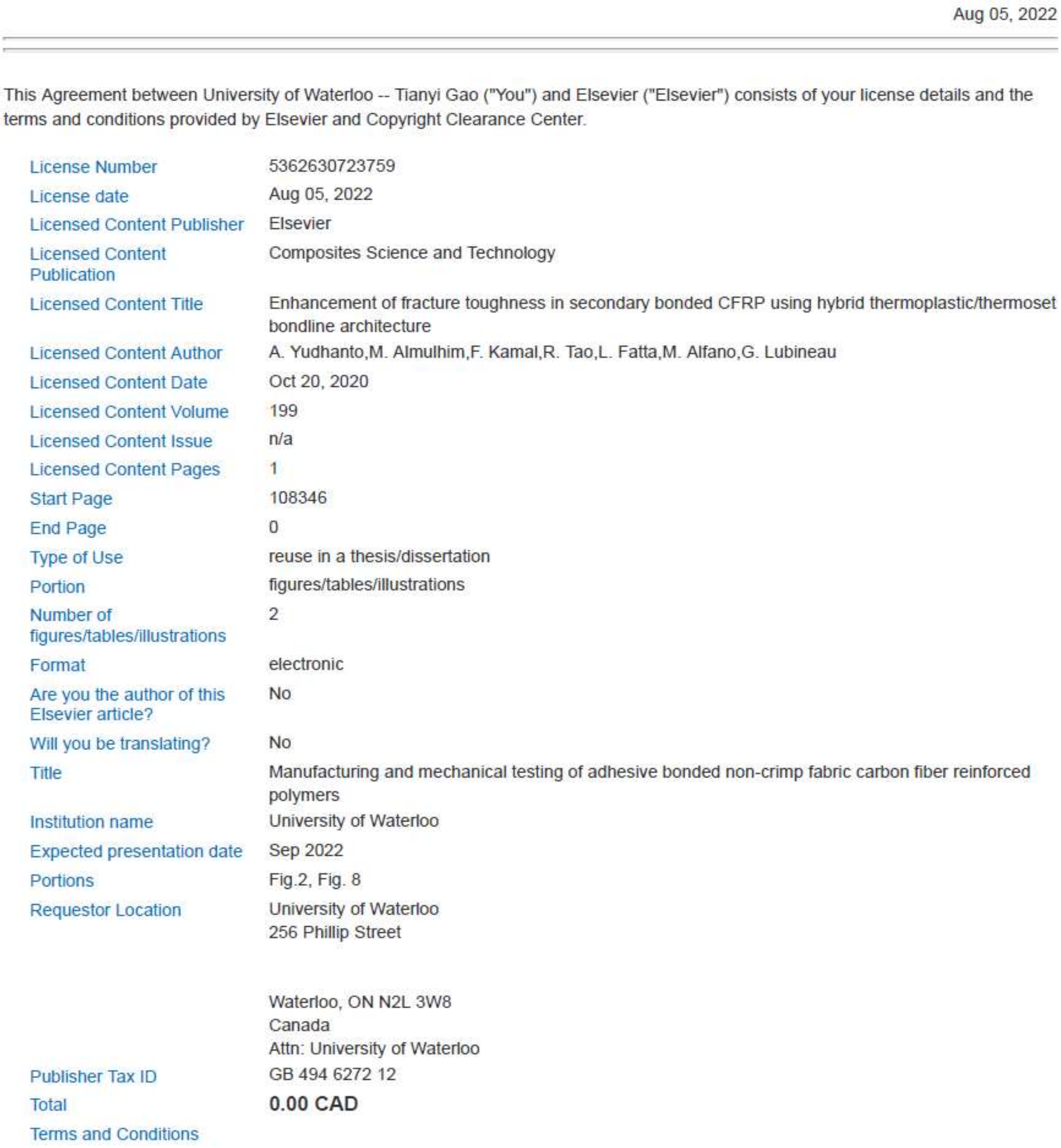

Aug 05, 2022

This Agreement between University of Waterloo -- Tianyi Gao ("You") and Elsevier ("Elsevier") consists of your license details and the terms and conditions provided by Elsevier and Copyright Clearance Center.

License Number	5362630723759
License date	Aug 05, 2022
Licensed Content Publisher	Elsevier
Licensed Content Publication	Composites Science and Technology
Licensed Content Title	Enhancement of fracture toughness in secondary bonded CFRP using hybrid thermoplastic/thermoset bondline architecture
Licensed Content Author	A. Yudhanto,M. Almulhim,F. Kamal,R. Tao,L. Fatta,M. Alfano,G. Lubineau
Licensed Content Date	Oct 20, 2020
Licensed Content Volume	199
Licensed Content Issue	n/a
Licensed Content Pages	1
Start Page	108346
End Page	0
Type of Use	reuse in a thesis/dissertation
Portion	figures/tables/illustrations
Number of figures/tables/illustrations	2
Format	electronic
Are you the author of this Elsevier article?	No
Will you be translating?	No
Title	Manufacturing and mechanical testing of adhesive bonded non-crimp fabric carbon fiber reinforced polymers
Institution name	University of Waterloo
Expected presentation date	Sep 2022
Portions	Fig.2, Fig. 8
Requestor Location	University of Waterloo 256 Phillip Street Waterloo, ON N2L 3W8 Canada Attn: University of Waterloo
Publisher Tax ID	GB 494 6272 12
Total	**0.00 CAD**
Terms and Conditions	

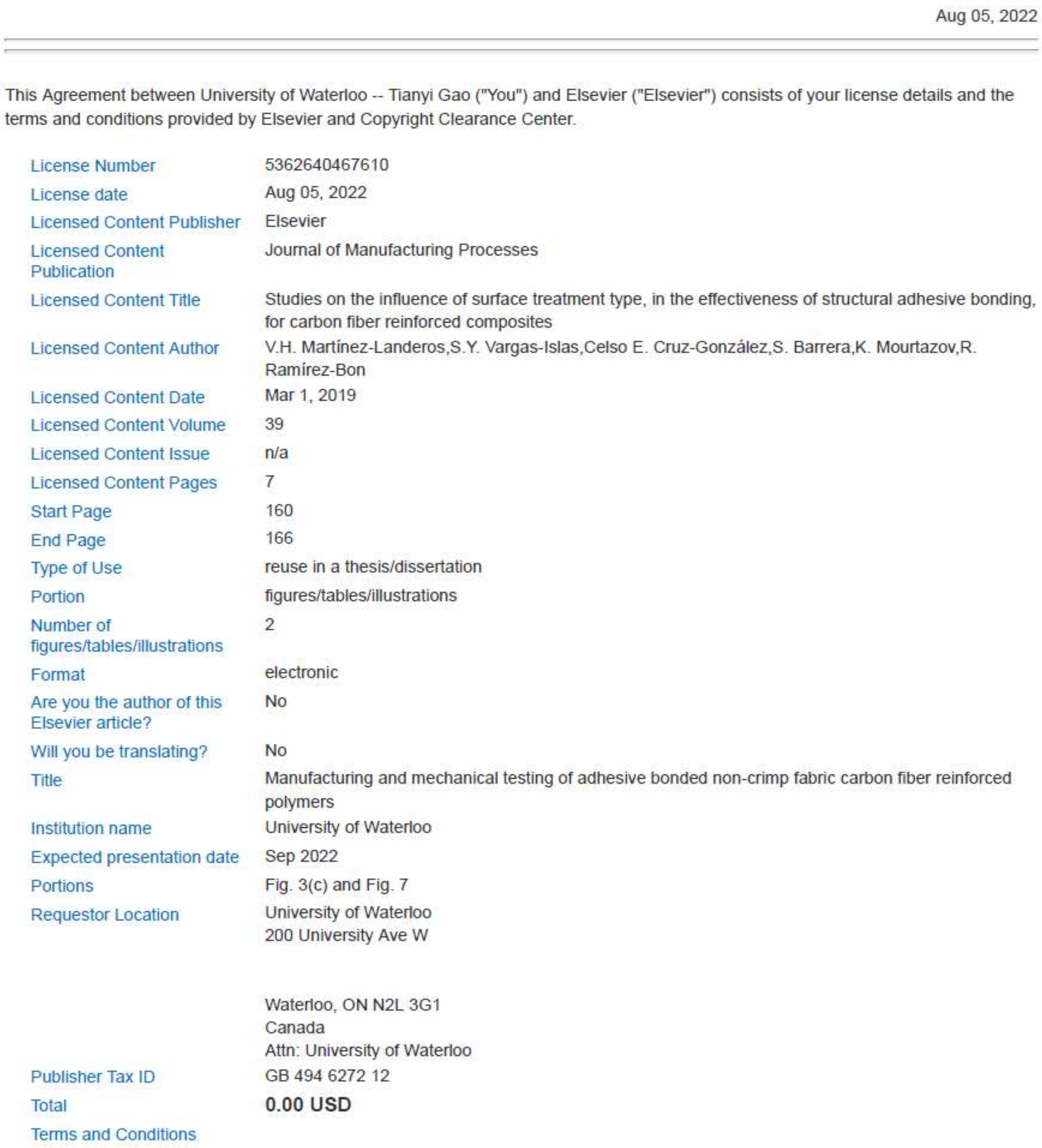

Aug 05, 2022

This Agreement between University of Waterloo -- Tianyi Gao ("You") and Elsevier ("Elsevier") consists of your license details and the terms and conditions provided by Elsevier and Copyright Clearance Center.

License Number	5362640467610
License date	Aug 05, 2022
Licensed Content Publisher	Elsevier
Licensed Content Publication	Journal of Manufacturing Processes
Licensed Content Title	Studies on the influence of surface treatment type, in the effectiveness of structural adhesive bonding, for carbon fiber reinforced composites
Licensed Content Author	V.H. Martínez-Landeros,S.Y. Vargas-Islas,Celso E. Cruz-González,S. Barrera,K. Mourtazov,R. Ramírez-Bon
Licensed Content Date	Mar 1, 2019
Licensed Content Volume	39
Licensed Content Issue	n/a
Licensed Content Pages	7
Start Page	160
End Page	166
Type of Use	reuse in a thesis/dissertation
Portion	figures/tables/illustrations
Number of figures/tables/illustrations	2
Format	electronic
Are you the author of this Elsevier article?	No
Will you be translating?	No
Title	Manufacturing and mechanical testing of adhesive bonded non-crimp fabric carbon fiber reinforced polymers
Institution name	University of Waterloo
Expected presentation date	Sep 2022
Portions	Fig. 3(c) and Fig. 7
Requestor Location	University of Waterloo 200 University Ave W Waterloo, ON N2L 3G1 Canada Attn: University of Waterloo
Publisher Tax ID	GB 494 6272 12
Total	**0.00 USD**
Terms and Conditions	

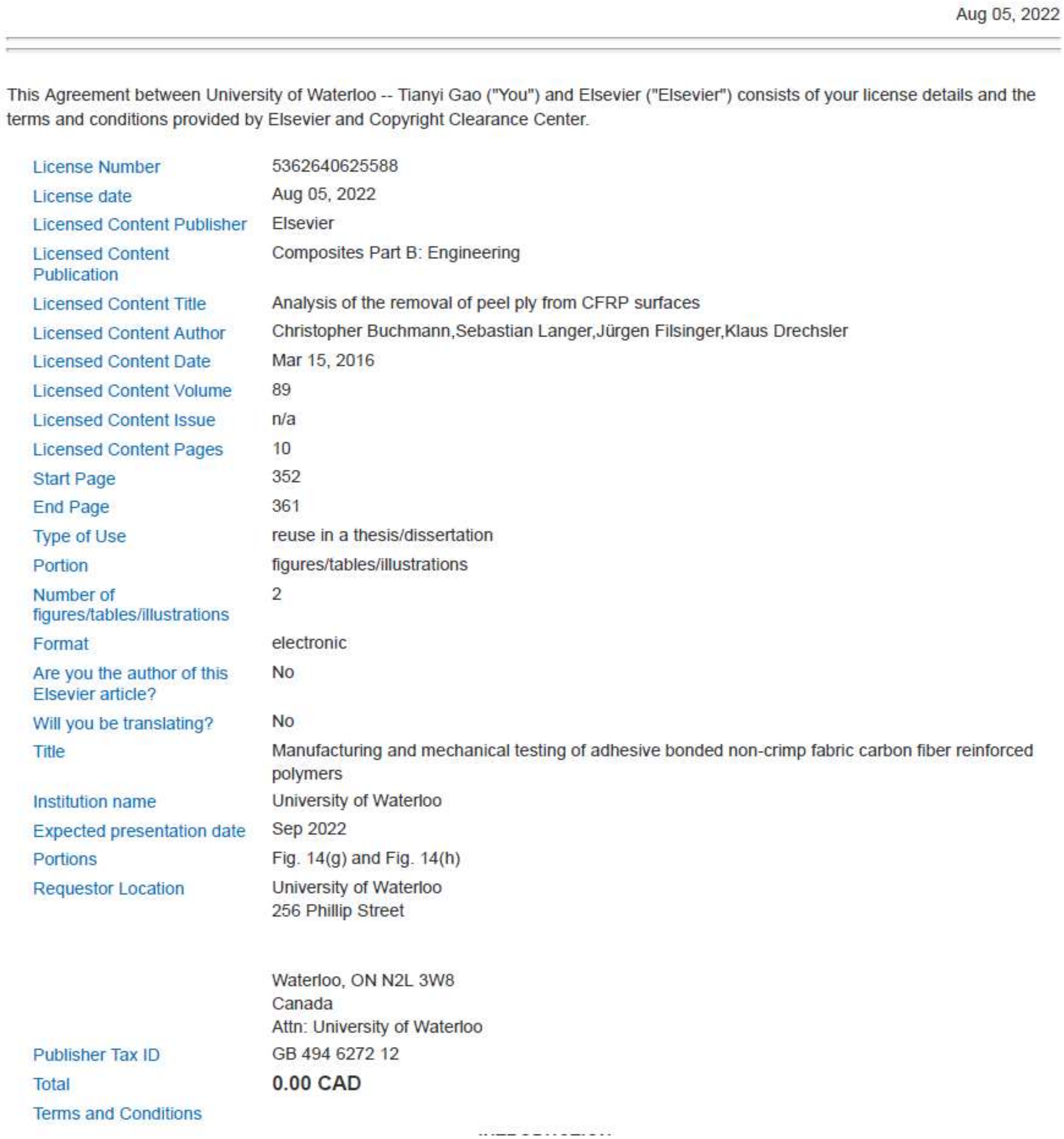

Aug 05, 2022

This Agreement between University of Waterloo -- Tianyi Gao ("You") and Elsevier ("Elsevier") consists of your license details and the terms and conditions provided by Elsevier and Copyright Clearance Center.

License Number	5362640625588
License date	Aug 05, 2022
Licensed Content Publisher	Elsevier
Licensed Content Publication	Composites Part B: Engineering
Licensed Content Title	Analysis of the removal of peel ply from CFRP surfaces
Licensed Content Author	Christopher Buchmann,Sebastian Langer,Jürgen Filsinger,Klaus Drechsler
Licensed Content Date	Mar 15, 2016
Licensed Content Volume	89
Licensed Content Issue	n/a
Licensed Content Pages	10
Start Page	352
End Page	361
Type of Use	reuse in a thesis/dissertation
Portion	figures/tables/illustrations
Number of figures/tables/illustrations	2
Format	electronic
Are you the author of this Elsevier article?	No
Will you be translating?	No
Title	Manufacturing and mechanical testing of adhesive bonded non-crimp fabric carbon fiber reinforced polymers
Institution name	University of Waterloo
Expected presentation date	Sep 2022
Portions	Fig. 14(g) and Fig. 14(h)
Requestor Location	University of Waterloo 256 Phillip Street Waterloo, ON N2L 3W8 Canada Attn: University of Waterloo
Publisher Tax ID	GB 494 6272 12
Total	**0.00 CAD**
Terms and Conditions	

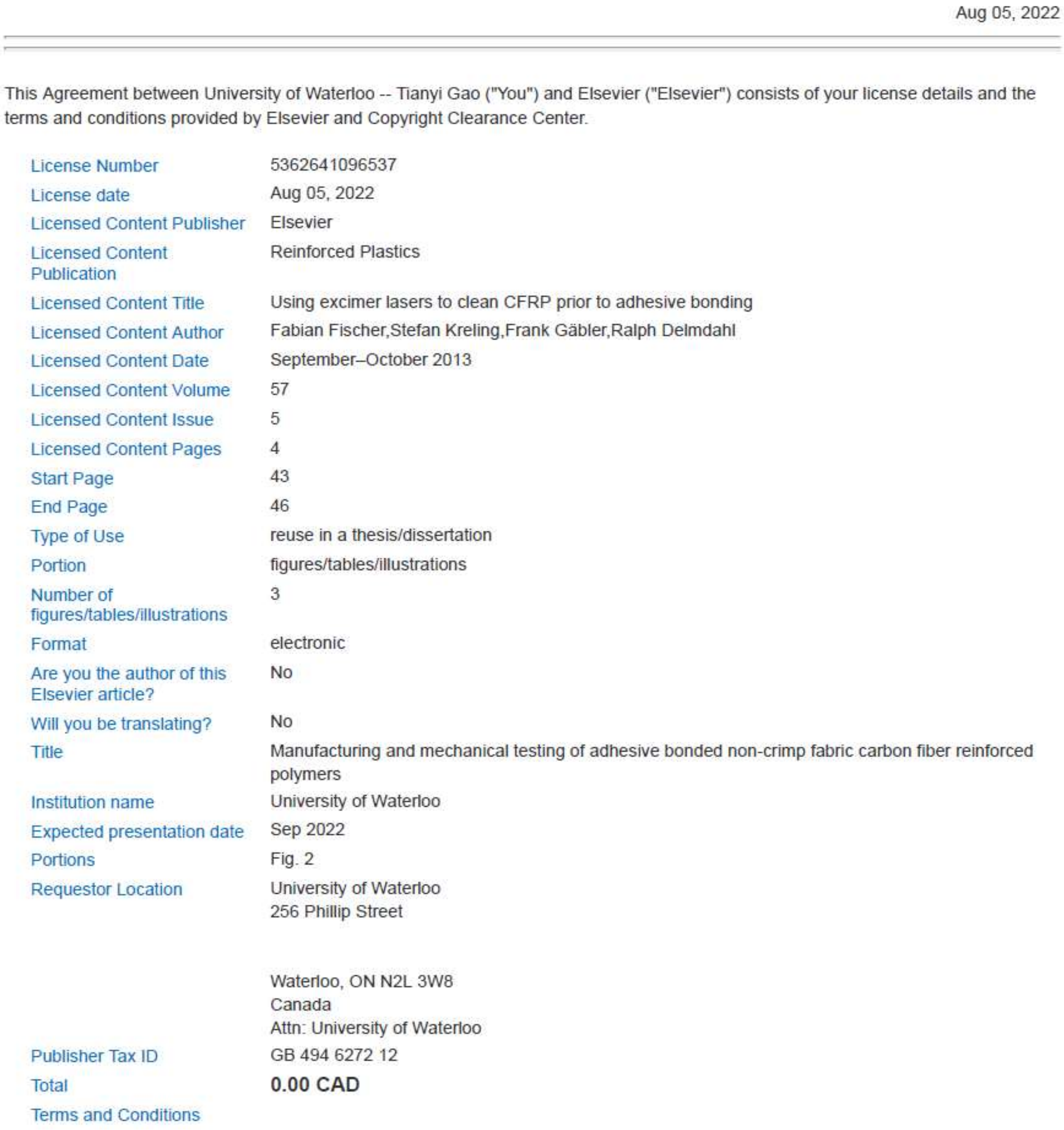

Aug 05, 2022

This Agreement between University of Waterloo -- Tianyi Gao ("You") and Elsevier ("Elsevier") consists of your license details and the terms and conditions provided by Elsevier and Copyright Clearance Center.

License Number	5362641096537
License date	Aug 05, 2022
Licensed Content Publisher	Elsevier
Licensed Content Publication	Reinforced Plastics
Licensed Content Title	Using excimer lasers to clean CFRP prior to adhesive bonding
Licensed Content Author	Fabian Fischer,Stefan Kreling,Frank Gäbler,Ralph Delmdahl
Licensed Content Date	September–October 2013
Licensed Content Volume	57
Licensed Content Issue	5
Licensed Content Pages	4
Start Page	43
End Page	46
Type of Use	reuse in a thesis/dissertation
Portion	figures/tables/illustrations
Number of figures/tables/illustrations	3
Format	electronic
Are you the author of this Elsevier article?	No
Will you be translating?	No
Title	Manufacturing and mechanical testing of adhesive bonded non-crimp fabric carbon fiber reinforced polymers
Institution name	University of Waterloo
Expected presentation date	Sep 2022
Portions	Fig. 2
Requestor Location	University of Waterloo 256 Phillip Street Waterloo, ON N2L 3W8 Canada Attn: University of Waterloo
Publisher Tax ID	GB 494 6272 12
Total	**0.00 CAD**
Terms and Conditions	

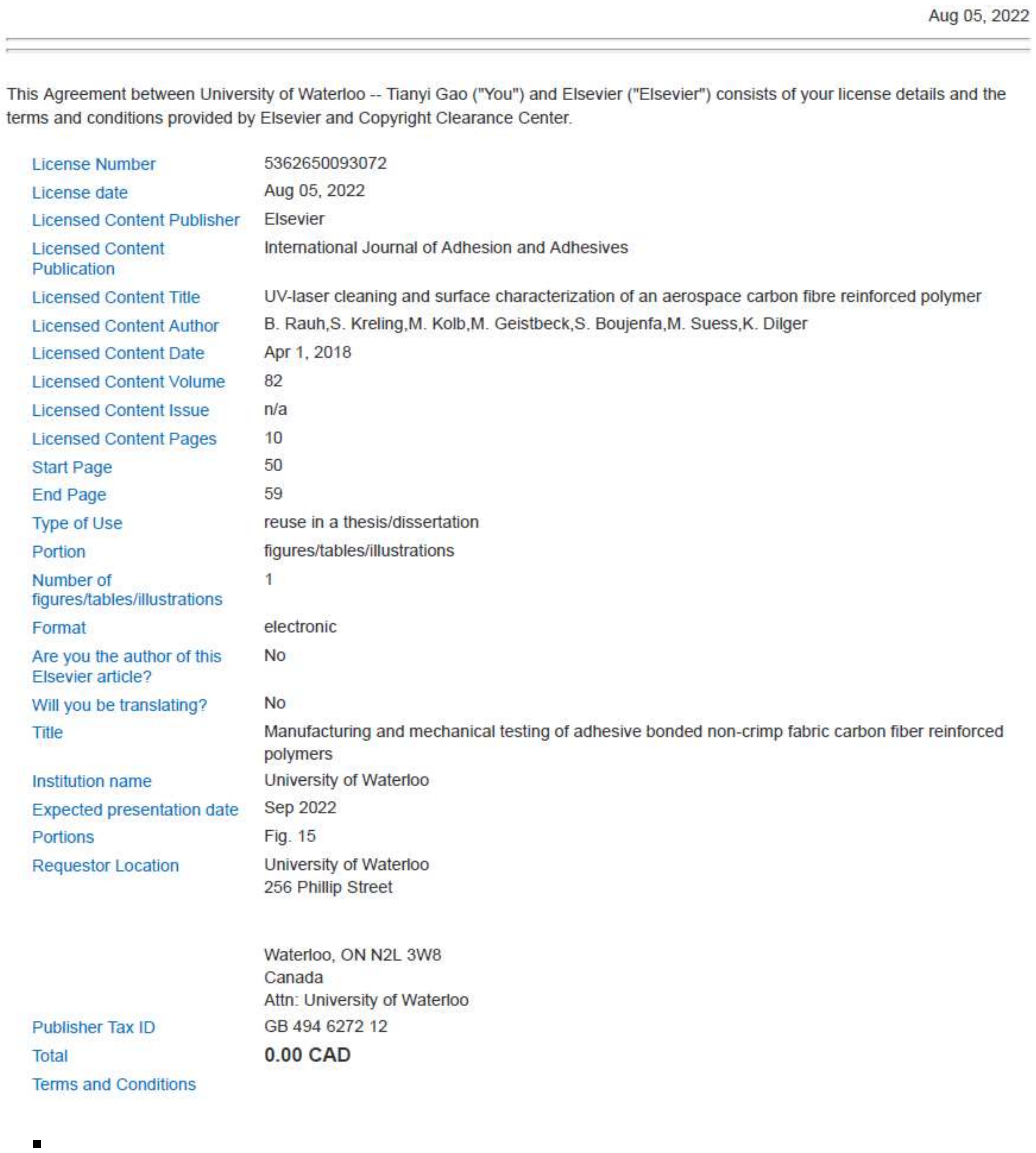

Aug 05, 2022

This Agreement between University of Waterloo -- Tianyi Gao ("You") and Elsevier ("Elsevier") consists of your license details and the terms and conditions provided by Elsevier and Copyright Clearance Center.

License Number	5362650093072
License date	Aug 05, 2022
Licensed Content Publisher	Elsevier
Licensed Content Publication	International Journal of Adhesion and Adhesives
Licensed Content Title	UV-laser cleaning and surface characterization of an aerospace carbon fibre reinforced polymer
Licensed Content Author	B. Rauh,S. Kreling,M. Kolb,M. Geistbeck,S. Boujenfa,M. Suess,K. Dilger
Licensed Content Date	Apr 1, 2018
Licensed Content Volume	82
Licensed Content Issue	n/a
Licensed Content Pages	10
Start Page	50
End Page	59
Type of Use	reuse in a thesis/dissertation
Portion	figures/tables/illustrations
Number of figures/tables/illustrations	1
Format	electronic
Are you the author of this Elsevier article?	No
Will you be translating?	No
Title	Manufacturing and mechanical testing of adhesive bonded non-crimp fabric carbon fiber reinforced polymers
Institution name	University of Waterloo
Expected presentation date	Sep 2022
Portions	Fig. 15
Requestor Location	University of Waterloo 256 Phillip Street Waterloo, ON N2L 3W8 Canada Attn: University of Waterloo
Publisher Tax ID	GB 494 6272 12
Total	**0.00 CAD**
Terms and Conditions	

Bibliography

[1] "Obama Administration Finalizes Historic 54.5 MPG Fuel Efficiency Standards | whitehouse.gov." https://obamawhitehouse.archives.gov/the-press-office/2012/08/28/obama-administration-finalizes-historic-545-mpg-fuel-efficiency-standard (accessed Jul. 02, 2022).

[2] K. Sridharan, B. Srinivasu, and V. Pudi, "The Road Ahead," *Carbon Nanostructures*, pp. 83–86, 2020, doi: 10.1007/978-3-030-50699-5_9.

[3] "Canada to copy Obama's fuel efficiency rules - The Globe and Mail." https://www.theglobeandmail.com/report-on-business/industry-news/energy-and-resources/canada-to-copy-obamas-fuel-efficiency-rules/article4508608/ (accessed Jul. 02, 2022).

[4] G. Gardiner, "4." https://www.compositesworld.com/articles/bmw-7-series-plant- dingolfing-germany

[5] S. Das, D. Graziano, V. K. K. Upadhyayula, E. Masanet, M. Riddle, and J. Cresko, "Vehicle lightweighting energy use impacts in U.S. light-duty vehicle fleet," *Sustainable Materials and Technologies*, vol. 8, pp. 5–13, 2016, doi: 10.1016/j.susmat.2016.04.001.

[6] A. T. Mayyas, A. Qattawi, A. R. Mayyas, and M. A. Omar, "Life cycle assessment-based selection for a sustainable lightweight body-in-white design," *Energy*, vol. 39, no. 1, pp. 412–425, 2012, doi: 10.1016/j.energy.2011.12.033.

[7] W. J. Joost, "Reducing vehicle weight and improving U.S. energy efficiency using integrated computational materials engineering," *Jom*, vol. 64, no. 9, pp. 1032–1038, 2012, doi: 10.1007/s11837-012-0424-z.

[8] G. Zhu, G. Sun, H. Yu, S. Li, and Q. Li, "Energy absorption of metal, composite and metal/composite hybrid structures under oblique crushing loading," *Int J Mech Sci*, vol. 135, no. September 2017, pp. 458–483, 2018, doi: 10.1016/j.ijmecsci.2017.11.017.

[9] A. Cherniaev, C. Butcher, and J. Montesano, "Predicting the axial crush response of CFRP tubes using three damage-based constitutive models," *Thin-Walled Structures*, vol. 129, no. April, pp. 349–364, 2018, doi: 10.1016/j.tws.2018.05.003.

[10] G. C. Jacob, J. F. Fellers, S. Simunovic, and J. M. Starbuck, "Energy absorption in polymer composites for automotive crashworthiness," *J Compos Mater*, vol. 36, no. 7, pp. 813–850, 2002, doi: 10.1177/0021998302036007164.

[11] H. (Edag Inc.) Singh, “Mass Reduction for Light-Duty Vehicles for Model Years 2017-2025 Final Report,” *Report No. DOT HS 811 666*, no. August, p. 582, 2012.

[12] “CFRP materials - Audi Technology Portal.” https://www.audi-technology-portal.de/en/body/materials/cfrp-materials (accessed Jul. 02, 2022).

[13] “Lamborghini Murciélago LP 670 SuperVeloce - Technical Specifications.” https://www.lamborghini.com/en-en/history/murcielago-lp-670-superveloce (accessed Jul. 02, 2022).

[14] “HP-RTM on the rise | CompositesWorld.” https://www.compositesworld.com/articles/hp-rtm-on-the-rise (accessed Jul. 02, 2022).

[15] C. Morano, R. Tao, M. Alfano, and G. Lubineau, “Effect of mechanical pretreatments on damage mechanisms and fracture toughness in cfrp/epoxy joints,” *Materials*, vol. 14, no. 6, pp. 1–16, 2021, doi: 10.3390/ma14061512.

[16] S. A. Tx, “COMPOSITES AFFORDABILITY INITIATIVE 2006 ASIP Conference,” 2006.

[17] M. Zeighami and F. Honarvar, “New approaches for testing of adhesive joints by ultrasonic C-scan imaging technique,” *Mater Eval*, vol. 67, no. 8, pp. 945–954, 2009.

[18] J. Holtmannspötter, J. V. Czarnecki, M. Wetzel, D. Dolderer, and C. Eisenschink, “The use of peel ply as a method to create reproduceable but contaminated surfaces for structural adhesive bonding of carbon fiber reinforced plastics,” *Journal of Adhesion*, vol. 89, no. 2. pp. 96–110, 2013. doi: 10.1080/00218464.2012.731828.

[19] M. Wetzel, J. Holtmannspötter, H. J. Gudladt, and J. V. Czarnecki, “Sensitivity of double cantilever beam test to surface contamination and surface pretreatment,” *Int J Adhes Adhes*, vol. 46, pp. 114–121, 2013, doi: 10.1016/j.ijadhadh.2013.06.002.

[20] D. N. Markatos, K. I. Tserpes, E. Rau, S. Markus, B. Ehrhart, and S. Pantelakis, “The effects of manufacturing-induced and in-service related bonding quality reduction on the mode-I fracture toughness of composite bonded joints for aeronautical use,” *Compos B Eng*, vol. 45, no. 1, pp. 556–564, 2013, doi: 10.1016/j.compositesb.2012.05.052.

[21] T. Takeda, T. Yasuoka, H. Hoshi, S. Sugimoto, and Y. Iwahori, “Effectiveness of flame-based surface treatment for adhesive bonding of carbon fiber reinforced epoxy matrix composites,” *Compos Part A Appl Sci Manuf*, vol. 119, no. September 2018, pp. 30–37, 2019, doi: 10.1016/j.compositesa.2019.01.013.

[22] J. Holtmannspötter, “How surfaces of carbon fiber reinforced plastics with thermoset matrices need to be treated for structural adhesive bonding,” *Journal of Adhesion*, vol. 96, no. 9, pp. 839–854, 2020, doi: 10.1080/00218464.2018.1519702.

[23] J. de Freese, J. Holtmannspötter, S. Raschendorfer, and T. Hofmann, “End milling of Carbon Fiber Reinforced Plastics as surface pretreatment for adhesive bonding–effect of intralaminar damages and particle residues,” *Journal of Adhesion*, vol. 96, no. 12, pp. 1122–1140, 2020, doi: 10.1080/00218464.2018.1557054.

[24] B. Rauh *et al.*, “UV-laser cleaning and surface characterization of an aerospace carbon fibre reinforced polymer,” *Int J Adhes Adhes*, vol. 82, no. December 2017, pp. 50–59, 2018, doi: 10.1016/j.ijadhadh.2017.12.016.

[25] D. Blass, S. Nyga, B. Jungbluth, H. D. Hoffmann, and K. Dilger, “Composite bonding pre-treatment with laser radiation of 3 μm Wavelength: Comparison with conventional laser sources,” *Materials*, vol. 11, no. 7, 2018, doi: 10.3390/ma11071216.

[26] R. Tao, M. Alfano, and G. Lubineau, “Laser-based surface patterning of composite plates for improved secondary adhesive bonding,” *Compos Part A Appl Sci Manuf*, vol. 109, no. February, pp. 84–94, 2018, doi: 10.1016/j.compositesa.2018.02.041.

[27] R. Tao, M. Alfano, and G. Lubineau, “In situ analysis of interfacial damage in adhesively bonded composite joints subjected to various surface pretreatments,” *Compos Part A Appl Sci Manuf*, vol. 116, no. June 2018, pp. 216–223, 2019, doi: 10.1016/j.compositesa.2018.10.033.

[28] “• Number of cars in U.S. | Statista.” https://www.statista.com/statistics/183505/number-of-vehicles-in-the-united-states-since-1990/ (accessed Jul. 15, 2022).

[29] “Use of energy for transportation - U.S. Energy Information Administration (EIA).” https://www.eia.gov/energyexplained/use-of-energy/transportation.php (accessed Jul. 15, 2022).

[30] “The Advantages And Disadvantages Of Composites - 1956 Words | Bartleby.” https://www.bartleby.com/essay/The-Advantages-And-Disadvantages-Of-Composites-PCPC4EE26N6 (accessed Jul. 15, 2022).

[31] “File:2013 IAA BMW i3 Honeycomb structure.jpg - Wikimedia Commons.” https://commons.wikimedia.org/wiki/File:2013_IAA_BMW_i3_Honeycomb_structure.jpg (accessed Jul. 15, 2022).

[32] “Lightweight Materials for Cars and Trucks | Department of Energy.” https://www.energy.gov/eere/vehicles/lightweight-materials-cars-and-trucks (accessed Jul. 15, 2022).

[33] T. J. Reinhart, *Overview of Composite Materials*. 1998.

[34] A. Kaw, “Mechanics of composite materials,” 2005.

[35] C. T. Herakovich, *Mechanics of fibrous composites*. New York: Wiley, 1998.

[36] and K. C. B. Agarwal, L. Broutman, *Analysis and performance of fiber composites*. 2017.

[37] M. P., *Fiber-reinforced composites: materials, manufacturing, and design*. 2007.

[38] P. Boisse, *Composite Reinforcements for Optimum Performance - 2nd Edition*. 2020.

[39] C. K., *Composite materials: science and engineering*. 2012.

[40] “Carbon Fiber - Unidirectional Fabrics - Selcom Multiaxial Fabrics.” https://www.multiaxialfabrics.com/carbon-fiber-unidirectional-fabrics/?lang=en (accessed Jul. 15, 2022).

[41] E. A. Trejo Sandoval, “Characterizing the deformation response of a unidirectional non-crimp fabric for the development of computational draping simulation models,” p. 167, 2020.

[42] K. Vanclooster, S. V. Lomov, and I. Verpoest, “Experimental validation of forming simulations of fabric reinforced polymers using an unsymmetrical mould configuration,” *Compos Part A Appl Sci Manuf*, vol. 40, no. 4, pp. 530–539, 2009, doi: 10.1016/j.compositesa.2009.02.005.

[43] B.L.Lee, “Failure of Spectra Polyethylene Fiber-Reinforced Composites under Ballistic Impact Loading.” 1993.

[44] A. Margossian, M. Ding, L. Avila Gray, S. Bel, and R. Hinterhölzl, “Flexural characterisation of unidirectional thermoplastic tapes using a dynamic mechanical analysis system,” *16th European Conference on Composite Materials, ECCM 2014*, no. June, pp. 22–26, 2014.

[45] J. M. Aleksandr Cherniaev, Yu Zhang, Duane Cronin, “Quasi-static and dynamic characterization of unidirectional non-crimp carbon fiber fabric composites processed by HP-RTM,” no. 2, pp. 1–13, 2019.

[46] “Thermoset vs Thermoplastic (What is the Difference?) - TWI.” https://www.twi-global.com/technical-knowledge/faqs/thermoset-vs-thermoplastic#ThermosetPlastics (accessed Jul. 15, 2022).

[47] A. A.-S. Mariam Al Ali AlMaadeed, Deepalekshmi Ponnamma, “Polymers to improve the world and lifestyle: physical, mechanical, and chemical needs,” in *Polymer Science and Innovative Applications*, 2020, pp. 1–19.

[48] S. P. A. Crosky, N. Soatthiyanon, D. Duys. Meatherall, *Thermoset matrix natural fibre-reinforced composites*. 2014.

[49] R. C. Dante, D. A. Santamaria, and J. M. Gil, “Crosslinking and thermal stability of thermosets based on novolak and melamine,” *Journal of Applied Polymer Science*, vol. 114, no. 6. pp. 4059–4065, 2009. doi: 10.1002/app.31114.

[50] Y. Li, T. Xie, and G. Yang, “Effects of polyphenylene oxide content on morphology, thermal, and mechanical properties of polyphenylene oxide/polyamide 6 blends,” *J Appl Polym Sci*, vol. 99, no. 5, pp. 2076–2081, 2006, doi: 10.1002/app.22687.

[51] “Desirable features in mold filling simula …,” p. 20029, 2004.

[52] and B. T. M. Graf, E. Fries, J. Renkl, F. Henning, R. Chaudhari, “High pressure resin transfer molding - Process advancements,” 2010.

[53] S. V. Lomov, Ed., *Non-crimp fabric composites: Manufacturing, properties and applications*. Cambridge, 2011.

[54] E. Schmachtenberg, J. Schulte Zur Heide, and J. Töpker, “Application of ultrasonics for the process control of Resin Transfer Moulding (RTM),” *Polym Test*, vol. 24, no. 3, pp. 330–338, 2005, doi: 10.1016/j.polymertesting.2004.11.002.

[55] K. K. Chawla, *Composite Materials: Science and Engineering*, 3 rd. New York: Springer-Verlag, 2012.

[56] L. F. and S. G. Advani, *Resin Transfer Molding*. Boston: Springer, 1998.

[57] M. Achparaki *et al.*, “Advanced Composite Materials by Resin Transfer Molding for Aerospace Applications,” *Intech*, p. 13, 2012.

[58] P. Rosenberg, B. Thoma, P. F. Henning, F. C. Technologie, I. Fahrzeugsystemtechnik, and K. Institut, “Characterization of Epoxy and Polyurethane Resin Systems for Manufacturing of High - Performance Composites in High - Pressure RTM Process,” *15th Annual SPE Automotive Composites Conference and Exhibition*, no. September, pp. 1–18, 2015.

[59] and F. H. R. Chaudhari, P. Rosenberg, M. Karcher, S. Schmidhuber, P. Elsner, “High-pressure RTM process variants for manufacturing of carbon fiber reinforced composites,” ICCM International Conferences on Composite Materials, pp. 1560–1568.

[60] R. W. Kim, C. M. Kim, K. H. Hwang, and S. R. Kim, “Embedded based real-time monitoring in the high-pressure resin transfer molding process for CFRP,” *Applied Sciences (Switzerland)*, vol. 9, no. 9, 2019, doi: 10.3390/app9091795.

[61] P. Gopal and S. Dharmaraj, “Development of a Non-Crimp Fabric Carbon Fiber / Epoxy Composite Technology Demonstrator,” 2020.

[62] K. Agarwal, Bhagwan D.; Broutman, Lawrence J.; Chandrashekhara, *ANALYSIS AND PERFORMANCE OF FIBER COMPOSITES*, THIRD EDIT. 2006.

[63] S. T. Pinho, C. G. Dávila, P. P. Camanho, L. Iannucci, and P. Robinson, “Failure Models and Criteria for FRP Under In-Plane or Three-Dimensional Stress States Including Shear Non-linearity,” *Nasa/Tm-2005-213530*, no. February, p. 68, 2005.

[64] L. Grauers, R. Olsson, and R. Gutkin, “Energy absorption and damage mechanisms in progressive crushing of corrugated NCF laminates: Fractographic analysis,” *Compos Struct*, vol. 110, no. 1, pp. 110–117, 2014, doi: 10.1016/j.compstruct.2013.11.001.

[65] M. D. Banea and L. F. M. Da Silva, “Adhesively bonded joints in composite materials: An overview,” *Proceedings of the Institution of Mechanical Engineers, Part L: Journal of Materials: Design and Applications*, vol. 223, no. 1, pp. 1–18, 2009, doi: 10.1243/14644207JMDA219.

[66] “What Is a Bolted Joint? | Blog Posts | OneMonroe.” https://monroeengineering.com/blog/what-is-a-bolted-joint/ (accessed Jul. 13, 2022).

[67] “Advantages and Disadvantages of Riveting | Mecholic.” https://www.mecholic.com/2018/10/advantages-and-disadvantages-of-riveting.html (accessed Jul. 13, 2022).

[68] “Adhesive bonding (introduction) [SubsTech].” https://www.substech.com/dokuwiki/doku.php?id=adhesive_bonding_introduction#advantages_of_adhesive_bonding (accessed Jul. 13, 2022).

[69] A. Baldan, “Adhesively-bonded joints and repairs in metallic alloys, polymers and composite materials: Adhesives, adhesion theories and surface pretreatment,” *J Mater Sci*, vol. 39, no. 1, pp. 1–49, 2004, doi: 10.1023/B:JMSC.0000007726.58758.e4.

[70] G. D. Davis, *Surface treatments of selected materials*, vol. 1–2. 2018. doi: 10.1007/978-3-319-55411-2_8.

[71] C. Buchmann, S. Langer, J. Filsinger, and K. Drechsler, “Analysis of the removal of peel ply from CFRP surfaces,” *Compos B Eng*, vol. 89, pp. 352–361, 2016, doi: 10.1016/j.compositesb.2015.11.019.

[72] M. Kanerva and O. Saarela, “The peel ply surface treatment for adhesive bonding of composites: A review,” *Int J Adhes Adhes*, vol. 43, pp. 60–69, 2013, doi: 10.1016/j.ijadhadh.2013.01.014.

[73] Fernholz KD., “Bonding of polymer matrix composites,” in *Advances in Stracutral Adhesive Bonding*, 2010, pp. 265–291.

[74] R. J. Zaldivar, H. I. Kim, G. L. Steckel, J. P. Nokes, and D. N. Patel, “The effect of abrasion surface treatment on the bonding behavior of various carbon fiber-reinforced composites,” *J Adhes Sci Technol*, vol. 26, no. 10–11, pp. 1573–1590, 2012, doi: 10.1163/156856111X618425.

[75] G. Yang, T. Yang, W. Yuan, and Y. Du, “The influence of surface treatment on the tensile properties of carbon fiber-reinforced epoxy composites-bonded joints,” *Compos B Eng*, vol. 160, no. July 2018, pp. 446–456, 2019, doi: 10.1016/j.compositesb.2018.12.095.

[76] S. M. Park, R. Roy, J. H. Kweon, and Y. Nam, “Strength and failure modes of surface treated CFRP secondary bonded single-lap joints in static and fatigue tensile loading regimes,” *Compos Part A Appl Sci Manuf*, vol. 134, no. January, p. 105897, 2020, doi: 10.1016/j.compositesa.2020.105897.

[77] Sina. Ebnesajjad, *Handbook of adhesives and surface preparation technology, applications and manufacturing*. 2011.

[78] Y. Nandwani, “Characterization of Structural Adhesives Using Lap Shear and Pin and Collar Tests,” 2015.

[79] R. AJ. Satas, D, Tracton, AA, *Coatings Technology Handbook*, Second Edi. J Electron Packag, 2002.

[80] A. Ganesan, M. Yamada, and M. Fukumoto, “The effect of CFRP surface treatment on the splat morphology and coating adhesion strength,” *Journal of Thermal Spray Technology*, vol. 23, no. 1–2, pp. 236–244, 2014, doi: 10.1007/s11666-013-0003-z.

[81] V. H. Martínez-Landeros, S. Y. Vargas-Islas, C. E. Cruz-González, S. Barrera, K. Mourtazov, and R. Ramírez-Bon, “Studies on the influence of surface treatment type, in the effectiveness of structural adhesive bonding, for carbon fiber reinforced composites,” *J Manuf Process*, vol. 39, no. January, pp. 160–166, 2019, doi: 10.1016/j.jmapro.2019.02.014.

[82] F. Fischer, S. Kreling, F. Gäbler, and R. Delmdahl, “Using excimer lasers to clean CFRP prior to adhesive bonding,” *Reinforced Plastics*, vol. 57, no. 5, pp. 43–46, 2013, doi: 10.1016/S0034-3617(13)70156-5.

[83] F. Fischer, S. Kreling, P. Jäschke, M. Frauenhofer, D. Kracht, and K. Dilger, “Laser surface pre-treatment of CFRP for adhesive bonding in consideration of the absorption behaviour,” *Journal of Adhesion*, vol. 88, no. 4–6, pp. 350–363, 2012, doi: 10.1080/00218464.2012.660042.

[84] L. Sorrentino, S. Marfia, G. Parodo, and E. Sacco, “Laser treatment surface: An innovative method to increase the adhesive bonding of ENF joints in CFRP,” *Compos Struct*, vol. 233, no. November 2019, 2020, doi: 10.1016/j.compstruct.2019.111638.

[85] B. Rauh *et al.*, “UV-laser cleaning and surface characterization of an aerospace carbon fibre reinforced polymer,” *Int J Adhes Adhes*, vol. 82, no. December 2017, pp. 50–59, 2018, doi: 10.1016/j.ijadhadh.2017.12.016.

[86] P. H. da S. Santos, “Mechanical Characterization and Computational Modeling of Gels,” *Purdue University*, vol. 9, p. 176, 2011.

[87] U. States and E. Commission, “Hexion inc.,” no. x, 2016.

[88] P. Description, “EPIKOTE ™ Resin TRAC 06170 EPIKURE ™ Curing Agent TRAC 06170 HELOXY ™ Additive TRAC 06805,” vol. 06170, 2015.

[89] R. C. Dehaghani, “Experimental and Numerical Assessment of Adhesively Bonded Non-Crimp Fabric Carbon Fiber / Epoxy Composite Joints,” 2021.

[90] Toray Group, “Zoltek PX35 Commercial Carbon Fiber,” *ZOLTEK Toray Group*, 2022.

[91] B. Watson, Y. Nandwani, M. J. Worswick, and D. S. Cronin, “Metallic multi-material adhesive joint testing and modeling for vehicle lightweighting,” *Int J Adhes Adhes*, vol. 95, no. May, p. 102421, 2019, doi: 10.1016/j.ijadhadh.2019.102421.

[92] “3M™ Scotch-Weld™ Epoxy Adhesive DP190 | 3M Canada.” https://www.3mcanada.ca/3M/en_CA/p/d/b40066476/ (accessed Jul. 24, 2022).

[93] T. Data, “Impact Resistant Structural Adhesive 07333 / 57333,” no. July, pp. 1–6, 2015.

[94] B. Zhang, Z. Chang, J. Li, X. Li, Y. Kan, and Z. Gao, “Effect of kaolin content on the performances of kaolin-hybridized soybean meal-based adhesives for wood composites,” *Compos B Eng*, vol. 173, no. May, pp. 1–8, 2019, doi: 10.1016/j.compositesb.2019.106919.

[95] “ME720 - Special topics in Solids Mechanics Winter 2022 LEC _ 11 : Surface pre-treatments,” 2022.

[96] “ME720 - Special topics in Solids Mechanic Interfacial contact , wettability and adhesion,” 2021.

[97] M. Suzuki *et al.*, “Article in press,” *Int J Radiat Oncol Biol Phys*, vol. 26, pp. 1–8, 2006, doi: 10.1016/j.ijadhadh.2005.08.001.

[98] “ME720 - Special topics in Solids Mechanics Winter 2021 Interfacial contact , wettability and adhesion,” 2021.

[99] “Intro to fracture equations.” https://sethna.lassp.cornell.edu/SimScience/cracks/advanced/math1.html (accessed Jul. 05, 2022).

[100] M. F. S. F. de Moura, J. J. L. Morais, and N. Dourado, “A new data reduction scheme for mode I wood fracture characterization using the double cantilever beam test,” *Eng Fract Mech*, vol. 75, no. 13, pp. 3852–3865, Sep. 2008, doi: 10.1016/j.engfracmech.2008.02.006.

[101] L. Y. Xu, J. R. Lu, K. M. Li, and J. Hu, “Removal mechanism of CFRP by laser multi direction interaction,” *Opt Laser Technol*, vol. 143, no. June, 2021, doi: 10.1016/j.optlastec.2021.107281.

[102] M. Alfano, G. Lubineau, F. Furgiuele, and G. H. Paulino, “Study on the role of laser surface irradiation on damage and decohesion of Al/epoxy joints,” *Int J Adhes Adhes*, vol. 39, pp. 33–41, 2012, doi: 10.1016/j.ijadhadh.2012.03.002.

[103] S. Oshima, A. Yoshimura, Y. Hirano, T. Ogasawara, and K. T. Tan, “In-situ observation of microscopic damage in adhesively bonded CFRP joints under mode I and mode II loading,” *Compos Struct*, vol. 227, no. August, p. 111330, 2019, doi: 10.1016/j.compstruct.2019.111330.

[104] H. Chai, “Shear fracture,” *Int J Fract*, vol. 37, no. 2, pp. 137–159, 1988, doi: 10.1007/BF00041716.

[105] W. Li, G. Zhang, Y. Huang, and Y. Rong, “UV laser high-quality drilling of CFRP plate with a new interlaced scanning mode,” *Compos Struct*, vol. 273, no. February, p. 114258, 2021, doi: 10.1016/j.compstruct.2021.114258.

[106] “Carbon-Black Reinforcement of Adhesives and Sealants | Adhesives & Sealants Industry.” https://www.adhesivesmag.com/articles/84175-carbon-black-reinforcement-of-adhesives-and-sealants (accessed Aug. 05, 2022).

[107] WORLD INTELLECTUAL ORGANIZATION, “INTERNATIONAL APPLICATION PUBLISHED UNDER THE PATENT COOPERATIN TREATY (PCT).pdf.” 2017.